Neutral Particle Detection by a Structured Cathode of a Micro-Pattern Gaseous Detector

Master Thesis
Faculty of Physics
Ludwig-Maximilians-Universität Munich

submitted by
Katrin Penski
born in Munich

Supervisor: Prof. Dr. Otmar Biebel
Munich, November 13, 2020

Detektion neutraler Teilchen mittels einer strukturierten Kathode in einem mikrostrukturierten Gasdetektor

Masterarbeit der Fakultät für Physik
der
Ludwig-Maximilians-Universität München

vorgelegt von
Katrin Penski
geboren in München

Gutachter: Prof. Dr. Otmar Biebel
München, den 13. November 2020

Abstract

In this thesis two different detection techniques for photons and neutrons are investigated with the aim to increase the detection efficiency using Micro-Pattern Gaseous Detectors (MPGDs). MPGDs are high-rate capable detectors with a good spatial and temporal resolution. Nevertheless, due to the low density of gas these detectors exhibit a poor detection efficiency for electrically neutral particles. The detection efficiency can be increased for photons by using a proper solid converter cathode which is made of high-Z materials or for neutrons with materials which have a large neutron interaction cross section.

This thesis discusses a further improvement of the photon conversion efficiency using several tilted converter layers which are stacked with large overlap inside a MPGD. Consequently, the incoming photons have a higher interaction probability. According to Geant4 simulations the conversion probability can be increased by a factor of 2.5 compared to a single converter cathode for 50 keV photons. After the interaction process the created electrons are located between the tilted layers. For detection they are guided to the amplification and readout area of the used detector by a specific designed electric field configuration. The tilted layers in combination with the electric guidance field act as structured cathode. Influences of the electric field on the electron movement are examined regarding the photon reconstruction efficiency and the electron distribution in the structured cathode area. The structured cathode is placed inside a GEM detector. In order to study the electron guiding efficiency, the structured cathode is irradiated by 5.9 keV photons of an ^{55}Fe-source. A very good agreement between the measurement results and a simulation based on ANSYS and Garfield++ is achieved. The investigation of the photon detection efficiency uses the same setup irradiated with an ^{241}Am-source emitting 59.5 keV photons. In order to simulate the photon-matter interaction Geant4 is added to the simulation. Measurement and simulation of the electron efficiency peak and electron distribution agree very well. Furthermore, with this structured cathode a two times higher detection efficiency compared to pure gas is measured showing that the structured cathode works as intended.

Also the detection of neutrons with a ^{10}B cathode is investigated. Therefore, measurements at the Tandem van de Graaff Accelerator in Garching have been performed. Different objects are placed between beam and detector to reconstruct the shape of the object in the detector and compare the measurements to corresponding Geant4 simulations. In most cases simulation and measurement show the same behavior although many side effects influence the measurement. This imaging process works for photons as well as for neutrons making most of the objects placed in the beam reconstructable.

Kurzfassung

In dieser Arbeit werden zwei verschiedene Detektionsmechanismen für Photonen und Neutronen mit dem Ziel untersucht, die Detektionseffizienz von mikrostrukturierten Gasdetektoren (MPGDs) zu erhöhen. Diese Detektoren sind hochratenfähig und weisen eine gute räumliche und zeitliche Auflösung auf. Jedoch haben sie aufgrund der geringen Gasdichte eine niedrige Detektionseffizienz für elektrisch neutrale Teilchen. Diese kann für Photonen durch eine Konversionsschicht aus Materialien mit hoher Ordnungszahl erhöht werden, während für Neutronen Materialien mit einem großem Neutronenwechselwirkungsquerschnitt nötig sind.

Um die Detektionseffizienz von Photonen zu verbessern, werden mehrere Konversionsschichten unter einem bestimmten Winkel mit großem Überlapp in einem MPGD positioniert. Dadurch haben die einfallenden Photonen eine höhere Wechselwirkungswahrscheinlichkeit. Gemäß einer Geant4 Simulation kann diese für 50 keV Photonen im Vergleich zu einer einzelnen Kathode um den Faktor 2.5 gesteigert werden. Zur Detektion werden die beim Wechselwirkungsprozess erzeugten Elektronen durch die spezielle Konfiguration eines elektrischen Feldes zum Verstärkungs- und Auslesebereich geleitet. Im GEM Detektor bilden die gekippten Konversionsschichten in Kombination mit dem elektrischen Feld die strukturierte Kathode. Mit dieser werden die Einflüsse des elektrischen Feldes auf die Elektronenbewegung untersucht, wobei die Effizienz der rekonstruierten Photonen und die Elektronenverteilung im Kathodenbereich im Vordergrund stehen. Um die Effizienz der Elektronenführung zu analysieren, wird eine 5.9 keV Photonen emittierende ^{55}Fe-Quelle verwendet. Die auf ANSYS und Garfield++ basierenden Simulationsergebnisse stimmen mit den Messungen überein. Für die Untersuchung der Photonenkonversionseffizienz wird eine ^{241}Am-Quelle verwendet, die 59.5 keV Photonen emittiert. Um auch in der Simulation die Photon-Materie-Wechselwirkung zu betrachten, wird diese um Geant4 ergänzt. Die Ergebnisse von Simulation und Messung bezüglich des Elektroneneffizienzpeaks und der Elektronenverteilung stimmen überein. Durch das Hinzufügen einer strukturierten Kathode wird die Detektionseffizienz verdoppelt und die gewünschte Funktion erfüllt.

Zum Neutronennachweis wird eine ^{10}B-Kathode verwendet. Die Messungen erfolgen am Tandem van de Graaff-Beschleuniger in Garching. Dabei werden zwischen dem Teilchenstrahl und dem Detektor verschiedene Objekte platziert, um die Form des Objekts zu rekonstruieren. Anschließend werden die Ergebnisse mit Geant4 Simulationen verglichen. In den meisten Fällen zeigen Simulation und Messung das gleiche Verhalten, jedoch werden die Messergebnisse durch verschiedene äußere Einflüsse bestimmt, die in der Simulation nicht berücksichtigt werden. Der Bildgebungsprozess funktioniert sowohl für Photonen als auch für Neutronen, wodurch die meisten im Strahl platzierten Objekte rekonstruiert werden können.

Contents

1 Introduction **1**

2 Theoretical Background **3**
2.1 Particle Interaction with Matter . . . 3
2.1.1 Charged particles . . . 3
2.1.2 Photons . . . 3
2.1.3 Neutrons . . . 5
2.2 Operation Regions of Gaseous Detectors . . . 6
2.3 Gas Multiplication . . . 7

3 The GEM Detector **9**
3.1 Working Principle and Detector Setup . . . 9
3.2 Readout Electronics . . . 11
3.3 Readout Software and Signal Analysis . . . 11

4 Simulation Software **13**
4.1 Geant4 . . . 13
4.2 ANSYS . . . 13
4.3 Garfield++ . . . 13

5 Improvement of the Photon Detection Efficiency **15**
5.1 Theoretical Principle . . . 15
5.2 Simulation . . . 19
5.2.1 Structured Cathode Geometries Created with ANSYS . . . 19
5.2.2 Electron Guiding Simulated with Garfield++ . . . 23
5.2.3 Results of Electron Guiding for Different Geometries . . . 25
5.2.4 Results of Electron Guiding for Final Geometry . . . 37
5.2.5 Photon Conversion Simulated with Geant4 . . . 39
5.2.6 Results of Combined Photon Conversion and Electron Guiding . 41
5.3 Measurements . . . 44
5.3.1 Setup . . . 44
5.3.2 Results for Electron Guiding using an Fe-55 Source . . . 48
5.3.3 Results for Conversion Efficiency using an Am-241 Source . . . 57
5.4 Conclusion . . . 63

6 Neutron Detection **65**
6.1 Theoretical Principle . . . 65
6.2 Measurement at the Tandem van de Graaf Accelerator in Garching . . 66
6.2.1 Setup . . . 66

6.2.2 Detection Mechanism 68
6.2.3 Imaging Processes 69
6.3 Conclusion 78

7 Summary and Outlook **79**

A Printed Resistors **81**

B Calculation of the Electron Guiding Angle **83**

C Simulation of the GEM Foil **87**

D Construction of the Detector Housing **89**

E Construction of the Lamellae Mount **91**

Bibliography **95**

Chapter 1

Introduction

Over the last century different detector concepts were developed and further improved. Exemplary detector types are gaseous, semiconductor or scintillation based. Each of them is specialized to certain applications. Since Micro-Pattern Gaseous Detectors (MPGDs) provide a high rate capability, a good spatial resolution ($<100\,\mu m$) and are background tolerant, they have a wide range of applications like in high-energy physics or medical imaging techniques. Nevertheless, due to the low density of the detector gas, they exhibit only a poor intrinsic detection efficiency for electrically neutral particles like photons and neutrons. Both particles provide complementary information in imaging techniques which emphasizes the need of a high detection efficiency for photons as well as for neutrons. In this thesis two currently independent detection mechanisms for photons and neutrons are investigated aiming for a higher detection efficiency. For the measurements a GEM detector [1] is used.

Typically, for photon detection one solid converter cathode with high-Z coating is used. In order to obtain higher efficiencies, the basic idea is to use several tilted converter layers which are stacked with large overlap inside the detector. With an optimized setup regarding the cathode geometry and detector performance, the efficiency for photons with energies about 50 keV should be improved. Since photons are used for several medical imaging techniques, a higher quantum efficiency reduces the radiation exposure for the patients.

Due to their interaction process with the atomic nuclei, neutrons are a favorable source for non-destructive probing. Additionally, neutrons penetrate materials better than photons and achieve a very good isotopic-specific contrast [2]. These properties have their application in radiographic or tomographic imaging techniques. Also, in these areas an increased neutron conversion efficiency is favorable. Therefore, in this thesis first investigations regarding the neutron detection mechanism using a ^{10}B cathode are performed.

For photons as well as for neutrons there are many applications which benefit from higher detection efficiencies. This motivates the investigation of different detection techniques improving their efficiency.

Chapter 2

Theoretical Background

2.1 Particle Interaction with Matter

Particles can be detected through their interaction processes with matter using a proper particle detector concept. In this thesis the focus lies on the detection of neutral particles like photons and neutrons using a gaseous ionization detector.

2.1.1 Charged particles

Charged particles can directly ionize the gas in the detector. Considering small corrections for electrons the average energy loss of a charged particle per unit length is defined by the Bethe-Bloch equation [3]

$$-\left\langle \frac{\mathrm{d}E}{\mathrm{d}x} \right\rangle = 4\pi N_\mathrm{A} r_\mathrm{e}^2 m_\mathrm{e} c^2 \rho \frac{Z z^2}{A\beta^2} \left(\frac{1}{2} \ln \left[\frac{2 m_\mathrm{e} c^2 \beta^2 \gamma^2 T_\mathrm{max}}{I^2} \right] - \beta^2 - \frac{\delta}{2} \right) \tag{2.1}$$

with the Avogadro constant N_A, the classical radius r_e and mass m_e of the electron, the speed of light c, the Lorentz factor $\gamma = 1/\sqrt{1-\beta^2}$, the properties of the absorbing material including its density ρ, atomic number Z and atomic weight A. The incoming particle has a velocity v ($\beta = v/c$) and a charge z in units of e. T_max is the maximum energy transfer, I the mean ionization potential of the material and δ the Fermi density correction [4]. Due to this energy deposition by the charged particle electron-ion pairs are created.

2.1.2 Photons

Photons interact differently with matter since they are not electrically charged. They can either be absorbed or scattered by the electron shell of the gas atom creating primary electrons. Highly energetic photons can convert to an electron-positron pair if for example the nucleus of an atom is engaged to conserve energy and momentum. The different interaction processes are now described in more detail. The occurring processes are the photoelectric effect, Compton and pair creation as shown in figure 2.1 for argon.

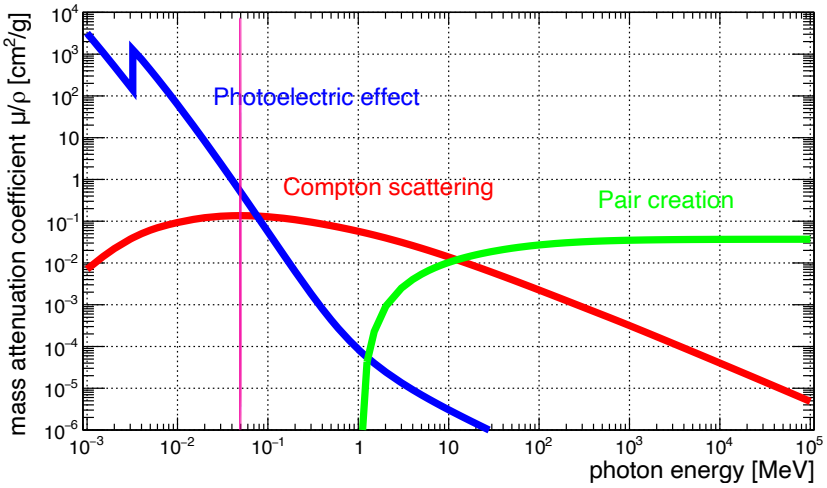

Figure 2.1: The photon mass attenuation coefficient μ/ρ for argon plotted against the photon energy. Depending on the photon energy three different interaction processes can occur: Photoelectric effect, Compton scattering or pair creation (data taken from [5]). The pink line indicates the interaction process for 50 keV photons.

The dominant process is determined by the incident photon energy and is also influenced by the used material (here argon). Since these effects are purely statistical, photons do not show a definite range in matter. But according to the Lambert-Beer law [6] a photon beam I_0 is attenuated exponentially if it penetrates into a material with thickness x

$$I(x) = I_0 \cdot e^{-\mu x} \tag{2.2}$$

with the linear attenuation coefficient μ which contains information about material properties. The mass attenuation coefficient μ/ρ is then defined as

$$\frac{\mu}{\rho} = \sigma \cdot \frac{N_\mathrm{A}}{m_\mathrm{a}} \tag{2.3}$$

where σ is the photon absorption cross section of the material, ρ is the density of the material, N_A is the Avogadro constant and m_a is the atomic molar mass [6].

For photons with energies below 100 keV the photoelectric effect is the dominant interaction process. A photon is absorbed and transfers its complete energy to an electron of the material. If the photon energy E_γ is larger than the binding energy E_B of the electron, ionization takes place. The electron leaves the atom with a kinetic energy of $E_\mathrm{kin} = E_\gamma - E_\mathrm{B}$. The cross section σ_ph defines the probability for photoionization according to ([6], [7])

$$\sigma_\mathrm{ph} = \sqrt{32} \cdot \alpha^4 \cdot Z^5 \cdot \epsilon^{-3.5} \cdot \sigma_\mathrm{Th} \tag{2.4}$$

and depends on the fine-structure constant α, the atomic number Z, the reduced photon energy $\epsilon = E_\gamma/(m_\mathrm{e}c^2)$ and the Thomson cross section $\sigma_\mathrm{Th} = \frac{8}{3}\pi r_\mathrm{e}^2$ with the electron radius r_e. For increasing photon energies, the Compton scattering becomes more dominant. In this process the kinetic energy and momentum of the photon is only partially delivered to an electron while the photon is scattered. If the photon energy exceeds 1.022 MeV $\approx 2m_\mathrm{e}$, which corresponds to twice of the rest mass of an electron, pair creation occurs. Here the photon creates an electron-positron pair in the Coulomb field of the nucleus [6]. Despite from pair creation, in both other processes a primary

electron and a corresponding positive charged ion is created. For energies larger than the binding energy of the medium either this electron or the scattered photon can cause further ionization.

2.1.3 Neutrons

Like photons, neutrons are electrically neutral. Nevertheless, they differ in their interaction processes with matter. Neutrons interact through the strong force with the atomic nuclei. Due to confinement the strong force is limited to approximately 10^{-15} m around the nucleus making neutrons very penetrating particles [8]. Nevertheless, if a neutron approaches the nucleus within this radius, different interaction processes can occur depending on the energy of the neutron. Neutrons with energies of some MeV are elastically scattered at the nuclei losing energy and momentum. If the neutron energy is sufficiently large, excitation of the nucleus can happen. The deexcitation follows in a radiative transition where a photon is emitted. Besides scattering, the neutron can also be captured by the nucleus while charged particles are emitted e.g. (n,α), (n,p) or (n,d). This process dominates for neutron energies in the range of some eV to keV since the cross section is indirectly proportional to the neutron velocity v_n [8]. Neutrons within this energy region are called thermal neutrons and can be observed in radiative neutron capture or fission processes. The total interaction probability for neutrons with matter is defined by the sum of the different cross sections [8]

$$\sigma_\mathrm{total} = \sigma_\mathrm{elastic} + \sigma_\mathrm{capture} + \ldots \tag{2.5}$$

which leads to the mass attenuation coefficient

$$\frac{\mu}{\rho} = \sigma_\mathrm{total} \cdot \frac{N_\mathrm{A}}{m_\mathrm{a}} \tag{2.6}$$

with the same variables used in equation 2.3. As photons, also neutrons experience an exponentially attenuation according to equation 2.2.

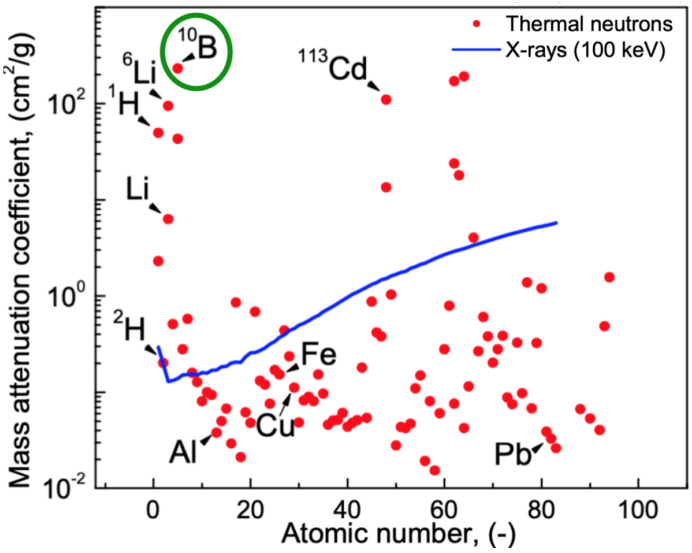

Figure 2.2: Mass attenuation coefficient for 100 keV photons (blue line) and thermal neutrons (red dots) in dependence of the atomic number of the material (taken from [9]). Since boron (green circle) shows a large mass attenuation coefficient it is used for thermal neutron detection in this thesis.

For 100 keV photons and thermal neutrons the mass attenuation is presented in figure 2.2. While for photons the mass attenuation coefficient increases with the atomic number, for thermal neutrons no correlation between both values can be observed. Nevertheless, boron exhibits a large mass attenuation coefficient (green circle). Consequently, it is used for detection of thermal as well as higher energetic neutrons in this thesis. The detection mechanism is described in chapter 6.

2.2 Operation Regions of Gaseous Detectors

Ionizing radiation can be detected using gaseous detectors. The radiation ionizes the detector gas creating electron-ion pairs which are separated by an electric field. In order to measure the small amount of created charges, amplification processes have to be used. Depending on the applied electric field gaseous detectors have different operation regions as shown in figure 2.3.

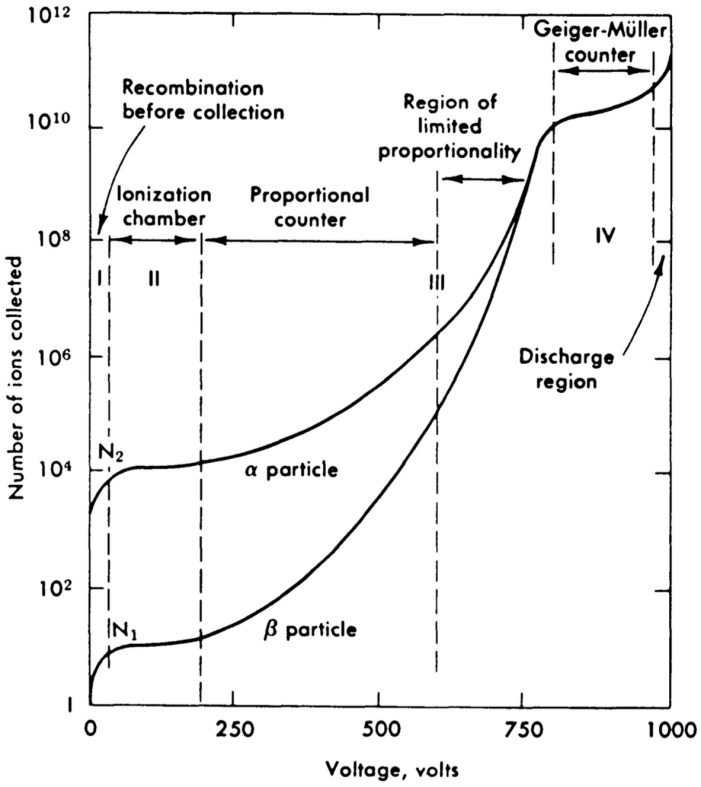

Figure 2.3: Gaseous detectors show different operation regions depending on the electric field. Here the number of collected ions as a function of the applied voltage for electrons and α-particles is shown (taken from [10]).

If no voltage is applied, the recombination of the electron-ion pairs by their own electrical attraction dominates. Consequently, no signal can be observed which makes particle detection impossible. With increasing voltage, the electron-ion pairs feel an increasing electrostatic force. If this force exceeds the attractive recombination forces, the electron-ion pairs can be separated, and a current is measurable. While the positive ions drift to the cathode, the electrons are accelerated to the anode. At a certain voltage the current stays constant (region II in figure 2.3) because all created electron-ion pairs are collected. In this region ionization chambers are operated. A further raise in voltage leads again to an increasing current. Through the strong electric field, the kinetic

energy of the primary electron becomes high enough to ionize further gas molecules. In this process secondary electrons are created which are then also accelerated and additional ionization takes place. In this way an electron avalanche is generated. The measured signal is amplified but the number of electron-ion pairs is directly proportional to the primary ionization charge. As shown in figure 2.3 the number of collected ions for α and β particles differs in this region. Up to point III proportional gas multiplication (more details in section 2.3) is observed. Detectors working in this operation region are known as proportional counters. At higher voltages the region of limited proportionality is reached where the number of electron-ion pairs further increases. As a result, a space charge is created because the ions flow off slower since their drift velocity is smaller than for electrons. Proportionality is no longer given. If an ion recombines with an electron a photon is emitted which causes more ionization in the gas but mainly from metallic surfaces. This results in further electron avalanches and a measured current which is independent of the energy of the initial radiation. Detected particles become indistinguishable in this so-called Geiger-Müller region. The voltages in the discharge region are so high, that a continuous breakdown happens with and without radiation. Consequently, no detection can be made at these voltages [8].

2.3 Gas Multiplication

In the proportional region of a gaseous detector gas amplification takes place. The primary electrons are accelerated by a strong electric field and gain kinetic energy. If the kinetic energy is higher than the ionization potential, gas ionization can happen which results in the creation of further electrons [6]. This mechanism, where N electrons create $\mathrm{d}N$ new electrons along a path $\mathrm{d}x$

$$\mathrm{d}N = N\alpha \mathrm{d}x \tag{2.7}$$

is called Townsend avalanche process with the first Townsend coefficient α [11]. This coefficient describes the probability of ionization per path length. It is connected to the free path λ of an electron between two collisions via $\alpha = 1/\lambda$. According to equation 2.7 there are in total

$$N = N_0 \cdot e^{\alpha x} \tag{2.8}$$

electrons after N_0 primary electrons traverse the distance x. The multiplication factor M is than defined by

$$M = \frac{N}{N_0} = e^{\alpha x} \tag{2.9}$$

or in case of a dependence of α on the electric field and the gas

$$M = e^{\int_{r_1}^{r_2} \alpha(x) dx} \tag{2.10}$$

for a path between r_1 and r_2. In general, the Townsend coefficient for different gas or gas mixtures can be calculated using modern computer programs which include ionization and excitation processes and the influence of the electric field on the electron drift. Nevertheless, an approximation for low values of the Townsend coefficient was developed by Rose and Korff [12]

$$\alpha = A \cdot p \cdot e^{-\frac{B \cdot p}{E}} \tag{2.11}$$

where A and B are gas constants, E the electric field and p the gas pressure.

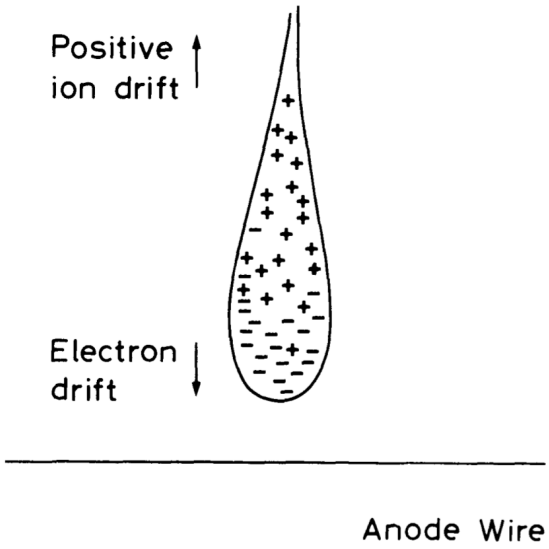

Figure 2.4: Drop-like distribution of an electron-ion avalanche next to a thin anode wire. Since electrons show a higher mobility they are located in the bottom of the drop while the positive charged ions which have a lower mobility are responsible for the drop-like shape (taken from [8]).

Due to their higher mobility the electrons separate quickly from the slower drifting ions. This is the reason why the resulting avalanche has the shape of a liquid-drop as it is shown in figure 2.4. Although equation 2.10 predicts an exponentially growing multiplication factor, in reality it is limited by the Raether limit of $M < 10^8$ or $\alpha x < 20$ [13]. As described in section 2.2 for voltages beyond point III the effective voltage decreases due to space charge from the positive ions while the voltage difference further increases. This effect leads to a saturation of the created electron-ion pairs and a limitation of the gas amplification [8].

Chapter 3

The GEM Detector

The Gaseous Electron Multiplier (short GEM) detector belongs to the Micro-Pattern Gaseous Detectors (MPGDs) and was developed by Fabio Sauli in 1997 [1]. It works as proportional counter (see section 2.2), therefore the detected signal is proportional to the energy deposition of the traversing particle.

3.1 Working Principle and Detector Setup

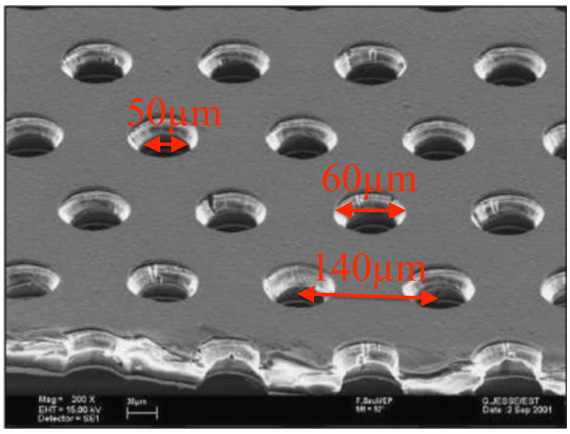

Figure 3.1: Electron microscopic image of a GEM foil showing the hole structure (taken from [1], edited).

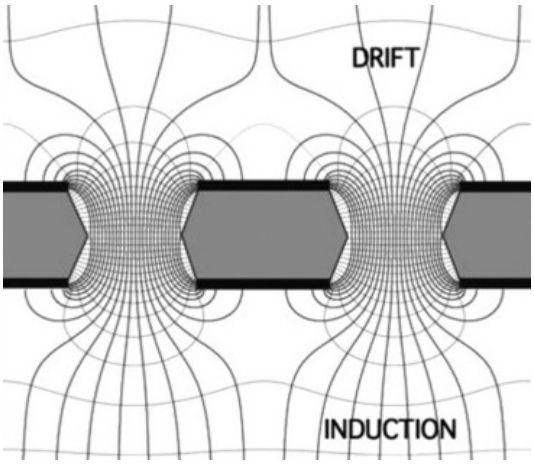

Figure 3.2: Electric field inside two holes of a GEM foil (taken from [1]).

The central component of this detector is the GEM foil which is made of a 50 µm thick Kapton foil covered by 5 µm thick copper layers at top and bottom. With photolithography and chemical etching cone-shaped holes with 60 µm inner and 70 µm outer diameter are created as shown in figure 3.1. They are arranged in a periodic structure with a distance of 140 µm. Applying a voltage difference of about 300 V between both copper layers leads to an electric field of 60 kV cm^{-1} inside the GEM holes. The field configuration can be seen in figure 3.2. This high field causes an electron multiplication (see section 2.3). Electron avalanches are created for electrons above the GEM foil with an amplification factor of about 20 per foil. A further multiplication is achieved by stacking multiple foils.

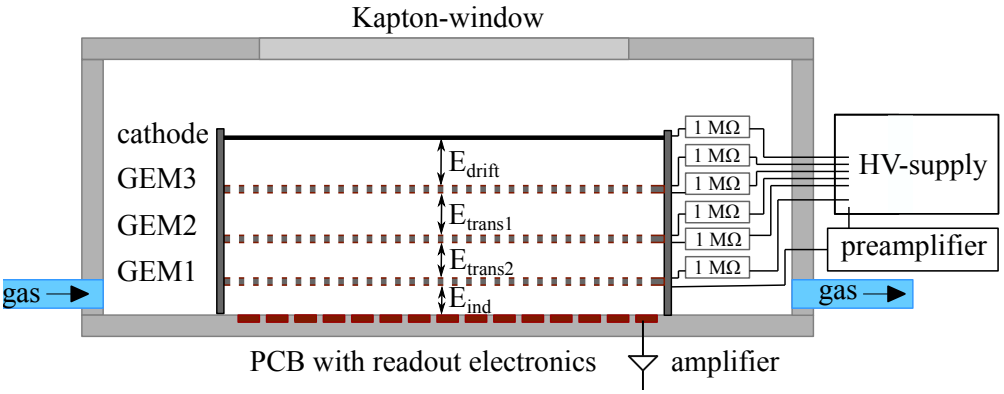

Figure 3.3: Illustration of the GEM detector setup including three GEM foils (not to scale).

Figure 3.3 shows the principle setup of the used GEM detector. In total three standard GEM foils are placed inside an Aluminum housing. In order to prevent sparks between the foils, they have a distance of 2 mm. The use of three GEM foils increases the amplification factor to about 20^3. In general, the GEM detector can be divided into three different areas: the drift, amplification and readout region. First, an incoming particle enters the detector through a window made of Kapton and Aluminum. An interaction can occur either in the cathode or the detector gas according to section 2.1. If an electron-ion pair is created and is located between the cathode and the top side of the GEM3 foil, the electron has to be guided to the amplification and readout area for detection. Therefore, all three GEM foils and the cathode are connected to a high-voltage power supply with increasing negative high voltage from bottom to top while the readout area is grounded. Due to the voltage difference between cathode and top side of the GEM3 foil an electric field E_{drift} is created. Consequently, the ions move to the cathode while the electrons drift to the amplification region were three GEM foils are located. Each GEM foil increases the number of electrons and the transport between the GEM foils is achieved by the electric fields E_{trans1} and E_{trans2}. To induce a signal on the readout anode an electric field E_{ind} between the bottom side of the GEM1 foil and the anode is necessary. This anode consists of a Printed Circuit Board (PCB) with two perpendicular oriented strip layers which form a two-dimensional readout structure. Each layer consists of 250 copper strips with a pitch of 400 µm. In order to guarantee a homogeneous charge distribution, the copper strips of the lower layer have to be wider (320 µm) than the ones on the upper layer (80 µm). This readout mechanism provides a good spatial resolution of less than 100 µm.

The detector has an active area of 10 cm × 10 cm. For this thesis the detector is flushed with a gas mixture of 93:7 vol. % Ar:CO_2 under a constant flux. While Argon is taken for gas amplification, CO_2 works as quencher. It absorbs UV photons which are created during the gas amplification process and prevents further ionization in the detector by these photons. Additionally, a slight overpressure of 1 mbar to 5 mbar ensures that no oxygen (O_2) or humidity (H_2O gas) can enter the detector through leaks. Already a small amount of O_2 influences the amplification process and as a consequence also the measurement results. The 1 MΩ resistors (see figure 3.3) reduce the noise of the power supply unit while the bottom side of the GEM1 foil is connected to a preamplifier which provides a trigger signal. This process is further discussed in the next section.

3.2 Readout Electronics

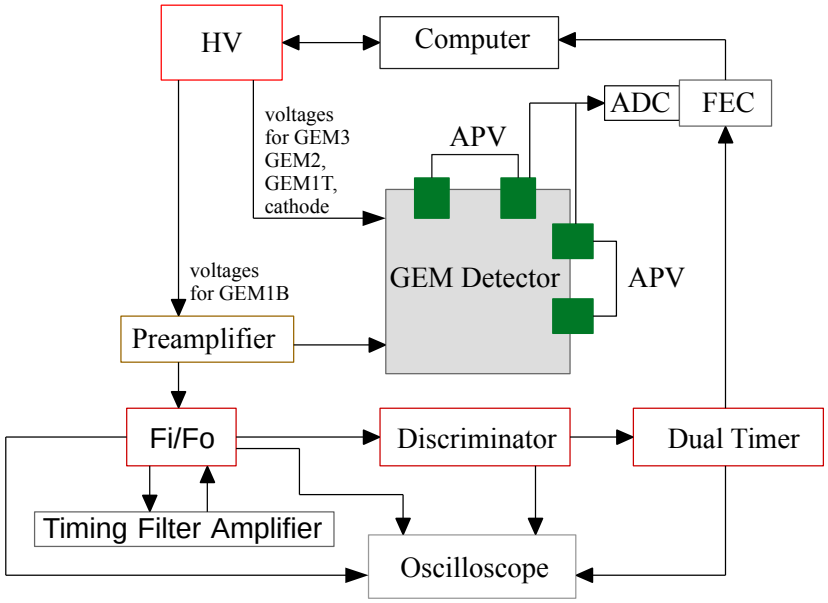

Figure 3.4: Scheme of high voltage (HV) power supply and the used readout electronics. For the GEM1 foil the ending 'B' stands for the bottom side and 'T' for the top side.

Figure 3.4 shows the connection scheme for the high voltage power supply unit and the readout electronics which is used for signal recording. If the electrons drift towards the copper strips on the readout area, a signal is induced. For readout the strips are connected to APV25 frontend boards [14] which have 128 channels each. In x- and y-direction two sperate pairs of APV25-chips are used. The APVs send the analog signal to an analog-digital-converter (ADC) which is connected to a Front-End Concentrator (FEC) card [15] for readout. The FEC-card needs an external trigger. Due to the electron drift to the anode, a signal is also induced on the bottom side of the GEM1 foil. This signal is increased by a preamplifier and then branched by a linear fan-in/fan-out (Fi/Fo) device. The main use of this signal branching is the visualization on the oscilloscope. With the Timing-Filter Amplifier the signal is shaped including smoothing and adapting to a Gaussian shape. For the discriminator a threshold value is set. If the signal exceeds this value, a rectangular-shaped trigger-pulse (NIM standard) is send to the Dual Timer which increases the pulse length and sends the signal to the FEC to start the readout. The signals from the FEC-card are send to a computer via a Gigabit ethernet interface and recorded by a specific readout software. With this complete readout mechanism a time resolved single-strip readout is possible.

3.3 Readout Software and Signal Analysis

For the data recording two different software setups are used which both remove noise and filter signals. One possibility is the data recording using Micromegas DAQ (mm-daq) [16] and the other is presented in [17]. In both cases the measurement results are saved as root-files which are analyzed by a software written by Bernhard Flierl. In the root-trees information about the measured charge per strip and the timing are saved which are post-processed in the analyses. The shape of a single strip signal is shown in figure 3.5.

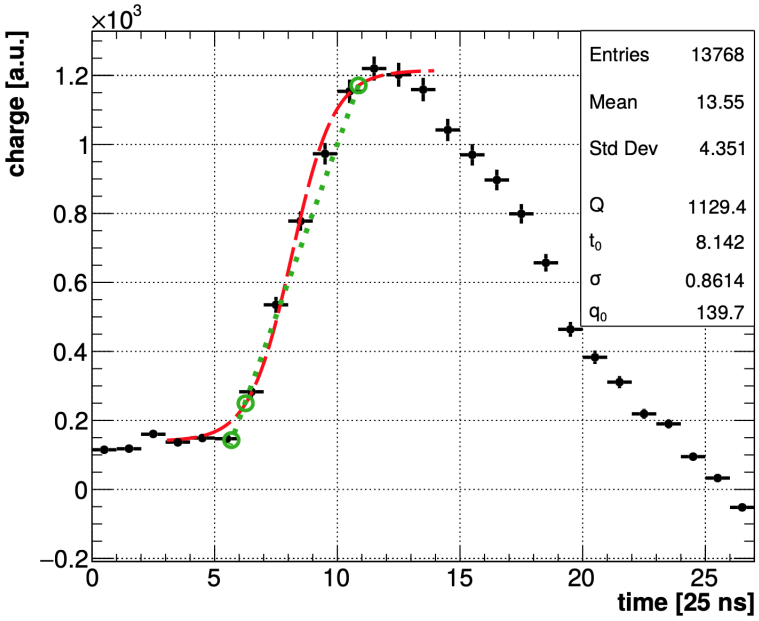

Figure 3.5: Single strip signal fit with a Fermi function (red function) (exemplary, taken from [17]).

The signal rise is characterized by an inverse Fermi function:

$$q(t) = \frac{Q}{1 + e^{\frac{t-t_0}{\sigma}}} + q_0 \tag{3.1}$$

where Q is the maximum of the charge distribution, t_0 the point of inflection, σ a measure for the rise time and q_0 the offset from the baseline [17]. The signals are characterized by their rise time which is described by the fitting parameter σ and the maximum charge Q. For $\sigma > 3\,\text{ns}$ or $Q > 500\,\text{a.u.}$ the signal is counted and otherwise rejected. In nearly all cases a signal is induced to more than one strip due to the amplification process, lateral diffusion or charge sharing. Consequently, adjacent hit signal strips are combined into clusters. If only one strip is hit and their neighboring ones not, it is most likely noise which is removed in the analysis. The cluster is characterized by its charge

$$Q_{\text{cluster}} = \sum_{\text{strips}} q_{\text{strip}} \tag{3.2}$$

and its position which is determined using the centroid method. With this method the particle hit position is reconstructed by weighting the position of each strip x_{strip} with the deposited charge q_{strip} leading to the charge weighted mean hit position

$$x_{\text{cen}} = \frac{\sum_{\text{strips}} x_{\text{strip}} \cdot q_{\text{strip}}}{\sum_{\text{strips}} q_{\text{strip}}} \tag{3.3}$$

which is used for further investigations.

Chapter 4

Simulation Software

Different simulations are performed to understand the physical processes in the detector. Therefore, various simulation software packages are necessary which are introduced in this chapter: Geant4, ANSYS and Garfield++. In the next chapters different combinations of these simulation packages are used for predictions and comparison with measurement results.

4.1 Geant4

Geant4 (see [18]) is a tool-kit developed at CERN. It is specialized on the interaction of particles with matter. With its help it is possible to simulate processes in the detector causing ionization charge. Primary as well as secondary electrons are taken into account. The basis of this simulation is a complete modeling of the detector including the correct dimensions and materials. The incoming radiation and physical processes are defined. After that, the position and momentum of the ionization electrons are calculated and can be extracted.

4.2 ANSYS

Using ANSYS, a software for finite-element analysis (see [19]), a three-dimensional detector geometry is created. Additionally, voltage boundaries are set and ANSYS calculates the corresponding electric field. Finally, the electric field for the whole geometry is extracted.

4.3 Garfield++

Garfield++ (see [20]) is a software tool-kit especially developed for gaseous detectors. It simulates ongoing physical processes like ionization, the influence of an electric field on electrons and ions and corresponding transport mechanism in the gas. The ionization processes can either be simulated by the so-called HEED program (see [21]) or with Geant4 (see subsection 4.1). If necessary, in this thesis ionization is included via Geant4. The needed information is then imported to Garfield++. Garfield++ utilizes the electric field line configuration computed by ANSYS (see subsection 4.2). For the calculation of the drift and amplification the MAGBOLTZ simulation package is used. The MAGBOLTZ software (see [22]) calculates the electron transport properties in the gas by solving the Boltzmann transport equation. For this calculation MAGBOLTZ has access to a large database with the necessary physical properties like energy loss, excitation levels and cross sections for a large variety of gases. As a result information about drift velocity, diffusion and the Townsend avalanche coefficient (see subsection

2.3) are provided.

Chapter 5

Improvement of the Photon Detection Efficiency

Gaseous detectors exhibit only a relative low quantum yield for neutral particles due to the small density of the converter. The aim of this chapter is to improve the photon detection efficiency by optimizing the cathode design.

5.1 Theoretical Principle

Electrically neutral particles like photons can be detected with gaseous detectors. As described in section 2.1.2 they interact with the detector creating electrons which are amplified and detected. But due to the low density of the gas these detectors only have a poor detection efficiency. It can be improved by increasing the interaction probability of the incoming particles with the detector medium. In this chapter the focus lies on the detection of photons with energies of 6 keV and of about 50 keV. While 6 keV photons mainly cause ionization in the gas, the interaction probability decreases with increasing photon energy according to equation 2.4. Consequently, in this thesis a detection configuration is optimized to increase the detection efficiency of photons with an energy of about 50 keV. According to figure 2.1 for 50 keV photon energy the photoelectric effect dominates in Argon (pink line in figure 2.1). There are two main factors influencing the photon conversion efficiency: On the one hand the interaction probability is described by the cross section σ_{ph} which has strong dependence on the atomic number Z of the material: $\sigma_{\text{ph}} \sim Z^5$ (see equation 2.4). But on the other hand, also the density ρ of the material has a huge impact on the conversion probability. An increased density e.g. by using a solid converter layer instead of gas, leads to a higher mass absorption coefficient according to equation 2.3. Both aspects improve the photon conversion efficiency. That is the reason why in gaseous detectors typically solid converter cathodes with high-Z coating are used for photon detection. Additionally, an optimized layer thickness is needed since a thick layer improves the conversion efficiency but lowers the electron extraction probability [23]. Thus, this chapter discusses a further improvement of the photon conversion efficiency by using not one but multiple solid converter layers with high-Z coating.

To optimize the photon conversion efficiency a proper design for the multiple layers is needed. Therefore, a simulation with Geant4 (see section 4.1) is carried out where the whole detector setup is modeled (see figure 5.1), and the conversion probability can be determined.

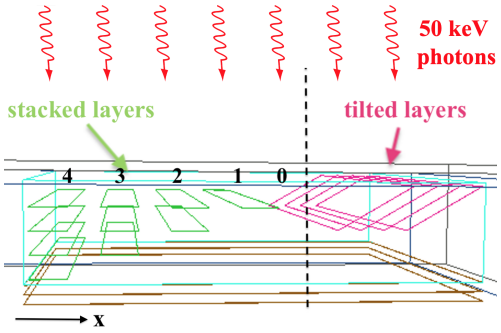

Figure 5.1: Geant4 Simulation: Detector setup with one to four stacked layers (left) and four tilted layers (right) made of 20 µm copper. It is irradiated homogeneously with 50 keV photons.

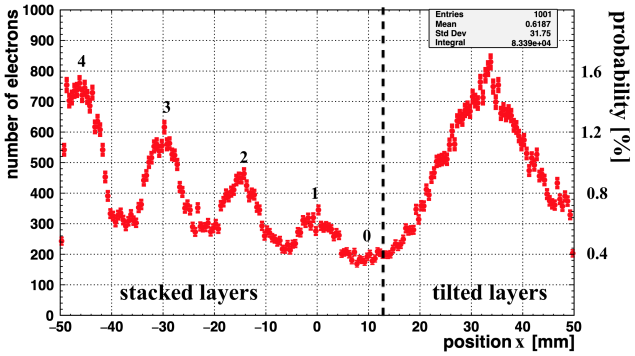

Figure 5.2: Geant4 Simulation: Number of created electrons (left y-axis) and conversion probability (right y-axis) for the stacked (left) and tilted (right) layer setup. With the tilted layer design, the conversion probability can be increased similar to the stacked layout but the extraction of the electrons seems easier.

The conversion layers can either be stacked or tilted as shown in figure 5.1. For comparison there are one to four stacked layers (left side) and four 60° tilted layers (right side). Each layer is made of 20 µm copper. Then the whole setup is irradiated with 50 keV photons and the number of created electrons in the gas volume (light blue box in figure 5.1) is counted. In Figure 5.2 the simulation results are presented. It shows the number of created electrons and the corresponding conversion probability for the stacked and tilted layer setup. The conversion efficiency of the four tilted layers corresponds to about four stacked layers. The conversion probability can be increased by a factor of about 2.5 for the four layers compared to a single converter layer. According to this simulation it is possible to increase the photon conversion probability by using multiple converter layers which are stacked or tilted inside the detector.

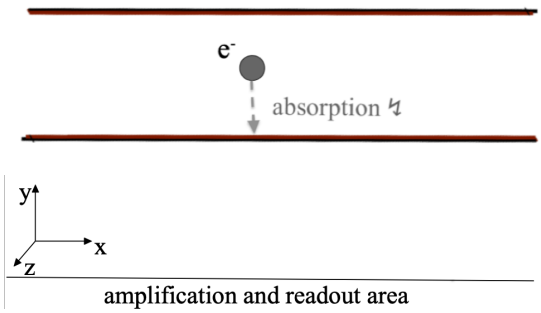

Figure 5.3: Stacked layers: The created electron is absorbed by the following layer and cannot be detected. This design is more difficult to use.

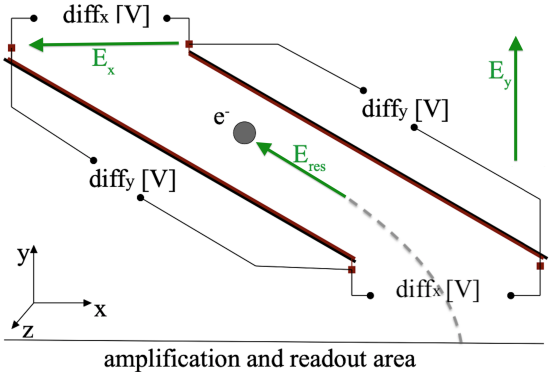

Figure 5.4: Tilted layers: The created electron can be guided with an electric field E_{res} to the amplification and readout area for detection. This is achieved by applying a voltage difference between top and bottom of one layer ($diff_{\mathrm{y}}$) and the left and right layer ($diff_{\mathrm{x}}$).

If an incoming photon interacts with one layer and the created photoelectron can leave this layer, it might be located between two layers of the stacked (figure 5.3) or tilted (figure 5.4) setup. For detection the electron has to drift to the amplification and readout area of the used detector. If the layers are stacked, the electron will more likely be absorbed by the following layer as it can be seen in figure 5.3. With the tilted layer design a created electron can leave its position between both layers. Figure 5.4 shows the electron guiding principle. The electron movement is influenced by an electric field E_{res}. It is a superposition of the electric field E_{x} which is created through a voltage difference $diff_{\mathrm{x}}$ between the left and right layer and E_{y} caused by a voltage difference $diff_{\mathrm{y}}$ between top and bottom of one layer. Finally, the created electrons drift anti-parallel to E_{res} and can be guided to the amplification and readout area using the proper voltage combination of $diff_{\mathrm{x}}$ and $diff_{\mathrm{y}}$. From now on in this chapter the coordinate system shown in figure 5.4 is used including the axis labeling of several histograms. To improve the photon conversion probability with this tilted layer design, the number of converter layers in the particle's path has to be maximized.

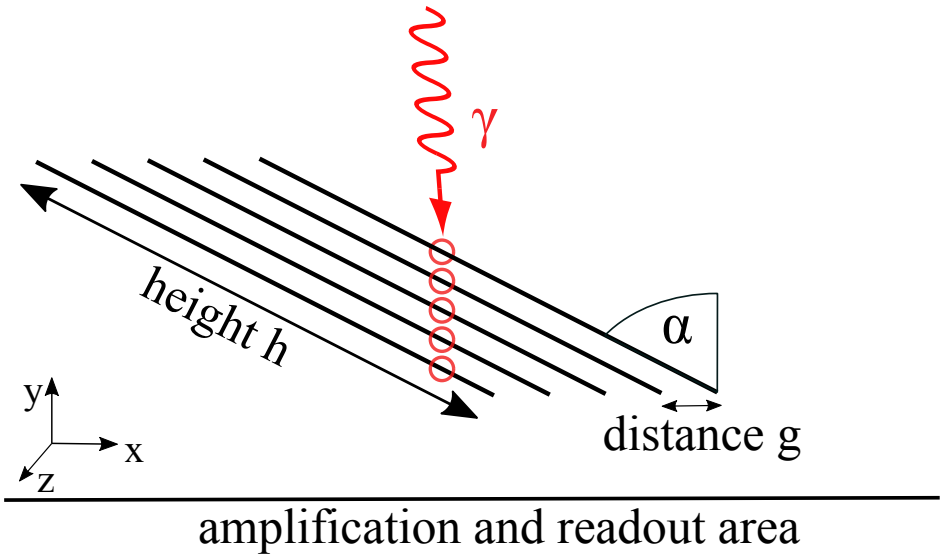

Figure 5.5: The photon conversion can be increased by maximizing the number of converter layers in the particle's path which depends on the height h, the distance g and the tilting angle α. Here the incoming photon γ could interact with one of five converter layers (red circles).

As shown in figure 5.5, five converter layers with height h are positioned under a certain tilting angle α and distance g. Because of this arrangement the incoming photon γ has several interaction possibilities (red circles). If an electron is created in an interaction process and can leave the layer it has to be guided to the amplification and readout area by an electric field E_{res} (see figure 5.4). The tilted layers in combination with the electric guidance field act as structured cathode. In this thesis the basic principle of photon conversion and electron guiding using this structured cathode is investigated while the option of three-dimensional position reconstruction is used but not considered for optimization.

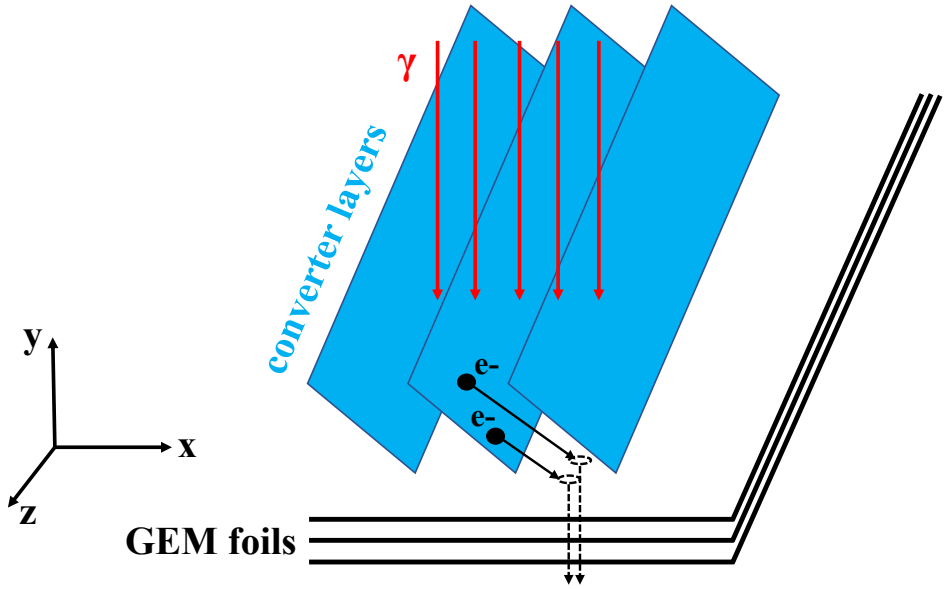

Figure 5.6: The created photoelectrons (black circles) are located between two converter layers. With the electric field E_{res} they are guided to the GEM foils for amplification. The position in x- and z-direction is reconstructed (visualized by the dashed circles). However, this x-position does not correspond to the x-position of the creation point due to the guiding process and no information about the y-position is given.

As shown in figure 5.6 the incoming photons create photoelectrons which are located between two tilted converter layers. Due to the electric field E_{res} they are guided to the three GEM foils for amplification. With this signal the position is reconstructed (see section 3.3) providing information about x- and z-position which is used. But it is not optimized since the reconstructed x-position does not correspond to the x-position where the conversion process takes place due to the electron guiding (see figure 5.6). Additionally, no information about the corresponding y-position is provided. But for future studies regarding the structured cathode it is very interesting and useful to determine the three-dimensional conversion position of the photon for example by using the drift time and pulse height.

5.2 Simulation

To get a better understanding about the on-going processes various simulations are performed using the simulation software introduced in chapter 4. The whole detector setup including the structured cathode and all needed physical processes are simulated in order to optimize the detection efficiency by variation of the setup parameters (like $diff_x$, $diff_y$, g, h and α). First the electron drift is investigated with Garfield++. Therefore, a homogeneous electron distribution between two layers is used. From section 5.2.5 on also the photon conversion is added to the simulation.

5.2.1 Structured Cathode Geometries Created with ANSYS

First, the structured cathode is modeled using the finite-element analysis program ANSYS (see section 4.2). It provides the geometry and simulates corresponding electric field configurations. In total three versions of the geometry are designed always aiming for a more realistic description of the structured cathode and the detector.

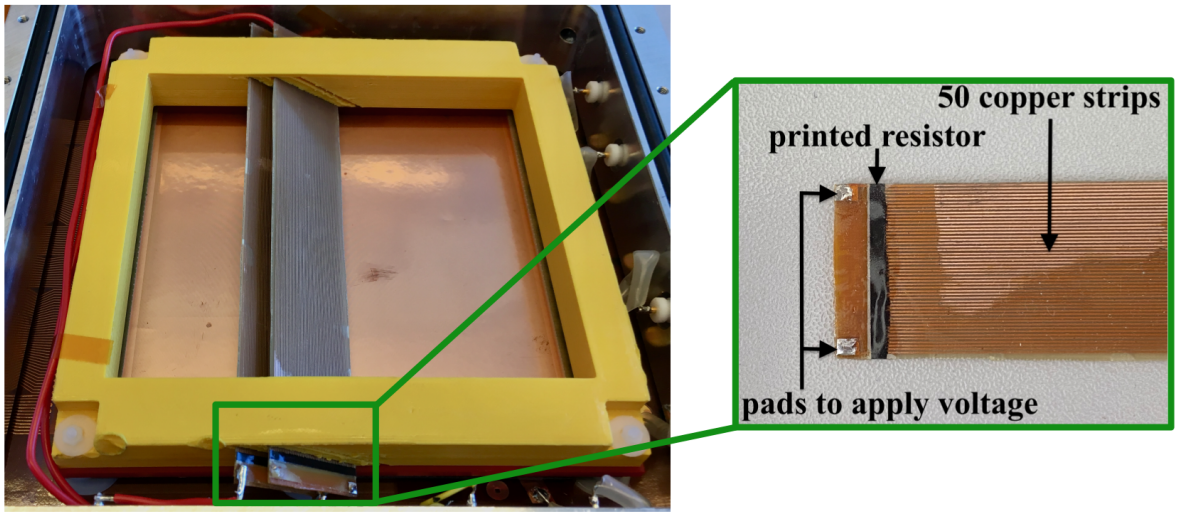

Figure 5.7: The voltage gradient for electron guiding is achieved by a lamella. It consists of a PCB with 50 copper strips (right figure) which are connected with a printed resistor. Applying a voltage difference $diff_y$ on the pads leads to the electric field in y-direction. The lamellae are positioned under $\alpha = 60°$ and $g = 5\,\text{mm}$ inside the detector (left figure).

The first real detector setup shown in figure 5.7 serves as template for the three simulated geometries which are introduced below. In reality this voltage gradient is achieved by a lamella which is shown in figure 5.7 on the right and functions as conversion layer. One lamella consists of a 0.8 mm thick Printed Circuit Board (PCB) with 50 copper strips on each side. Each copper strip is 35 µm thick, has a width of 0.2 mm and a periodicity of 0.4 mm leading to a height $h = 19.8\,\text{mm}$ of the lamella. The copper strips are connected with a printed resistor (production process see Appendix A) which has a resistance between 100 MΩ and 800 MΩ to minimize the current. Due to additional pads on the outer strips an external voltage can be applied leading to the voltage difference $diff_y$ and a corresponding electric field in y-direction. For the electric field in x-direction a voltage difference $diff_x$ between the left and right lamella is applied. Finally, two lamellae are positioned under a tilting angle $\alpha = 60°$ and distance $g = 5\,\text{mm}$ (see figure 5.5) with a mount inside a GEM detector. These parameters are an optimized balance between the number of lamellae in the particle's path and a practicable

realization regarding positioning of the lamellae and placement of the power connections inside the detector. Based on simulation and measurement results, this detector setup will also be modified in course of this chapter. The following geometries are modeled after the setup in figure 5.7.

5.2.1.1 Geometry 1: First Structured Cathode

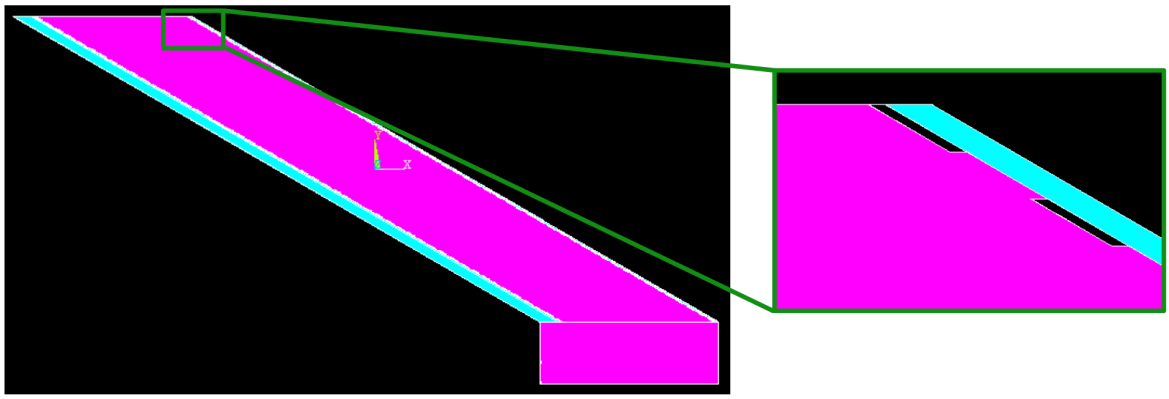

Figure 5.8: The first geometry consists of two PCBs (cyan areas) with 50 copper strips each (small black areas between pink and cyan volumes on the right). Between these lamellae is a gas volume (pink area). A 2 mm high drift volume (also pink) is included at the bottom of the lamellar area. All dimensions of this geometry correspond to the real setup from figure 5.7.

The first structured cathode [24] is presented in figure 5.8. It consists of two PCBs with a thickness of 0.8 mm and height of 19.8 mm. On the PCB 50 copper strips are placed. Each has a thickness of 35 µm, a width of 0.2 mm and a periodicity of 0.4 mm. Both lamellae have a distance of $g = 5\,\text{mm}$, are tilted by $\alpha = 60°$ and are separated by a gas volume. Below the lamellae is the drift area which has a height of $h_{\text{drift}} = 2\,\text{mm}$. All dimensions correspond to the real setup introduced previously. This simulation setup as well as all the following ones are modeled in three-dimensions. The shown areas in figure 5.8 are in reality volumes.

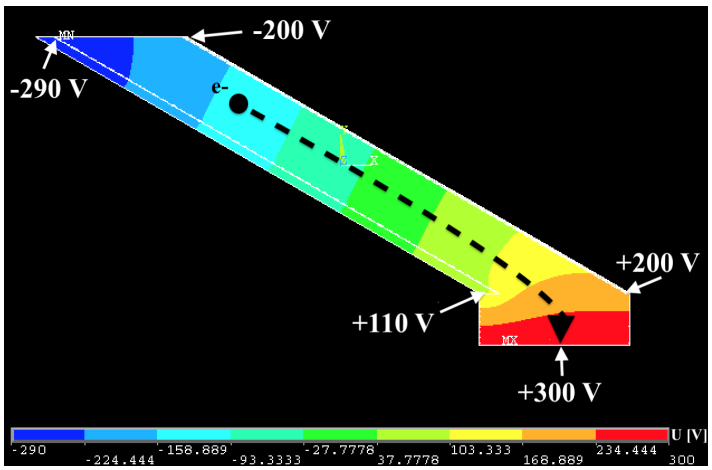

Figure 5.9: Potential distribution for $diff_{\text{y}} = 400\,\text{V}$, $diff_{\text{x}} = 90\,\text{V}$ and $\Delta U_{\text{drift}} = 100\,\text{V}$. The shown equipotential lines are perpendicular to the direction of the electric field $\vec{E}_{\text{res}}$. Since $\vec{E}_{\text{res}} \parallel \vec{v}$ the electron is guided according to the black dashed arrow.

Using the real geometry ANSYS calculates the electric field configuration. The applied voltages are shown in figure 5.9. Between top and bottom of one lamella the voltage difference is $diff_y = 400\,\mathrm{V}$ including a linear voltage distribution for all copper strips leading to an electric field in y-direction. For an electric field in x-direction a voltage difference $diff_x = 90\,\mathrm{V}$ between left and right lamella is created. This leads to a resulting 60° electric field E_{res}. Additionally, in figure 5.9 the corresponding potential distribution is presented. The direction of the electric field $\vec{E}_{\mathrm{res}}$ is always perpendicular to the shown equipotential lines. Since the direction of the electric field $\vec{E}_{\mathrm{res}}$ is anti-parallel to the drift velocity of an electron $\vec{v}$ ($\vec{E}_{\mathrm{res}} \parallel \vec{v}$) the electron is guided outside of the gas volume between both lamellae into the drift area. Due to a voltage difference $\Delta U_{\mathrm{drift}} = 100\,\mathrm{V}$ between the bottom of the right lamella and the bottom of the drift area it drifts further down to the bottom of this drift area where in reality the amplification area of the GEM detector starts.

5.2.1.2 Geometry 2: Structured Cathode in Gaseous Environment

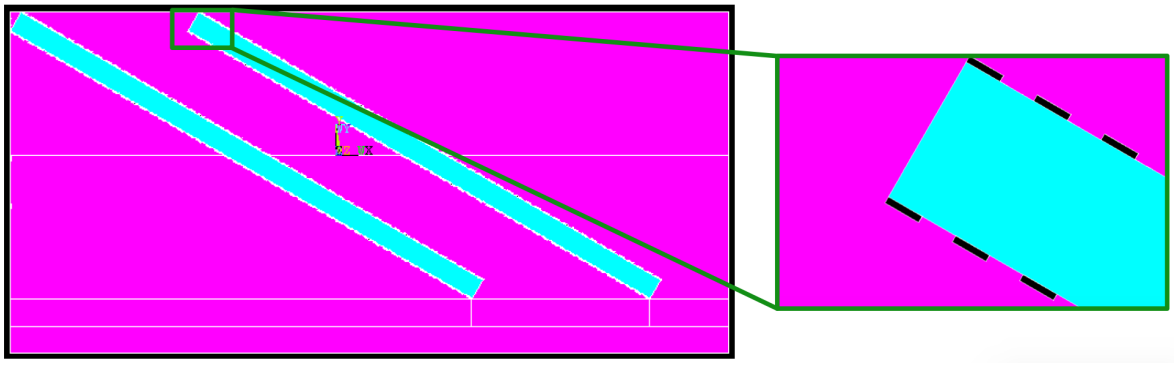

Figure 5.10: This geometry is closer to reality than the previous one. As shown on the left both lamellae are now completely embedded in the gas volume (pink). There is also a change in the lamella design (right figure) which still consists of a PCB (cyan) and 50 copper strips (black). But the geometric arrangements changed compared to the right figure of 5.8 e.g. the lamellae and copper strips are now rectangular.

Compared to the previous geometry from figure 5.8 some changes and extensions are made in the simulation as shown in figure 5.10. First, new gas volumes on the left and right of the lamellae are added. As in reality both lamellae are now completely surrounded by gas (figure 5.10 on the left). There is also a change in the lamella geometry that can be seen on the right figure. It still consists of a PCB with 50 copper strips. But the geometry, especially the angle of the corners, is adapted to be more realistic. Moreover, the copper strips are now added to both sides of one lamella. All dimensions are the same as before.

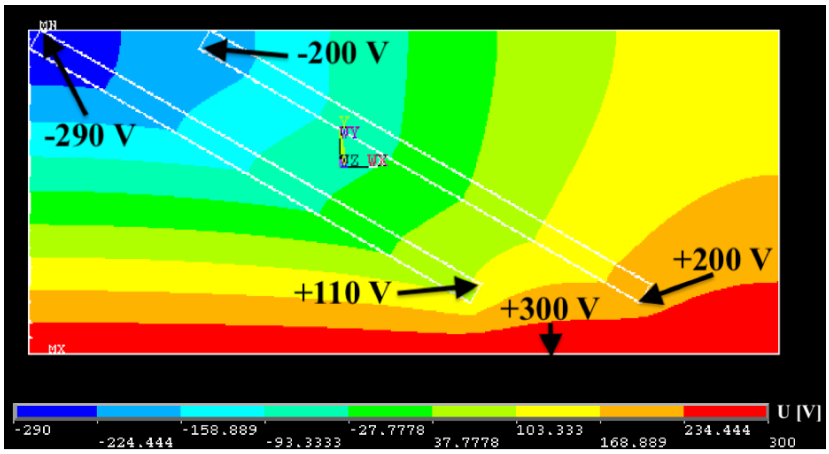

Figure 5.11: Potential distribution for $diff_y = 400\,\mathrm{V}$, $diff_x = 90\,\mathrm{V}$ and $\Delta U_{\mathrm{drift}} = 100\,\mathrm{V}$. Although the same voltages are applied as in figure 5.9 the equipotential lines differ.

Now, the voltage differences $diff_y = 400\,\mathrm{V}$, $diff_x = 90\,\mathrm{V}$ and $\Delta U_{\mathrm{drift}} = 100\,\mathrm{V}$ are applied to the new geometry leading to a corresponding potential distribution. Both can be seen in figure 5.11. On both sides of one lamella copper strips are implemented, but only to the inner ones a voltage is explicitly applied for a better comparison to the previous geometry. If the voltage is applied to all copper strips, the resulting equipotential lines look similar to the ones in figure 5.36. Although the same voltages are used as for the first geometry (see figure 5.9) the equipotential lines differ. According to the previous explanation this influences the movement of the electron between both lamellae and its probability to leave the lamellar area.

5.2.1.3 Geometry 3: Structured Cathode in a GEM detector

Until now only the structured cathode and its gaseous environment are modeled as realistic as possible. But in reality, it is placed inside a GEM detector (see figure 5.7). To examine the influence of a GEM detector the surface at the bottom of the drift area is replaced by a GEM foil.

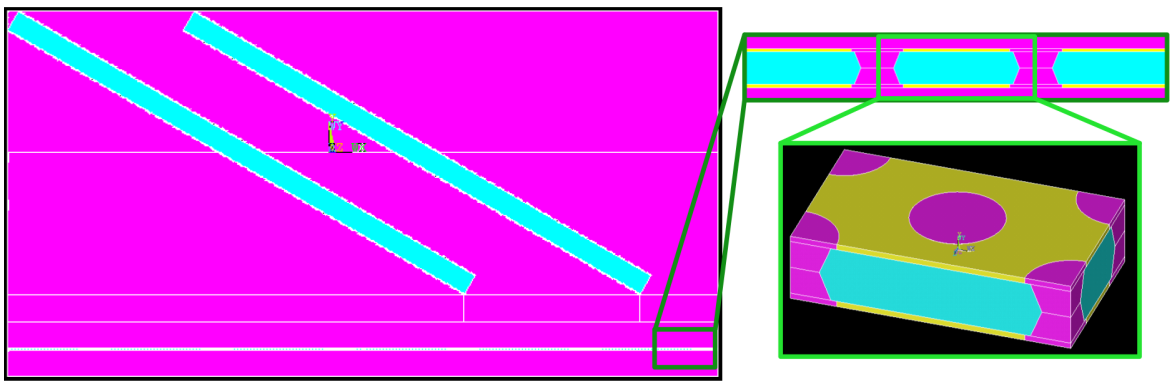

Figure 5.12: The preliminary setup from figure 5.10 is used and extended by a GEM foil which is shown on the right side on the top. It consists of several GEM unit cells (bottom figure) which are made of a Kapton layer (cyan volume) covered by a copper layer on top and bottom (yellow volumes). The pink volumes represent the gas holes. An induction area of $h_{\mathrm{ind}} = 1\,\mathrm{mm}$ is added below the GEM foil (lowest pink volume on the left).

The extended geometry is shown in figure 5.12. Compared to the previous geometry from figure 5.10 the structured cathode, the surrounding gas volumes and the drift area with a height of $h_{\text{drift}} = 2\,\text{mm}$ are identical. The main difference is the added GEM foil which can be seen in detail on the right of figure 5.12. In the upper right the GEM foil is shown which is made of several GEM unit cells (bottom figure) covering the complete bottom side of the setup. As in reality (see section 3.1) one unit cell is made of a 50 µm thick Kapton layer covered by a 5 µm thick copper layer on top and bottom. The gas holes in the GEM foil are positioned with a distance of 140 µm and have three different diameters: an inner diameter of 50 µm, an outer diameter of 70 µm and a rim diameter of 80 µm at top and bottom. Below the GEM foil is the induction area with $h_{\text{ind}} = 1\,\text{mm}$.

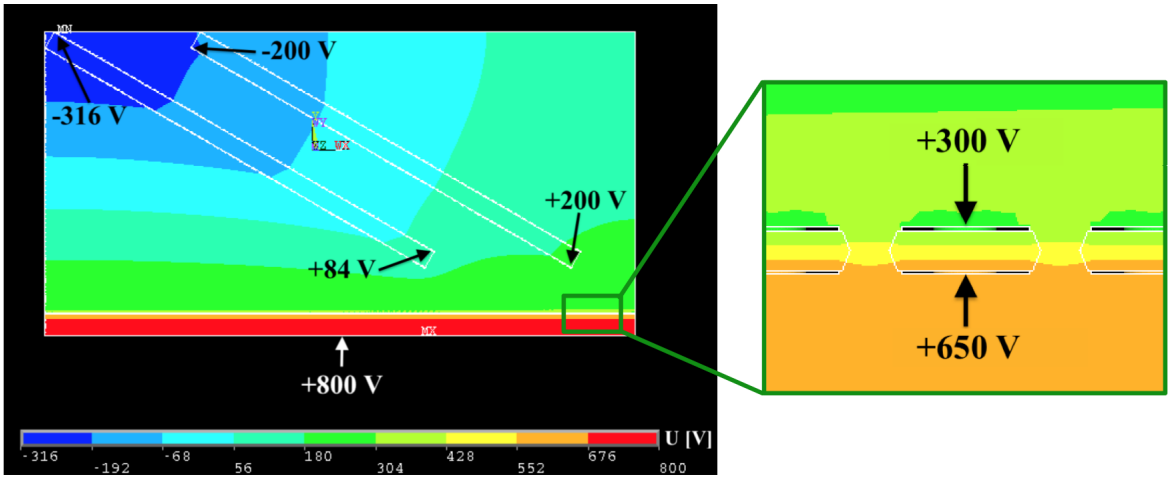

Figure 5.13: Additional voltages are applied at the GEM foil and below the induction gap. Besides $diff_{\text{y}} = 400\,\text{V}$, $diff_{\text{x}} = 116\,\text{V}$ and $\Delta U_{\text{drift}} = 100\,\text{V}$ there are also the voltage difference $\Delta U_{\text{GEM}} = 350\,\text{V}$ and $\Delta U_{\text{ind}} = 150\,\text{V}$. The total resulting potential distribution is shown on the left while the one for the GEM foil can be seen on the right.

As before, a voltage difference $diff_{\text{y}} = 400\,\text{V}$ is applied at the inner copper strips of both lamellae but this time $diff_{\text{x}} = 116\,\text{V}$. For amplification a voltage difference between the top and bottom copper layer of the GEM foil is necessary which is $\Delta U_{\text{GEM}} = 350\,\text{V}$. Additionally, there is $\Delta U_{\text{drift}} = 100\,\text{V}$ between the bottom side of the right lamella and the top side of the GEM foil (drift area) as well as $\Delta U_{\text{ind}} = 150\,\text{V}$ between bottom side of the GEM foil and the bottom side of the induction area. All applied voltages and the resulting potential distribution are shown in figure 5.13 for the complete geometry on the left and for the GEM foil on the right.

5.2.2 Electron Guiding Simulated with Garfield++

For all three designs the geometry and the electric field configuration generated with ANSYS are imported to Garfield++ (see section 4.3) where the influence of the electric field on the electron guiding can be examined.

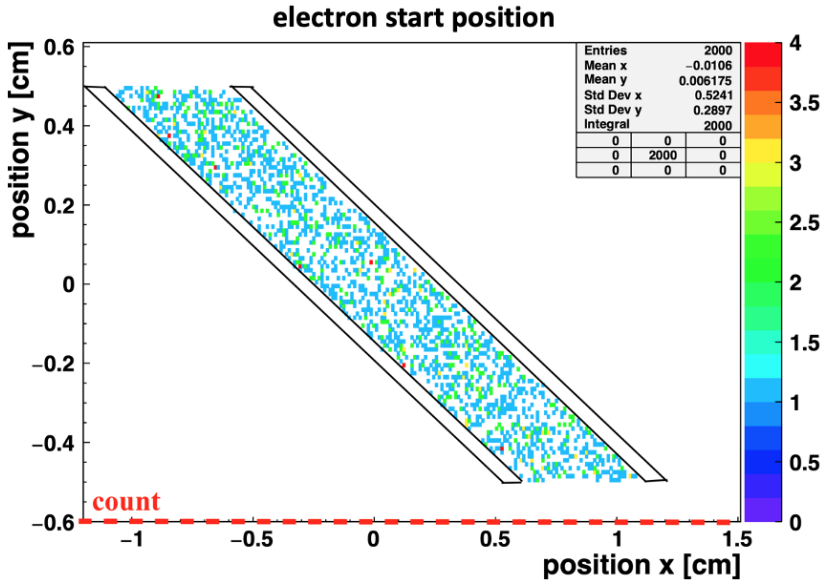

Figure 5.14: In Garfield++ electrons are randomly generated between both lamellae (not drawn to scale) with zero kinetic energy. The electric field guides some electrons out of the lamellar area while others are absorbed. At the end the number of electrons passing $y = -0.6\,\text{cm}$ are counted as extracted electrons.

Therefore, a certain number of electrons is randomly generated in the gas volume between both lamellae (in x and y-direction) as shown in figure 5.14 with zero kinetic energy. Although the electrons start at the position $z = 0$ the whole geometry is periodically extended in z-direction to guarantee a sufficient large volume size in this direction. This is also done with Garfield++. Due to the electric field the electrons are either guided out of the lamellar area or are absorbed by one of them. An electron is counted when it passes the position value $y = -0.6\,\text{cm}$ (see figure 5.14). Depending on the used geometry different parameters have to be taken into account.

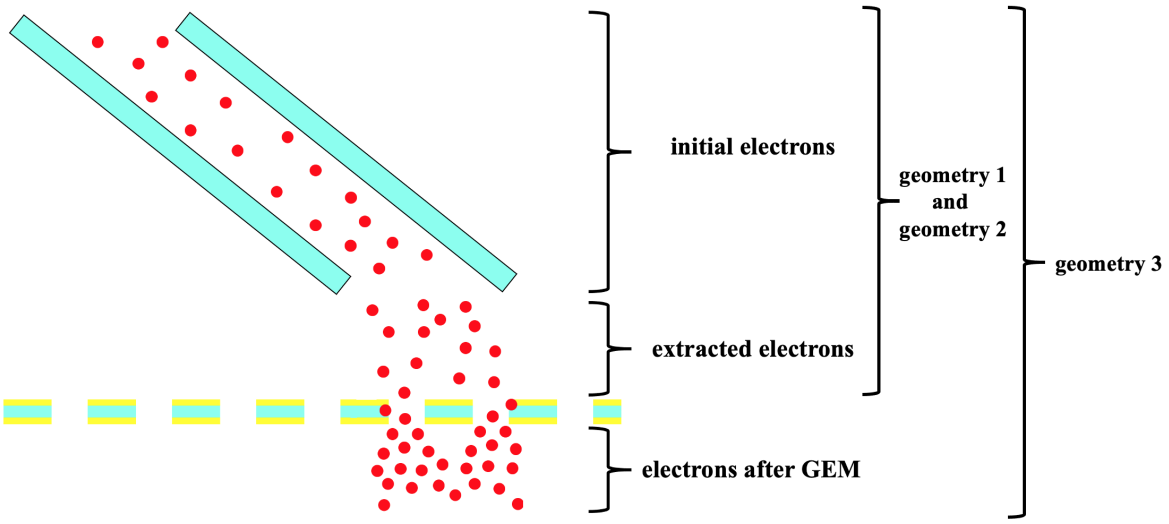

Figure 5.15: For all three geometries the electron guiding efficiency is defined as the number of extracted electrons divided by the number of initial electrons (red dots). Only for geometry 3 the influence of the GEM foil has to be considered. A certain number of electrons can pass the GEM foil and are counted as electrons after the GEM.

Figure 5.15 gives an overview of the different geometries and the corresponding parameters. For all three geometries initial electrons are created between both lamellae. Depending on the electric field a certain number of electrons can be guided out of the lamellar area. As described above an extracted electron has to pass the value $y = -0.6\,\mathrm{cm}$ to be counted. Both parameters lead to the electron guiding efficiency

$$\text{electron guiding efficiency} = \frac{\text{extracted electrons}}{\text{initial electrons}} \tag{5.1}$$

which is calculated for all three geometries. Consequently, the electrons guiding efficiency is used to compare the geometries. Only in geometry 3 the GEM foil is included which amplifies the extracted electrons. The GEM amplification factor is:

$$\text{GEM amplification factor} = \frac{\text{electrons after GEM}}{\text{extracted electrons}} \tag{5.2}$$

The number of electrons after the GEM is supposed to be larger than before the GEM for correct voltages. Nevertheless, there are always electrons which are absorbed by the GEM foil. The folding of the electron guiding efficiency and the GEM amplification factor leads to the total amplification factor

$$\begin{aligned} \text{total amplification factor} &= \text{electron guiding efficiency} \times \text{GEM amplification factor} \\ &= \frac{\text{extracted electrons}}{\text{initial electrons}} \times \frac{\text{electrons after GEM}}{\text{extracted electrons}} \\ &= \frac{\text{electrons after GEM}}{\text{initial electrons}} \end{aligned} \tag{5.3}$$

With these parameters the simulated processes for each geometry are quantified.

5.2.3 Results of Electron Guiding for Different Geometries

Finally, the simulation is performed for all three geometries and the results are compared. In all cases the focus is on the electron guiding efficiency which should be maximized. This is achieved by finding an optimal voltage combination $diff_{\mathrm{x}}$ and $diff_{\mathrm{y}}$. Furthermore, the advantages and differences between the geometries are emphasized with the aim of finding the most suitable geometry which can be used for comparison with measurements.

5.2.3.1 Geometry 1: First Structured Cathode

For the first structured cathode a correlation between $diff_{\mathrm{x}}$ and $diff_{\mathrm{y}}$ can be found for an optimized electron guiding efficiency. Each voltage combination leads to a resulting electric field E_{res} which defines the movement of the electrons. They drift anti-parallel to E_{res}. The orientation of E_{res} is determined by the guiding angle θ as shown in figure 5.16.

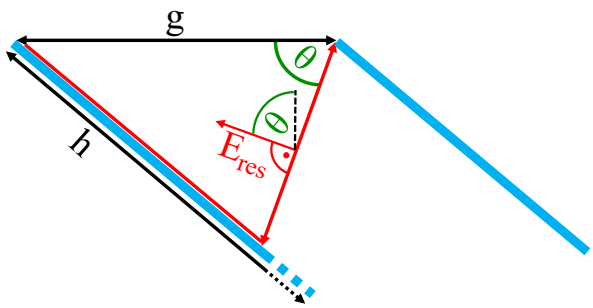

Figure 5.16: Due to the applied voltages $diff_x$ and $diff_y$ equipotential lines between the left and right lamella are created (red arrow). The resulting electric field E_{res} is always perpendicular to this equipotential line and its orientation is defined by the guiding angle θ. For a general consideration $\theta \neq \alpha$ but later θ should be equal to the tilting angle α in the ideal case.

Each voltage combination $diff_x$ and $diff_y$ results an equipotential line which determines the guiding angle θ and therefore directly the resulting electric field E_{res} which is always perpendicular to this equipotential line influencing the electron guiding efficiency. From a geometrical consideration of these relations follows for the guiding angle θ:

$$\theta = \alpha + \arctan\left(\frac{\frac{h \cdot diff_x}{diff_y} - g \cdot \sin(\alpha)}{g \cdot \cos(\alpha)}\right) \tag{5.4}$$

which is shown in more detail in Appendix B. It only depends on known quantities like the voltage pair $diff_x$ and $diff_y$, height h, distance g and tilting angle α.

It is expected that most of the electrons are guided out of the lamellar area if the electric field is oriented parallel to both lamellae. For this case the guiding angle is $\theta = \alpha$ and the equipotential lines are oriented perpendicular to the lamellae. Consequently, for the maximum guiding efficiency a correlation for the proper voltage pair $diff_x$ and $diff_y$ is found:

$$diff_x = \frac{g \cdot \sin(\alpha)}{h} \cdot diff_y \tag{5.5}$$

(see Appendix B). Inserting the dimensions from the geometry $h = 19.8\,\text{mm}$, $g = 5\,\text{mm}$ and $\alpha = 60°$ (compare section 5.2.1) into equation 5.5 leads to

$$diff_x = 0.219 \cdot diff_y \tag{5.6}$$

These theoretical expectations are now compared to the simulation results.

In the simulation for the first structured cathode geometry (see figure 5.8) the voltage between top and bottom of one lamella is fixed at a certain $diff_y$ value while the voltage difference between both lamellae $diff_x$ is varied. For each voltage combination the electron guiding efficiency (see equation 5.1) is calculated and the result is plotted. In general, for all simulations in this chapter the corresponding error bars are determined using the min-max method.

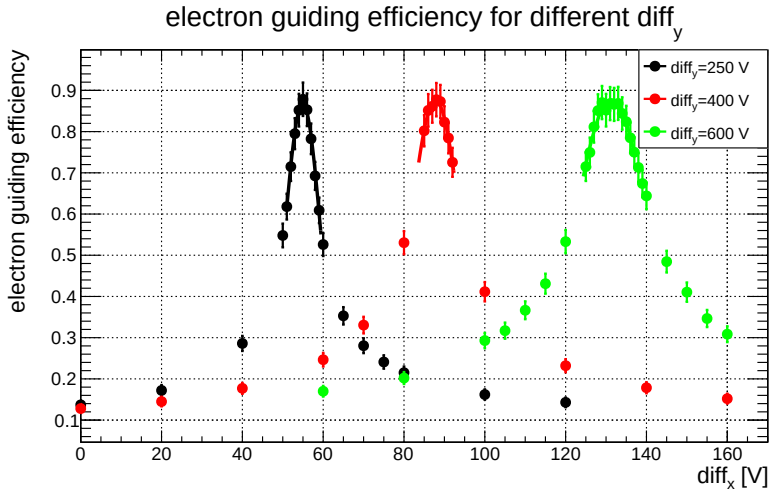

Figure 5.17: For the first structured cathode the electron guiding efficiency shows a clear peak for a fixed $diff_y$ and varied $diff_x$ values. The shape and position of the guiding efficiency peak is influenced by $diff_y$. With higher $diff_y$ the peaks get broader and the maximum efficiency is only reached at higher $diff_x$. But the maximum guiding efficiency stays constant. To all three peaks a Gaussian function is fitted.

The results of the corresponding simulations are presented in figure 5.17. While a fixed $diff_y$ value is set, $diff_x$ is varied which leads to clear electron guiding efficiency peaks. The effect of $diff_y$ on the peak shape and position is visualized for three values: $diff_x = 250\,\mathrm{V}$, $diff_x = 400\,\mathrm{V}$ and $diff_x = 600\,\mathrm{V}$. With higher $diff_y$ the peak width increases and the position of the peak maximum is shifted to higher $diff_x$. Nevertheless, the maximum electron guiding efficiency stays constant at about 88 %. To these and other $diff_y$ peaks a Gaussian function is fitted. The provided fit parameters including their errors are used for further investigations.

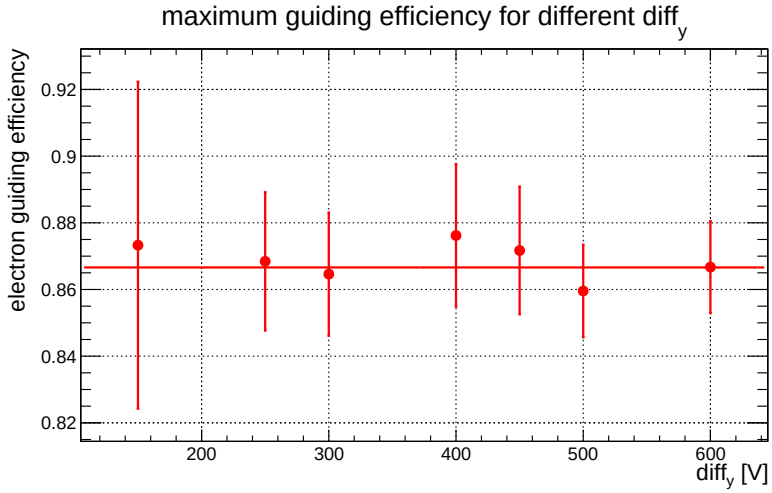

Figure 5.18: For different $diff_y$ the maximum electron guiding efficiency and the corresponding errors from the fit are plotted. The guiding efficiency stays constant within the limits of the error intervals.

First, the maximum electron guiding efficiency is presented in figure 5.18 for different $diff_y$ using the Gaussian fit parameters. For all simulated $diff_y$ the maximum guiding efficiency stays constant at $(86.6 \pm 0.7)\,\%$ within the limits of the simulation accuracy.

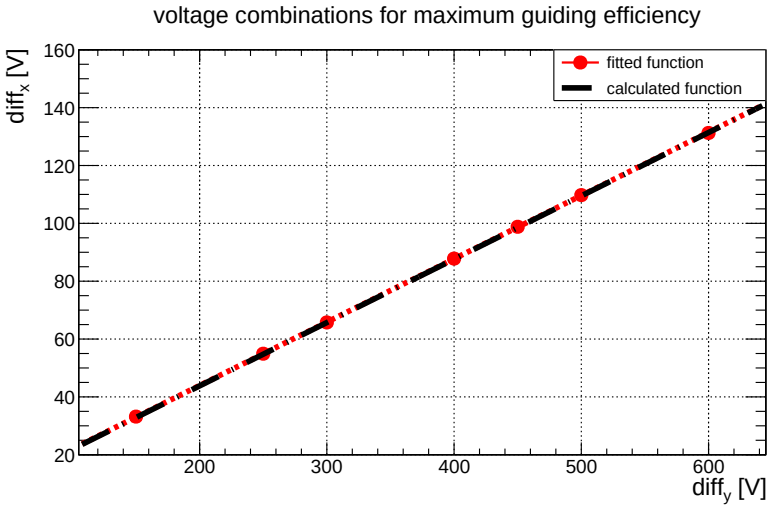

Figure 5.19: The simulated voltage pairs $diff_x$ and $diff_y$ for the maximum electron guiding efficiency are plotted against each other and a linear function is fitted to the simulated points (red function). Also the theoretical function from equation 5.6 is plotted (black function).

In the simulation to every maximum electron guiding efficiency belongs a corresponding $diff_x$ and $diff_y$ voltage pair. These pairs are plotted in figure 5.19 against each other. The values as well as the corresponding errors which are too small to be visible are provided from the Gaussian fit parameter. It results a linear correlation between $diff_x$ and $diff_y$ as expected from equation 5.5. The linear fit leads to

$$diff_x = (0.2189 \pm 0.0009) \cdot diff_y \tag{5.7}$$

with the same slope calculated in equation 5.6 (within the error interval) which is also plotted in figure 5.19. Both linear functions show a very good agreement and are in figure 5.19 nearly indistinguishable. This linear relation is in agreement with the observed peak shift in figure 5.17.

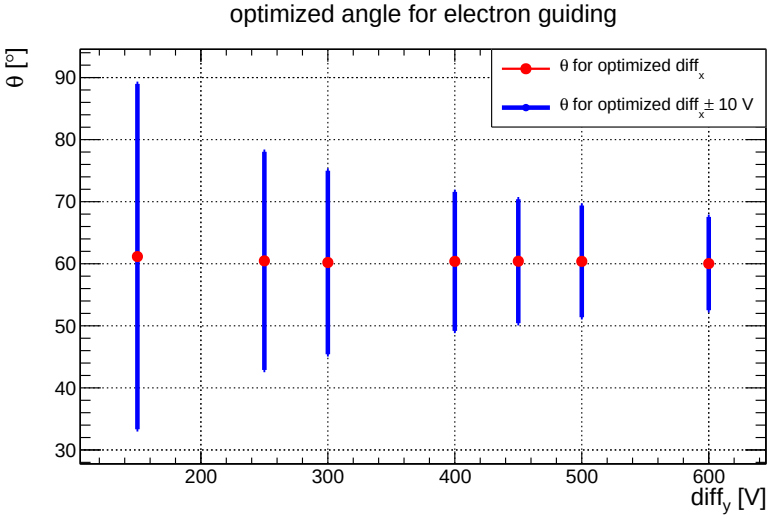

Figure 5.20: For fixed $diff_y$ there is one optimized $diff_x$ for the maximum guiding efficiency. To each of these voltage pairs with optimized $diff_x$ belongs a guiding angle θ which is constant (red dots). A change of this optimized $diff_x$ by $\pm 10\,V$ causes a deviation in the guiding angle θ which also depends on $diff_y$ (blue lines). With increasing $diff_y$ the influence of the variation of θ for optimized $diff_x \pm 10\,V$ decreases.

Additionally, to every voltage pair $diff_x$ and $diff_y$ for the maximum detection efficiency belongs an optimized guiding angle θ. It is calculated using equation 5.4 (with $h = 19.8\,\text{mm}$, $g = 5\,\text{mm}$ and $\alpha = 60°$) and plotted in figure 5.20. As expected, it is constant with $\theta = (60.43 \pm 0.14)°$ and corresponds for optimized guiding efficiency to the tilting angle α. But the tilting angle of 60° does not lie in the error interval of the simulated guidance angle θ because only integer voltage pairs are applied. A deviation from the optimized $diff_x$ by $\pm 10\,\text{V}$ has an impact on the guiding angle θ as shown in figure 5.20. The higher the variation in θ, the less electrons can be extracted leading to a quicker decrease in the electron guiding efficiency. In general, for high $diff_y$ a deviation in $diff_x$ by $\pm 10\,\text{V}$ does not have such a huge impact on the guiding efficiency than for small $diff_y$. Consequently, with increasing $diff_y$ the peaks become broader which can also be seen in figure 5.21.

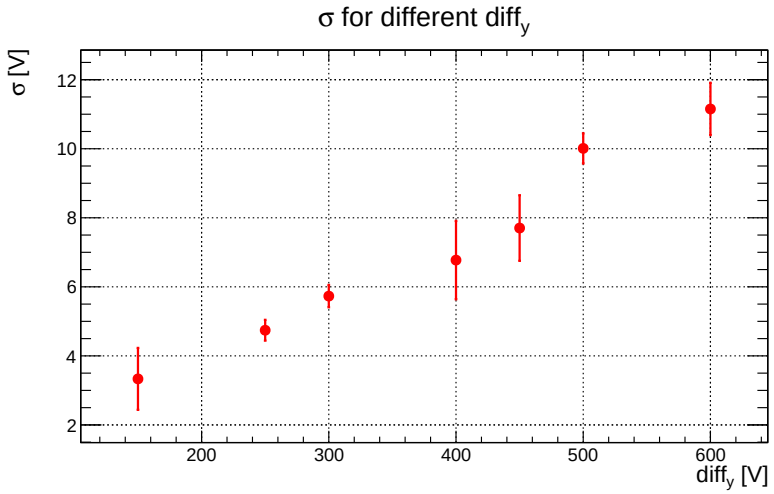

Figure 5.21: All $diff_y$ are plotted against the resulting σ values from the Gaussian fit. With higher $diff_y$ also σ increases.

The width of the electron guiding efficiency peak is described by the fit parameter σ. As shown in figure 5.21 with higher $diff_y$ also the width σ increases resulting in the broadening of the peaks. The reason for this behavior is explained above. For higher $diff_y$ the deviation of the guiding angle θ decreases leading to wider $diff_x$ range with approximately the same guiding efficiency which means a broader peak is observed. Additionally, a higher $diff_y$ allows for a wider $diff_x$ range with the same efficiency which is favorable for measurements.

5.2.3.2 Geometry 2: Structured Cathode in Gaseous Environment

For the second design of the structured cathode the lamella geometry is changed and it is completely surrounded by gas as introduced in figure 5.8. Although the same voltages are applied at geometry 1 and geometry 2, the equipotential lines between both lamellae differ. This can be seen by comparing figure 5.9 and figure 5.11. Since the potential distribution influences the electron guiding for both geometries different electron guiding efficiency peaks are expected. For geometry 2 the same simulation process is performed. While $diff_y$ is fixed at $400\,\text{V}$, $diff_x$ is varied. The resulting electron guiding efficiency peak is shown in figure 5.22 as well as the efficiency peak for the first structured cathode (geometry 1).

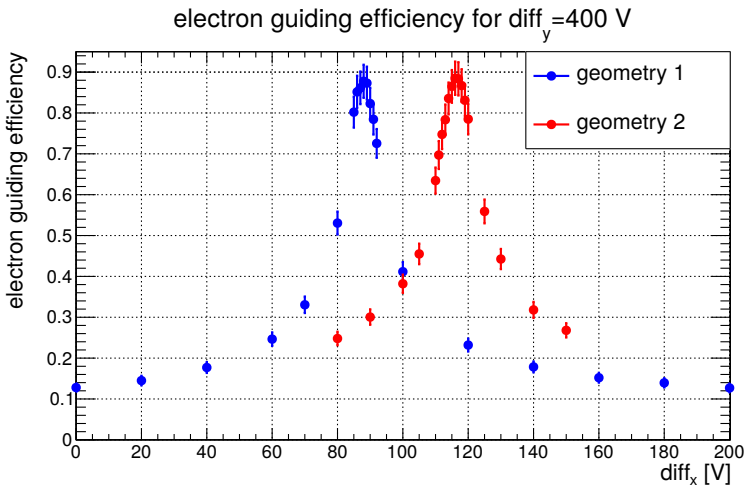

Figure 5.22: For $diff_y = 400\,\mathrm{V}$ the electron guiding efficiency is compared between geometry 1 (blue dots) and geometry 2 (red dots). While the maximum guiding efficiency is constant at 88 %, the peak is shifted from $diff_x = 88\,\mathrm{V}$ to $diff_x = 117\,\mathrm{V}$.

Depending on the used geometry the peak is positioned at different $diff_x$ values. Geometry 1 has a maximum guiding efficiency of 88 % at $diff_x = 88\,\mathrm{V}$ whereas for geometry 2 the maximum of 87 % is reached at $diff_x = 117\,\mathrm{V}$. A peak shift is observed while the maximum guiding efficiency stays almost constant. Thus, at first glance the new $diff_x$ value does not correspond to equation 5.5. But due to the additional gas volumes the boundary conditions for calculation of the electric field configuration in ANSYS changed because each material has another dielectric constant which influences the applied voltages and corresponding electric fields. Consequently, the effective $diff_x$ and $diff_y$ values change due to the dielectric. If these effective voltages with the proper dielectric constants are taken into account, equation 5.5 is still valid resulting in other voltage pairs. This relation emphasizes the observed peak shift from figure 5.22. Since both geometries show different simulation results and geometry 2 is much closer to reality from its appearance than geometry 1, it is used for further investigations.

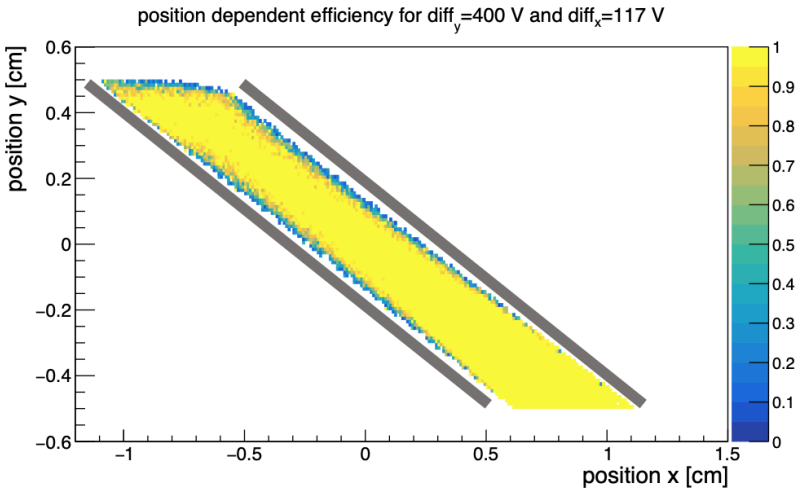

Figure 5.23: Although for $diff_y = 400\,\mathrm{V}$ and $diff_x = 117\,\mathrm{V}$ as many electrons as possible are extracted from the lamellar area, there is still a loss of about 13 %. The extraction probability for this voltage combination depends on the position of the initial electron. The extraction probability decreases for higher y-position.

First, the position dependent electron guiding efficiency which is shown in figure 5.23 is examined. The maximum guiding efficiency for geometry 2 is achieved by applying $diff_y = 400\,\mathrm{V}$ and $diff_x = 117\,\mathrm{V}$ with a loss of about 13 % of the initial electrons. The figure shows how the extraction probability depends on the initial position of the created electrons in the lamellar area and emphasizes where the electrons are lost. On the one hand the electrons created close to the lamella cannot be guided out and are absorbed. But on the other hand, the extraction probability close to the lamella also decreases with increasing y-position. This behavior can be explained with figure 5.24.

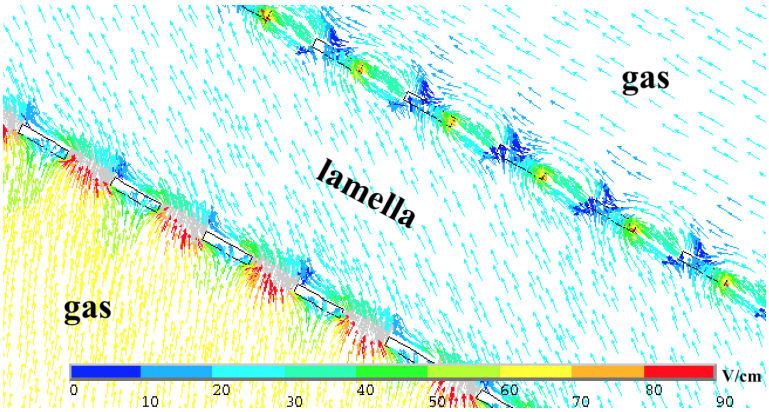

Figure 5.24: The drift direction of the electrons is described by electric field vectors. Here the lower lamella in the gaseous environment is shown. Between both lamellae (upper gas volume) the vectors are oriented parallel to the lamella boundaries. But close to the lamella they show periodic arcs between adjacent copper strips.

In this figure the electric field vectors for $diff_y = 400\,\mathrm{V}$, $diff_x = 115\,\mathrm{V}$ and $\Delta U_{\mathrm{drift}} = 100\,\mathrm{V}$ are shown. For these voltages the electric field vectors between both lamellae are oriented parallel. But due to the periodic copper strip arrangement on each lamella, close to the lamella boundaries the electric field vectors are no longer parallel but show periodic arcs. The electrons drifting close to one lamella are easily absorbed when they diffuse off the line which leads to a decreasing extraction probability.

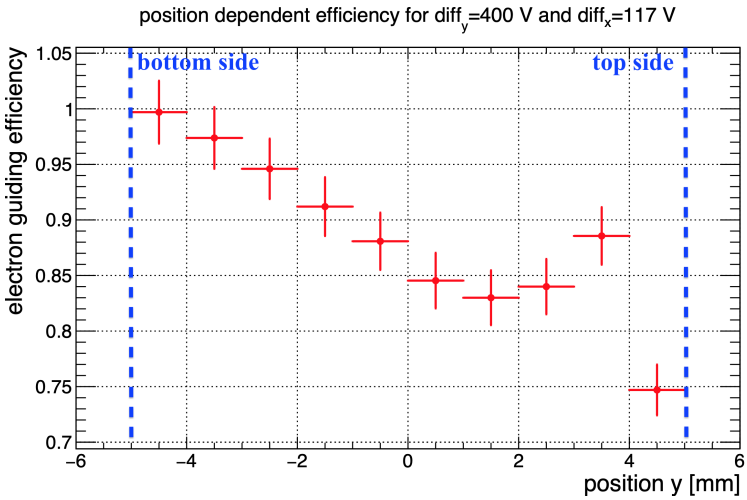

Figure 5.25: The electron guiding efficiency is evaluated from figure 5.23 as a function of the electron start position in y-direction. Apart from two exception values the efficiency decreases with increasing y-position by a total of 25 %.

The electron guiding efficiency is plotted against the y-position in figure 5.25. It is another visualization of figure 5.23. Therefore, the complete y-range of the initially created electrons is divided into ten equally large parts and for each of them the electron guiding efficiency is calculated. Between $y = -5\,\text{mm}$ and $y = 2\,\text{mm}$ the electron guiding efficiency decreases constantly from about 100 % to 80 %. Then it increases again until it falls to 75 % for the initially highest electrons at $y = (4.5 \pm 0.5)\,\text{mm}$. The impression from a decreasing efficiency with increasing y-position from figure 5.23 is confirmed by figure 5.25 apart from two exception values. These two deviations are also visible in figure 5.23 and can be explained with the different equipotential line in figure 5.11 on the top of the left lamella. It has another orientation due to the boundary conditions of the ending gas volume. While between both lamellae the equipotential lines are parallel to each other, the one in the top left right corner is oriented differently (darkest blue in the legend of figure 5.11). Due to the resulting electric field in this area the electrons are first not guided parallel to the lamellae but to the right into the middle of both lamellae. Consequently, the probability that the electrons starting in this area diffuse off the field line and are absorbed by a lamella decreases and more electrons than expected can be guided out. Nevertheless, this correlation can help in measurements to reconstruct the y-position of the conversion process since it depends on the number of extracted electrons which is proportional to the amount of detected charge.

Another aspect that can be investigated is the electron endpoint distribution below the lamellar area. To investigate this the lamella boundaries have to be defined.

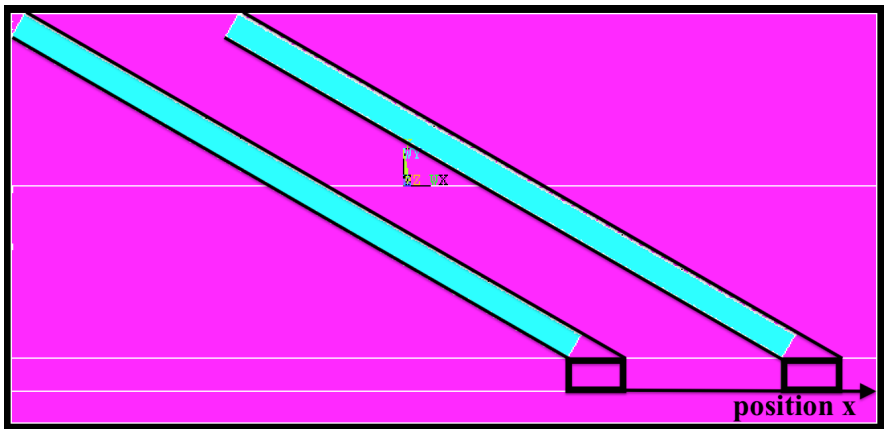

Figure 5.26: The lamella boundaries are defined by the black boxes. Their width is given by the boundaries of the cyan colored lamellar areas (black lines) which are extended up to the drift area. In the histograms from simulations or measurements these lamella boundary boxes are pink.

These boundaries are shown in figure 5.26. The boundaries of the lamellar areas are extended up to the beginning of the drift area where the distance of the lines in x-direction describes the width of each lamella. It is visualized by the black boxes. In all following histograms these boundaries are shown by pink boxes like in figure 5.27.

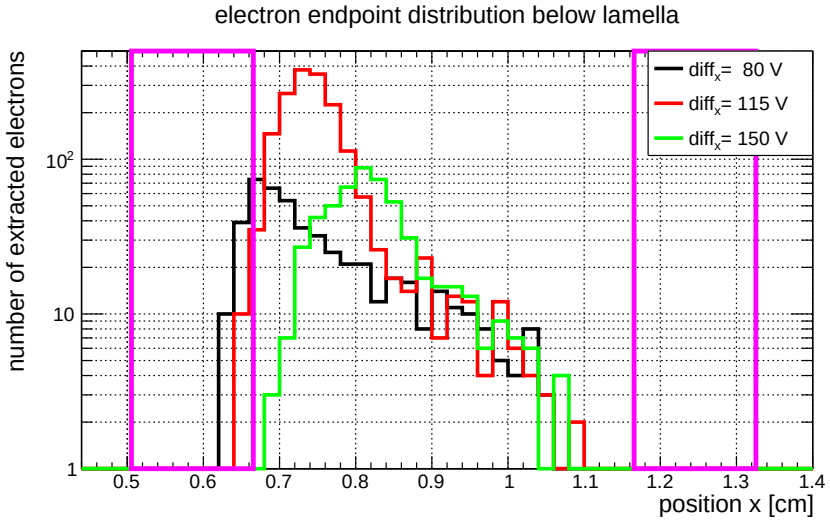

Figure 5.27: The extracted electrons form a peak-shaped distribution below the lamellar area. Its height (logarithmic scale) is a measure for the guiding efficiency for $diff_y = 400\,V$. For all three $diff_x$ the peaks are closer to the left lamella but with increasing $diff_x$ they are shifted to the right.

Figure 5.27 presents the distribution of the extracted electrons below the lamellar area for $diff_y = 400\,V$ and three different $diff_x$: $80\,V$, $115\,V$ (close to maximum guiding efficiency) and $150\,V$. For all these values a peak is observed which is located close to the left lamella. But with increasing $diff_x$ the electrons are dragged towards the right lamella. Consequently, the peak also moves into the direction of the right lamella. Furthermore, the height is correlated to the electron guiding efficiency. The reason for the peak position is shown in the vector plot in figure 5.28.

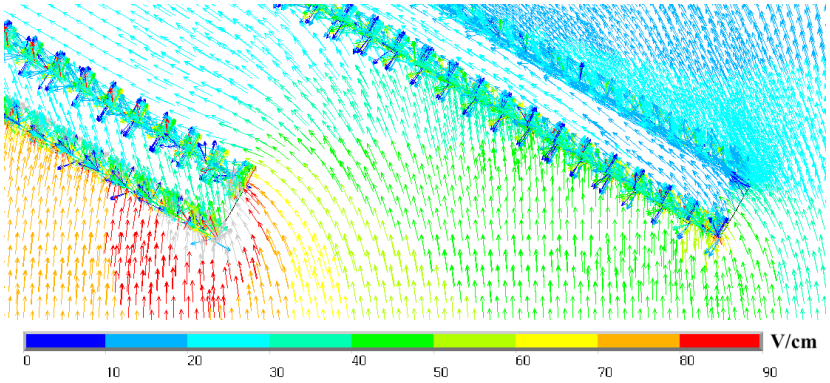

Figure 5.28: The drift direction of the electrons is described by electric field vectors. Between both lamellae these vectors are oriented parallel to the lamella boundaries. After exiting the lamellar area the electrons change their trajectory towards the bottom of the drift area close to the left lamella.

Nearly all electric field vectors starting between both lamellae are oriented parallel to them. But if the electrons exit the lamellar area, they change their trajectories towards the bottom side of the drift area. Since most of the electrons are created between the lamellae, they end close to the left lamella because of this electric field configuration. This behavior explains the observed peak positions in figure 5.27.

5.2.3.3 Geometry 3: Structured Cathode in a GEM detector

Adding a GEM foil and an induction area to geometry 2 is a further adaption to reality and leads to geometry 3 which is introduced in figure 5.12. As previously explained in section 5.2.2 the additional GEM foil leads to an amplification of the extracted electrons. First of all, the electron guiding efficiency for geometry 3 is simulated the same way as for geometry 2.

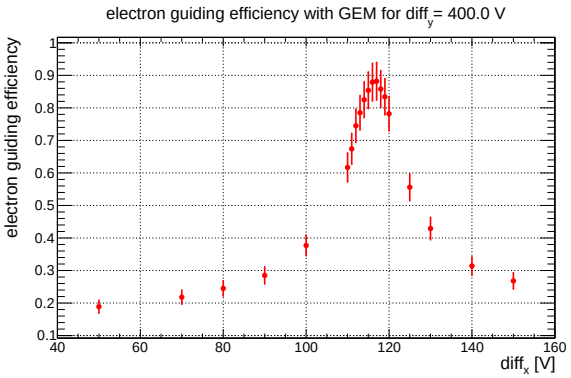

Figure 5.29: With the GEM foil a maximum guiding efficiency of 88 % for $diff_y$ = 400 V and $diff_x$ = 116 V is achieved.

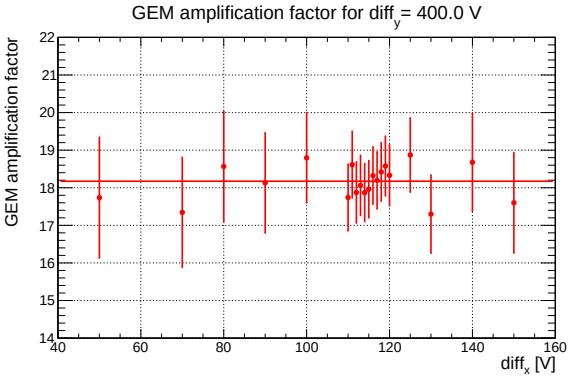

Figure 5.30: The simulated GEM amplification factor (see equation 5.2) has a constant value of 18.2 ± 0.3.

In figure 5.29 the guiding efficiency peak is presented for $diff_y$ = 400 V which reaches its maximum of 88 % at $diff_x$ = 116 V. Additionally, the voltages ΔU_{drift} = 100 V, ΔU_{GEM} = 350 V and ΔU_{ind} = 150 V are applied. Then the GEM foil is examined. Its purpose is the amplification of electrons. In equation 5.2 the corresponding GEM amplification factor is defined and the simulation result is shown in figure 5.30. Within the limits of accuracy the GEM amplification factor has the constant value of 18.2 ± 0.3 as presented in figure 5.30.

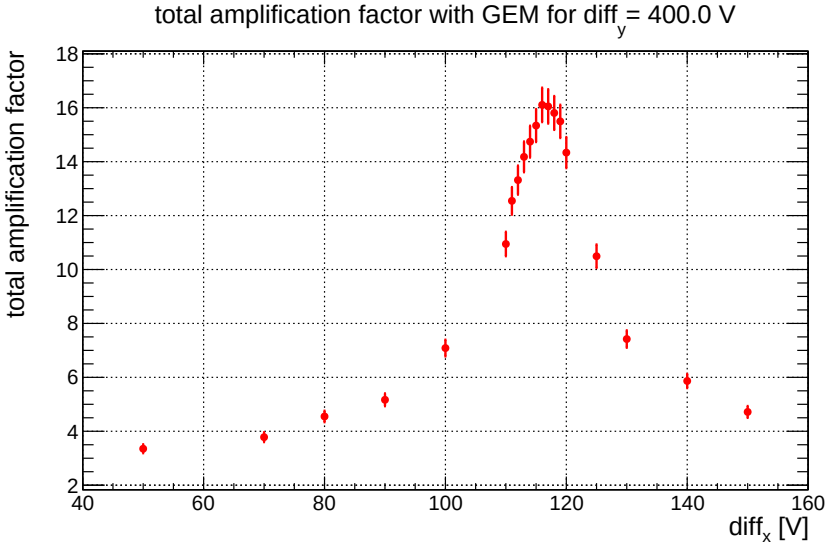

Figure 5.31: The total amplification factor results from the folding of the electron guiding efficiency peak (see figure 5.29) with the constant GEM amplification factor (see figure 5.30). Consequently, it is also peak-shaped.

The folding of the electron guiding efficiency (figure 5.29) and the GEM amplification factor (figure 5.30) leads to the total amplification factor (equation 5.31) which is plotted in figure 5.31. Since the total amplification factor results from the guiding efficiency peak multiplied by the constant GEM amplification factor it is peak-shaped.

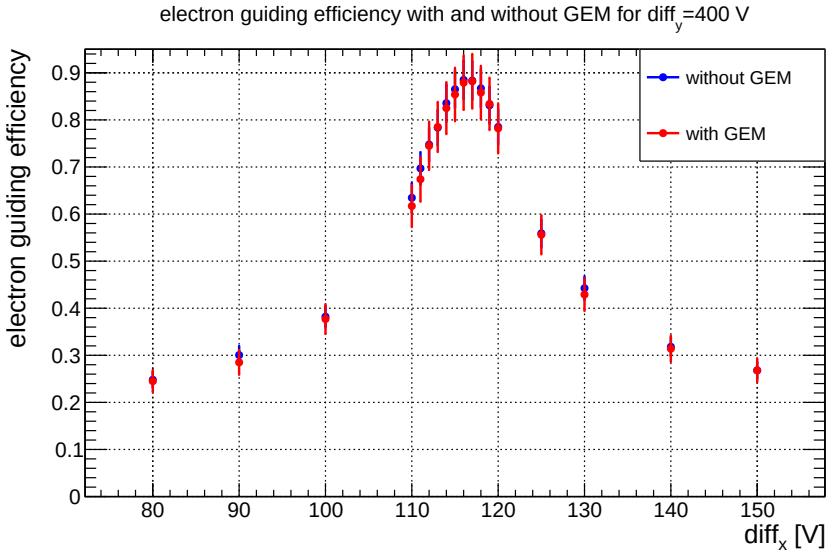

Figure 5.32: The electron guiding efficiency is plotted for the geometries with (red dots) and without (blue dots) GEM foil.

Now the simulation results for geometry 2 (without GEM) and geometry 3 (with GEM) are compared. For the electron guiding efficiency, both geometries show the same peak shape within the limits of simulation accuracy (see figure 5.32). Consequently, the GEM foil does not influence the electron guiding.

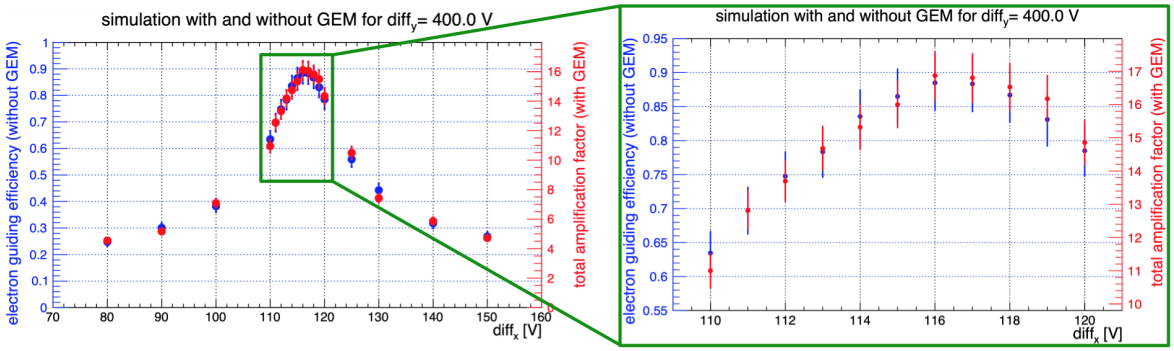

Figure 5.33: In order to compare the electron guiding efficiency from figure 5.32 (without GEM, blue) with the total amplification factor (with GEM, red) both values are overlayed using two differently scaled y-axes. While on the left side both total peaks can be seen, on the right side a zoom on the peak is shown.

Nevertheless, geometry 3 is characterized by the GEM foil. That is the reason why the electron guiding efficiency (without GEM) is compared to the total amplification factor (with GEM) in figure 5.33. Therefore, two different axes (on the left and right of each data set) with the correct scaling are used. While on the left figure all investigated $diff_x$ values are shown, the right one focuses on the peak. Within the limits of accuracy, the peak shapes for the geometries with and without GEM foil are very similar. While

the maximum electron guiding efficiency of about 88 % (without GEM) is reached for $diff_x = 117\,V$, the maximum total amplification factor of 16.1 (with GEM) is achieved for $diff_x = 116\,V$. Both optimized $diff_x$ values lie very close together.

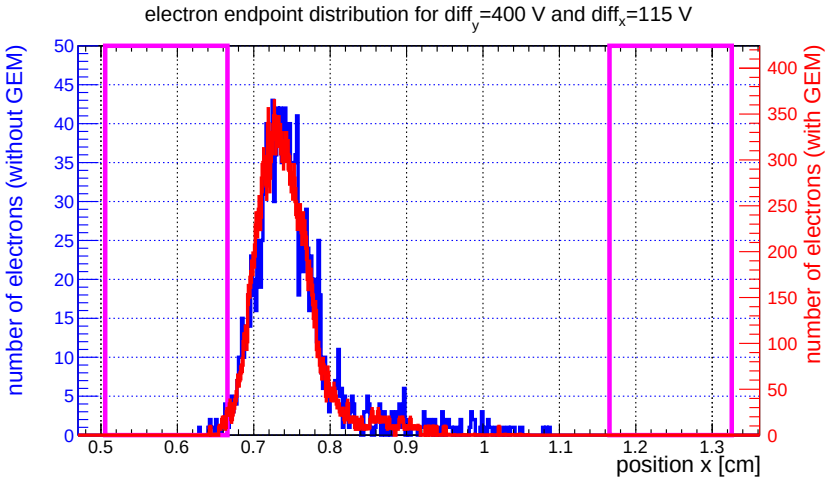

Figure 5.34: The electron endpoint distribution peak below the lamellar area is shown for the two geometries with and without GEM foil. As before the left axis represents the simulation results for geometry 2 (blue) and the scaled right axis the ones for geometry 3 (red). The pink boxes represent the boundaries of the lamellae.

Finally, also the electron endpoint distribution for both geometries is compared. This is done exemplarily for the voltage pair $diff_y = 400\,V$ and $diff_x = 115\,V$ in figure 5.34. For both geometries the electron distribution is very similar.

To sum up, the GEM foil neither influences the electron guiding efficiency nor the electron endpoint distribution up to a scaling factor which represents the gas gain factor.

Additional simulations performed with the GEM foil are presented in Appendix C.

5.2.3.4 Conclusion

With the first structured cathode (geometry 1) the following relations are determined: With higher $diff_y$ the electron guiding efficiency peak gets broader while the maximum guiding efficiency stays constant (see figure 5.17). Furthermore, there is a linear correlation between $diff_y$ and $diff_x$ (compare figure 5.19). All these behaviors result from the guiding angle θ. Changing the lamella geometry and adding gas volumes (geometry 2) influences the guiding efficiency (see figure 5.22). Consequently, geometry 1 is no longer used because geometry 2 is closer to reality. But adding a GEM foil to geometry 2 (leading to geometry 3) does neither show any impact on the guiding efficiency (see figure 5.32 or 5.33) nor on the electron endpoint distribution (see figure 5.34) apart from the constant amplification factor. Since the simulation time for geometry 3 is much longer than for geometry 2 and it does not show other advantages, geometry 2 is favored. That is the reason why geometry 2 is used for further simulations.

5.2.4 Results of Electron Guiding for Final Geometry

Up to now the simulation results base on the detector setup from figure 5.7. Since this real detector setup is iterated until the final setup is achieved, also the simulation has to be adapted. To show the influence of the different properties, the different parameters are changed step by step. As emphasized in the previous section geometry 2 is used for the adaption process. In total five setups of geometry 2 with different parameters are simulated which are presented in table 5.1. The results of the electron guiding efficiency are shown in figure 5.35.

setup	lamella	thickness [mm]	distance g [mm]	strips	voltages
1	2	0.8	5.0	50	inner
2	2	**1.5**	5.0	**25**	inner
3	2	1.5	5.0	25	**all**
4	**5**	1.5	5.0	25	all
5	5	1.5	**7.6**	25	all

Table 5.1: In total five different setups are designed which are step by step adapted from the first detector geometry on figure 5.7 (setup 1 which corresponds to geometry 2) to the final simulation geometry (setup 5). The changed parameters are indicated in bold. For all setups the electron guiding efficiency is simulated (see figure 5.35).

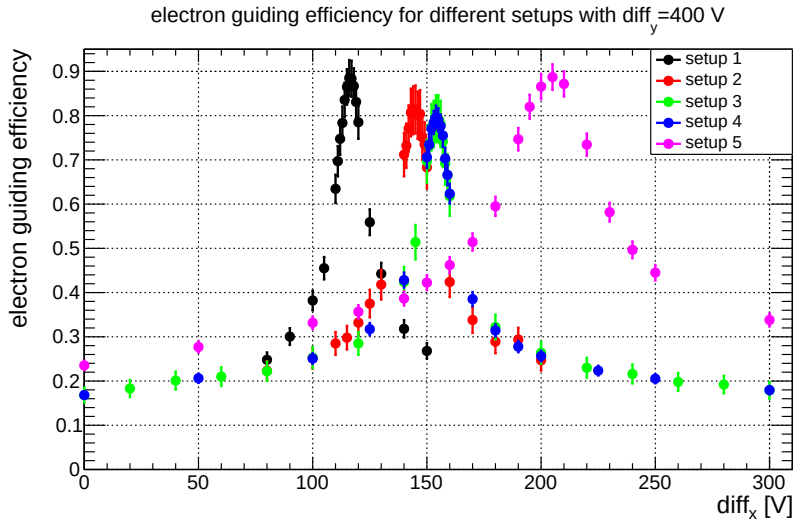

Figure 5.35: For all five setups from table 5.1 the electron guiding efficiency is investigated. While the number of used lamellae does not influence the guiding efficiency (compare setup 3 and 4), all other parameter changes lead to a peak shift.

Setup 1 has still the same parameters as the original geometry 2 from the previous section and the simulations are carried out the same way as described in section 5.2.2. Then the lamella geometry is changed leading to new dielectric boundary conditions. In setup 2 one lamella has a thickness of 1.5 mm and consists of 25 copper strips with a width of 0.4 mm and periodicity of 0.8 mm. This leads to a peak shift from $diff_x = 117\,\mathrm{V}$ to $diff_x = 145\,\mathrm{V}$. Additionally, the maximum efficiency is reduced by about 5 %. A further peak shift to $diff_x = 154\,\mathrm{V}$ is observed (setup 3) if to all copper strips a voltage is applied and not only to the inner ones (see figure 5.10). For setup 4 further lamellae are added resulting in a total number of five lamellae in the detector. This change does

not influence the simulation result within the limits of accuracy. Finally, the distance is increased from 5 mm to 7.6 mm (setup 5) leading to a peak shift to $diff_x = 205\,\mathrm{V}$.

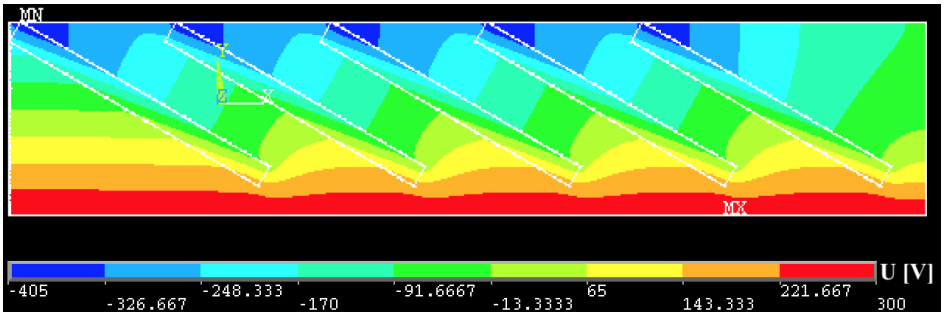

Figure 5.36: The potential distribution for setup 5 using $diff_y = 400\,\mathrm{V}$, $diff_x = 205\,\mathrm{V}$ and $\Delta U_{\mathrm{drift}} = 100\,\mathrm{V}$. Each lamella has a height of $h = 19.6\,\mathrm{mm}$ and tilting angle of $\alpha = 60°$.

Successive improvements are made for the geometry and setup in the simulation to predict the optimal parameter for operation in reality. For the last setup the potential distribution for $diff_y = 400\,\mathrm{V}$ and $diff_x = 205\,\mathrm{V}$ is shown in figure 5.36 giving an impression of the simulation geometry. This final simulation geometry is used for the following simulations. First, for better comparison a peak height factor is defined as:

$$\text{peak height factor} = \frac{\text{maximum guiding efficiency}}{\text{guiding efficiency at } diff_x{=}0\,\mathrm{V}} \tag{5.8}$$

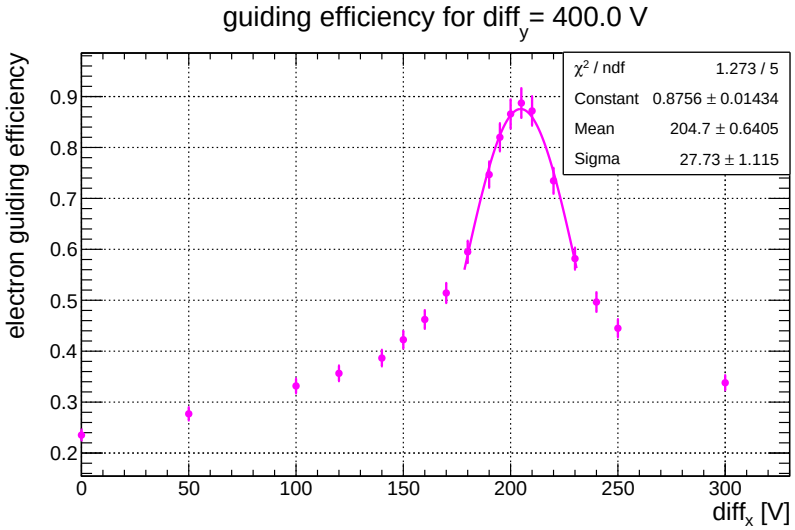

Figure 5.37: The guiding efficiency peak of setup 5 has a peak height factor of 3.77 and the Gaussian fit leads to $\sigma = (27.7 \pm 1.2)\,\mathrm{V}$.

The electron guiding efficiency peak for setup 5 is plotted in figure 5.37 supplemented by a Gaussian fit. For $diff_x = 205\,\mathrm{V}$ the maximum efficiency of about 87 % is reached. Applying equation 5.8 leads to a peak height factor = 3.77. There are electrons which start close to the bottom of the right lamella and as shown in figure 5.28 these electrons can easily be extracted for $diff_x = 0\,\mathrm{V}$ mostly due to the voltage difference $\Delta U_{\mathrm{drift}}$. Additionally, the Gaussian fit parameter provides $\sigma = (27.7 \pm 1.2)\,\mathrm{V}$ which indicates the width of the peak.

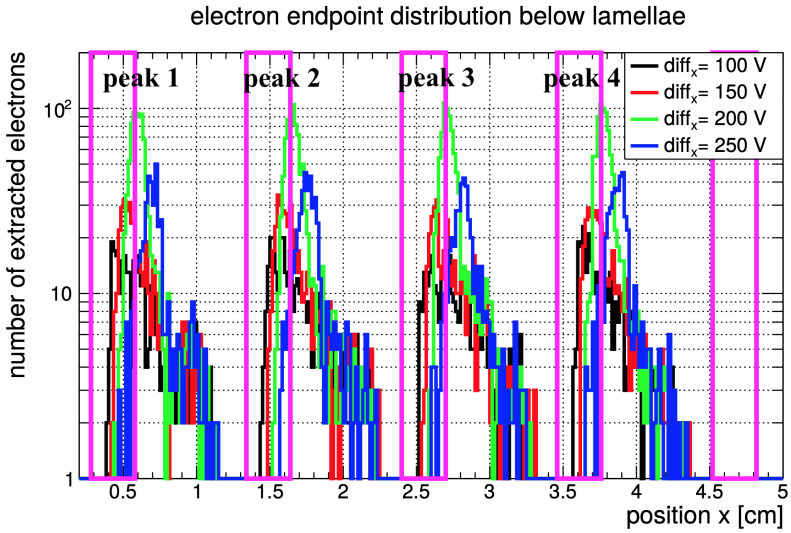

Figure 5.38: Although the electron distribution below the lamellae is now simulated for the new geometry (setup 5, see figure 5.36), the observations are the same: The peaks are located closer to the left lamella and are shifted to the right for increasing $diff_x$.

Figure 5.38 shows the simulated electron endpoint distribution for $diff_y = 400\,V$ and different $diff_x$ values using the new geometry (setup 5, see figure 5.36). Due to the four lamellae gaps also four peaks are observed (peak 1 to peak 4). Despite the changed geometry, the electron distribution still shows the same behavior as observed in figure 5.27. All peaks are located closer to the left lamella and with increasing $diff_x$ the peak is shifted to the right. The peak height is an index for the electron guiding efficiency. These simulation results are used for comparison with measurement results for the Fe-55 measurement (see section 5.3.2) with which the electron guiding is measured.

5.2.5 Photon Conversion Simulated with Geant4

In the simulation not only the electron guiding but also the photon conversion is investigated. Therefore, the interaction process for 50 keV photons with the structured cathode has to be included using Geant4 (see section 4.1) since the used particle source for measurements emits photons in this energy range.

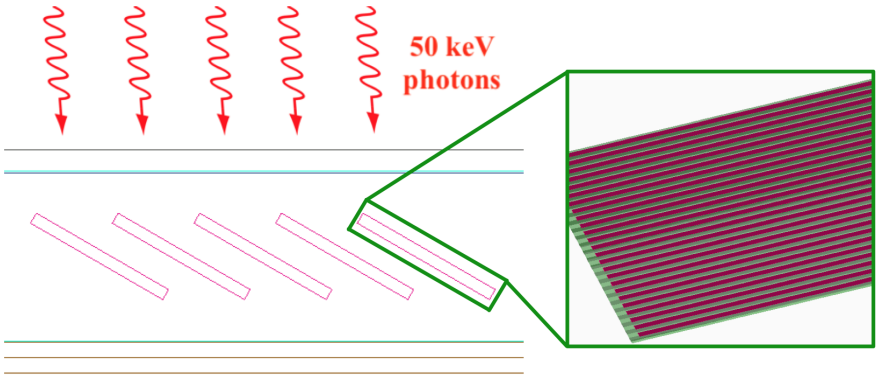

Figure 5.39: In Geant4 the complete structured cathode is built including the lamellae with copper strips (right figure). Then it is irradiated with 50 keV photons.

First the whole structured cathode geometry (geometry 2, setup 5, see previous section) is modeled in Geant4 including the lamellae as shown in figure 5.39. This whole

setup is irradiated with 50 keV photons and the corresponding interaction processes are simulated. In the end, Geant4 provides the position (x, y, z) of the created electrons. It is assumed, that these electrons have zero kinetic energy since the secondary ionization electrons are simulated in Geant4. The photons can interact via the photoelectric effect in the detector gas (Ar), the copper strips or the PCB of the lamella creating primary and secondary ionization. If the electrons can leave the solids, they are located in the gas volume between both lamellae. The position of these electrons in the gaseous environment is taken as start point for the electron drift.

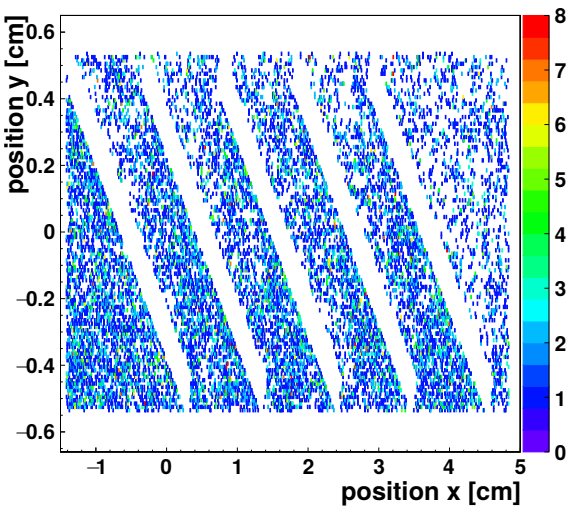

Figure 5.40: The position of initial electrons is simulated with Geant4 for the lamellar area as well as the outside gas volumes at the left and right.

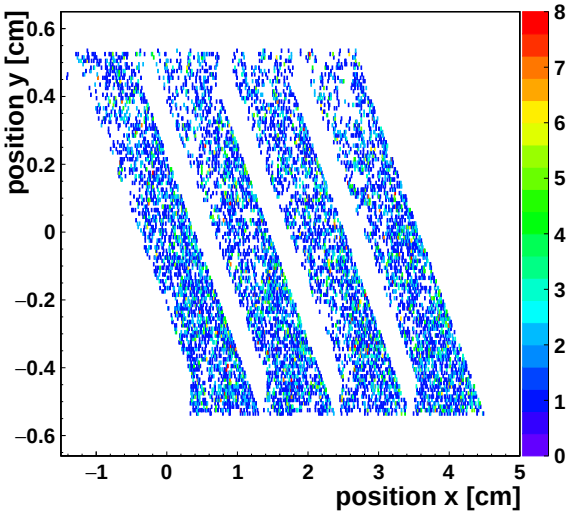

Figure 5.41: Here the simulated position of the initial electrons in the lamellar area is shown.

These electron positions are then imported to Garfield++ as well as the electric guiding field calculated with ANSYS (see figure 5.36). The position distribution of the initial electrons in the lamellar area is shown in figure 5.41. If the electrons which are created outside the lamellar area are taken into account, the position distribution of the initial electrons is defined by figure 5.40. For the simulation this extended area is called complete area and has a width of about 6.2 cm. As in section 5.2.2 the electrons are counted as extracted if they pass the position $y = -0.6$ cm. With this simulation the combination of photon conversion and electron guiding can be investigated.

5.2.6 Results of Combined Photon Conversion and Electron Guiding

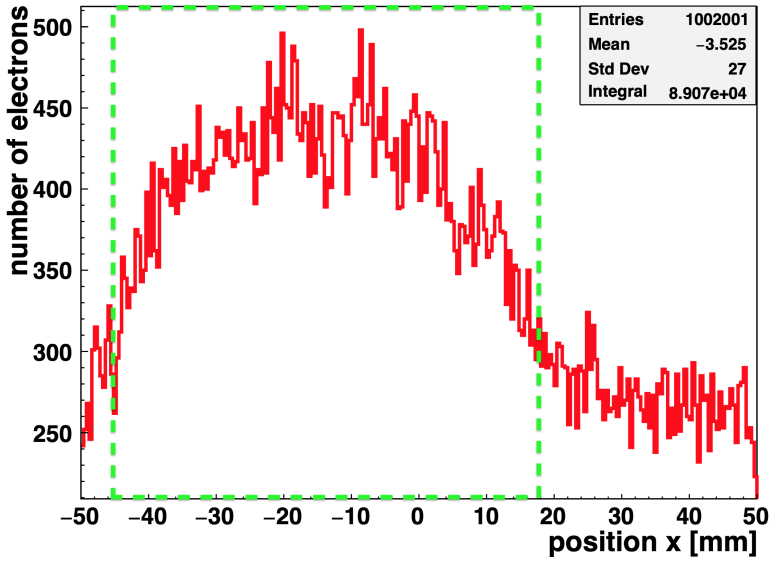

Figure 5.42: In Geant4 the number of created electrons in the photon conversion process is counted. The green rectangle marks the lamellar area where more electrons are created than in the area where no lamellae are placed.

First, the result of the photon conversion process simulated in Geant4 is shown in figure 5.42. For about $x > 18\,\text{mm}$ the active detector area is empty and surrounded by gas while in the lamellar area the structured cathode is positioned (compare figure 5.48 and figure 5.50). Therefore, the number of created electrons in the surrounding gas volume is counted which is about 1.6 times smaller in the lamellar area. According to this simulation the photon conversion efficiency is increased by the use of this structured cathode geometry by a factor of 1.6, partially due to the copper strips. The electrons have to be guided outside the lamellar area which is achieved by the electric field E_{res} as in all previous simulations.

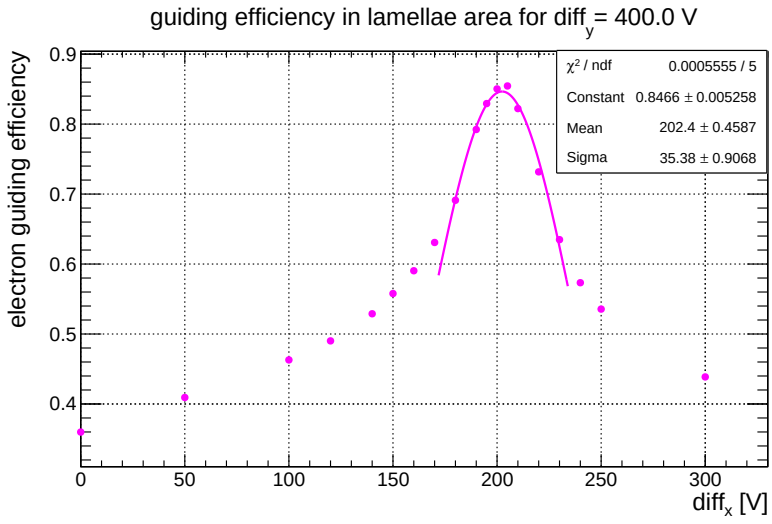

Figure 5.43: The simulated electron guiding efficiency show a peak for $diff_y = 400\,\text{V}$ with a peak height factor of 2.37 and width of $(35.4 \pm 1.0)\,\text{V}$.

The simulated electron guiding efficiency for $diff_y = 400\,\mathrm{V}$ and different $diff_x$ is presented in figure 5.43. As expected, an efficiency peak is observed with a peak height factor of 2.37 (see equation 5.8) and a width of $\sigma = (35.4 \pm 1.0)\,\mathrm{V}$. As in the simulation performed in section 5.2.4 the maximum efficiency is achieved for $diff_x = 205\,\mathrm{V}$. This efficiency peak results from the electrons created in the lamellar area (see figure 5.41). Now it is compared to the electrons positioned in the complete area (see figure 5.40). In the simulation this complete area has a width of about 6.2 cm.

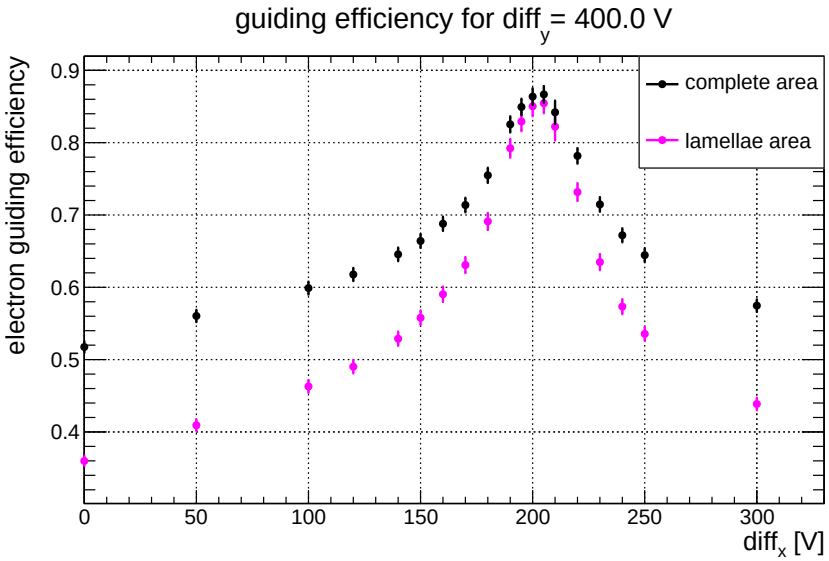

Figure 5.44: The electron guiding efficiency peak for the electrons created in the complete area (black dots) (6.2 cm in figure 5.40) is higher compared to those created in the four areas in between the lamellae (pink dots). The difference between both efficiency plots depends on $diff_x$.

This comparison is shown in figure 5.44. For both areas the peak height factor differs. While the peak height factor for the lamellar area is 2.37, it is smaller for the complete area with 1.68 due to the additional electrons in the gas volume at the left and right of the outer lamellae. Most of these electrons can directly be extracted since there are no obstacles in their drift direction. The total number of these electrons is independent of the applied voltage $diff_x$ and stays nearly constant since $diff_y$ is fixed for the simulation. Nevertheless, the relative weight of these electrons is larger for $diff_x$ values where only a few electrons are extracted from the lamellae area like for $diff_x = 0\,\mathrm{V}$ or $diff_x = 300\,\mathrm{V}$. As a consequence for these $diff_x$ values the relative amount of extracted electrons from the outside gas volumes dominates which leads to a significant higher efficiency for the complete area. This is due to counting all extracted electrons without spatially resolving their origin. The difference between both curves gets smaller for $diff_x$ values with high extraction probability because then the relative amount of extracted electrons from the lamellar area dominates. Nevertheless, due to the additional electrons the guiding efficiency for the complete area is always higher than for the lamellar area.

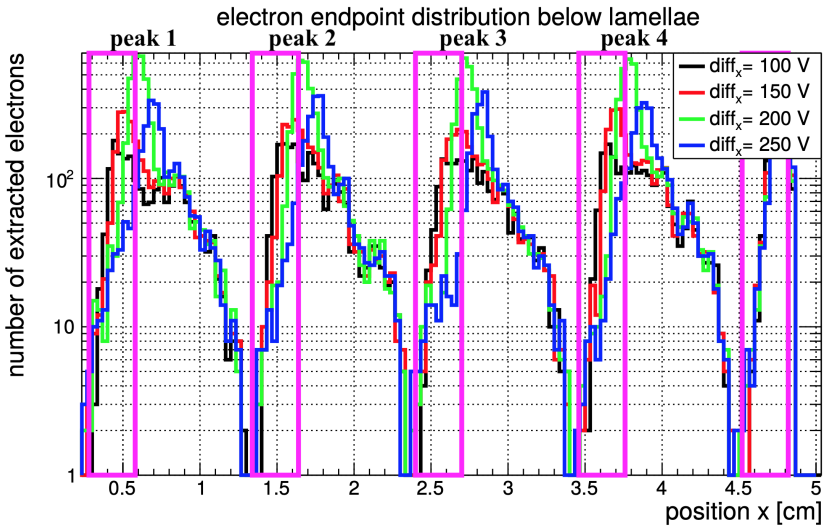

Figure 5.45: The position and height of the electron distribution peaks below the lamellar area depend on the applied voltage $diff_x$. The pink boxes mark the lamella boundaries.

As shown in figure 5.45 the electron distribution below the lamellar area for $diff_y = 400\,V$ is influenced by $diff_x$. In general, all peaks are positioned close to the left lamella due to the same reason explained in section 5.2.3.2. But with increasing $diff_x$ the distribution peaks are shifted to the right. Since the peak height is an index for the electron guiding efficiency, it increases up to the value $diff_x = 200\,V$ and then decreases according to figure 5.43.

These simulation results are used for comparison with measurement results for the Am-241 measurement (see section 5.3.3) During these measurements the combination of photon conversion and electron guiding is examined and the performance of the structured cathode is investigated.

5.3 Measurements

For the measurements a structured cathode is placed inside a GEM detector (see section 3.1). Two different measurement setups are used one with a Fe-55 source (5.9 keV photons) to investigate the electron guiding and the other with an Am-241 source. Americium produces 59.9 keV photons which are used to examine the photon conversion in combination with the electron guiding. The results are then compared to the corresponding simulations.

5.3.1 Setup

The first structured cathode prototype is introduced in figure 5.7 and is used as starting point for the simulation geometry. Nevertheless, with this construction no measurement could be performed due to various difficulties. Building on the gained knowledge from simulation and interim measurements, the structured cathode as well as parts of the detector setup are further improved leading to a setup which is used for measurements.

5.3.1.1 Difficulties

First, a new larger detector housing (see Appendix D) is designed since the necessary voltages cannot be applied because sparks between the structured cathode or its cables and the housing occur. Additionally, the first designed lamellae are too fragile. They are quite thin and their strips have a small width, consequently the connection strip to the pads broke easily and no voltage could be applied. This makes most of the lamellae unusable. For a more stable lamella design the thickness is increased from 0.8 mm to 1.5 mm. Each strip is still 35 µm thick but the width is changed from 0.2 mm to 0.4 mm and the periodicity from 0.4 mm to 0.8 mm leading to 25 strips in total on each side and a lamella height of 19.6 mm. Additionally, the electron guiding is influenced by electric field irregularities which have their origin in the printed resistors and the positioning of the lamellae inside the detector.

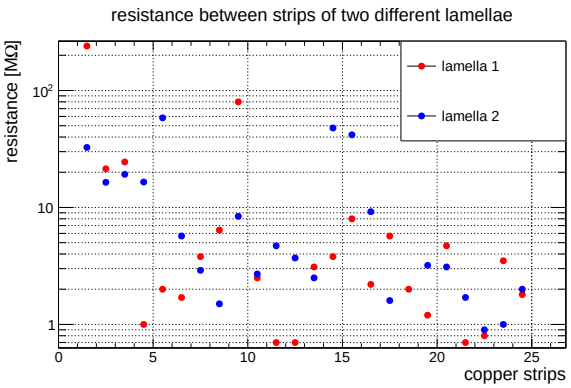

Figure 5.46: The resistance between adjacent copper strips can differ largely, as seen for two lamellae exemplarily.

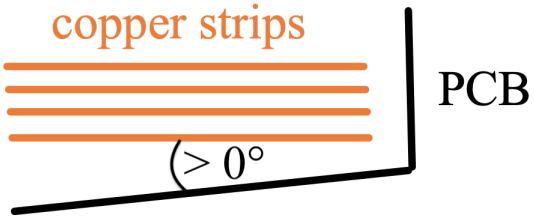

Figure 5.47: The distance between PCB edge and copper strips can be inhomogeneous (exaggerated drawing).

The use of a printed resistor (see Appendix A) leads to resistance values which lie between 100 MΩ and 800 MΩ. Consequently, each lamella side shows a different voltage gradient that influences the electric field. Additionally, the resistance between two adjacent strips is unequal. This is shown exemplarily for two lamella sides in figure 5.46 where the resistances between two strips vary between less than 1 MΩ and 240 MΩ.

Another difficulty is the positioning of the lamellae. It is necessary to cut the PCB edge to the proper width. This is done with a guillotine cutter. Unfortunately, the precision of this technique is not as good as desired leading to an inhomogeneous distance between the outer copper strip and the lamella edge. This is drawn exaggeratedly in figure 5.47. If these lamellae are then fixed inside the mount, their orientation is defined by the PBC edge and consequently the copper strips are not aligned parallel to the copper strips of the adjacent lamellae. Both aspects, the printed resistor and the lamella positioning, result in electric field irregularities effecting the electron guiding.

5.3.1.2 Final Setup

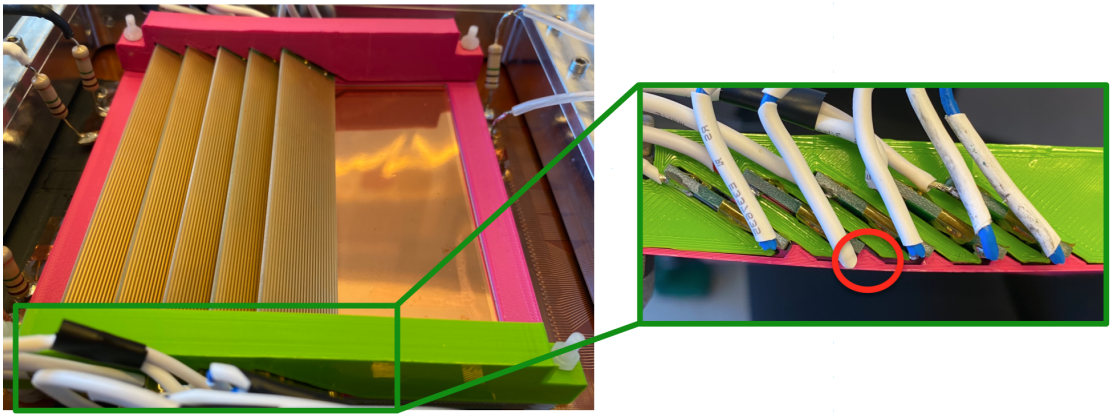

Figure 5.48: The opened GEM detector is shown in this figure. Five lamellae (see figure 5.49) are placed in the active gas volume (Ar:CO_2) of the detector with a distance $g = 7.6\,\text{mm}$ and tilting angle $\alpha = 60°$ with the large housing (left side). For a better fixation of the lamellae little triangles are integrated (red circle on the right) into the pink holding structure. In figure 5.50 this detector is closed.

The final detector setup is shown in figure 5.48. In order to fix the lamella difficulties introduced in the previous section an improved lamella design is used which is shown in figure 5.49.

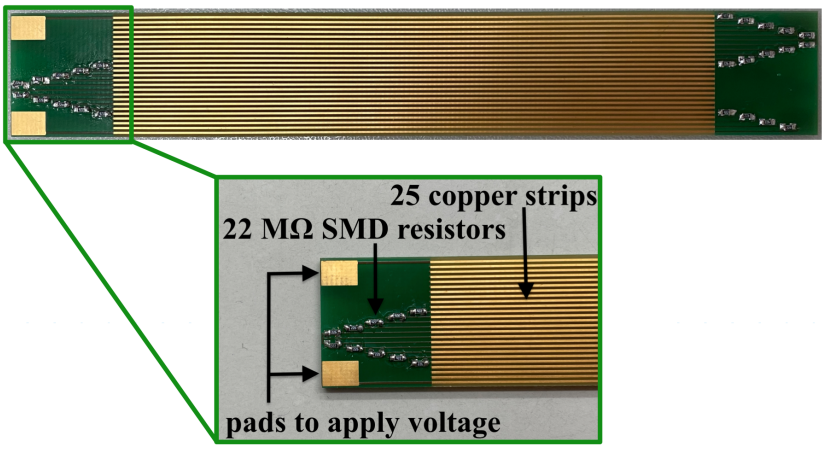

Figure 5.49: A lamella to solve the difficulties from figure 5.46 and 5.47 is designed. The distance between outer copper strip and PCB edge is now exact due to the improved production process. By replacing the printed resistor through single 22 MΩ SMD resistors now the resistance between two strips is well defined.

With this lamella design both difficulties can be solved. Due to a different production process the distance between the PCB edge and the outer copper strip is already well defined. Furthermore, the printed resistor is replaced by single 22 MΩ SMD resistors between two strips leading to a total resistance of 528 MΩ per lamella side. Despite the tolerance which is smaller than 1 % the resistance for each lamella and all adjacent strips is equal now. Apart from these changes the dimensions of the lamella, especially the PCB and copper strips, are the same as before. Five of these lamellae are placed inside a GEM detector with a distance $g = 7.6\,\text{mm}$ and tilting angle $\alpha = 60°$ as shown in figure 5.48 and the used mount is presented in Appendix E. This final geometry and the simulated geometry (see section 5.2.4 and 5.2.6) have the same parameters and are used for comparison.

GEM1B	GEM1T	GEM2B	GEM2T	GEM3B	GEM3T
−400 V	−700 V	−1050 V	−1350 V	−1650 V	−1950 V

Table 5.2: To provide amplification these voltages are applied at the GEM foils. The naming corresponds to figure 3.3 and the ending 'B' stands for the bottom and 'T' for the top side of a GEM foil.

To guide an electron from the structured cathode to the readout area, the structured cathode as well as all GEM foils need a proper high voltage supply. The used voltages for the GEM foil are presented in table 5.2 where the ending 'B' stands for the bottom side of one GEM foil and 'T' for the top side. Now this optimized detector setup, including the structured cathode, is flushed with a gas mixture of 93:7 vol. % Ar:CO_2 and connected to the readout electronics (see section 3.2). This final setup is then ready for measurements. While for the first measurement (see section 5.3.1.3) the data acquisition program mmdaq is used for data recording, for the second one (see section 5.3.1.4) the method described in [17] is taken (see section 3.3).

5.3.1.3 Fe-55 particle source

In order to perform first test regarding the electron guiding efficiency, 5.9 keV photons emitted by an ^{55}Fe-source enter the structured cathode parallel to the lamellae to partially achieve a homogeneous electron distribution between two lamellae.

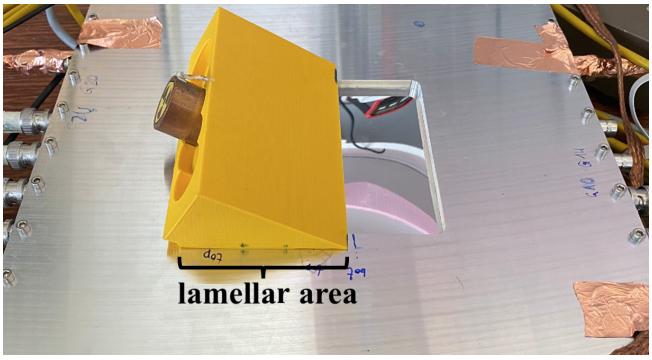

Figure 5.50: The ^{55}Fe-source is positioned under a tilting angle of 60° above the lamellar area. Furthermore, the Aluminum coated Kapton-window, the high voltage connections and the housing are shown.

Therefore, a radioactive Iron-55 source is used. ^{55}Fe decays by electron capture to ^{55}Mn

$$^{55}_{26}\mathrm{Fe} + {}^{0}_{-1}\mathrm{e} \longrightarrow {}^{55}_{25}\mathrm{Mn} + \gamma(5.9\,\mathrm{keV})$$

emitting a mono-energetic photon with an energy of 5.9 keV. If this photon interacts with one lamella or other materials, it is absorbed by the photoelectric effect. This is the reason why the source has to be positioned with an inclination angle of 60° which corresponds to the angle of the lamellae as shown in figure 5.50. Since the orientation of the detector is still the same as in figure 5.48, the source is located above the lamellar area. The created electrons are then guided to the amplification and readout area. Consequently, with this detector setup and source configuration the electron guiding is investigated.

5.3.1.4 Am-241 particle source

The final application of this structured cathode is to increase the conversion efficiency for photons with energies of about 50 keV which leads to a higher electron creation in the copper of the lamella or in the lamella itself. This is investigated with the following setup.

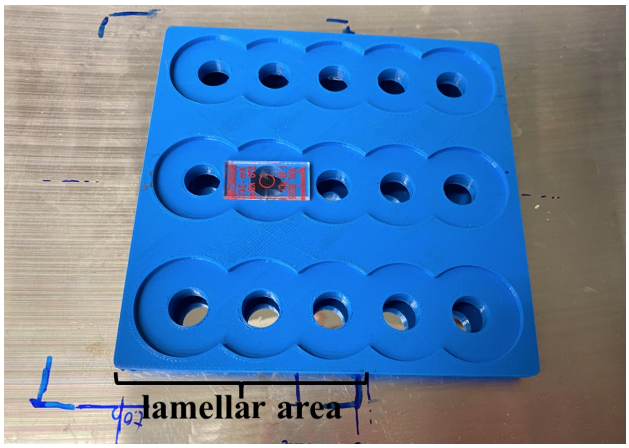

Figure 5.51: The ^{241}Am-source is positioned above the lamellar area. The blue mount covers the complete Kapton-window.

In order to investigate the photon conversion and the electron guiding an Americium-241 source is used. Therefore, the alpha decay of ^{241}Am to ^{237}Np

$$^{241}_{95}\mathrm{Am} \longrightarrow {}^{237}_{93}\mathrm{Np} + {}^{4}_{2}\alpha \; + \gamma(59.5\,\mathrm{keV})$$

is interesting since a photon with an energy of 59.5 keV is created. As shown in figure 5.51 it is positioned above the lamellar area. Due to the higher photon energy compared to the ^{55}Fe source, they are not absorbed but interact with the lamellae. With this the combination of photon conversion and electron guiding is examined.

5.3.2 Results for Electron Guiding using an Fe-55 Source

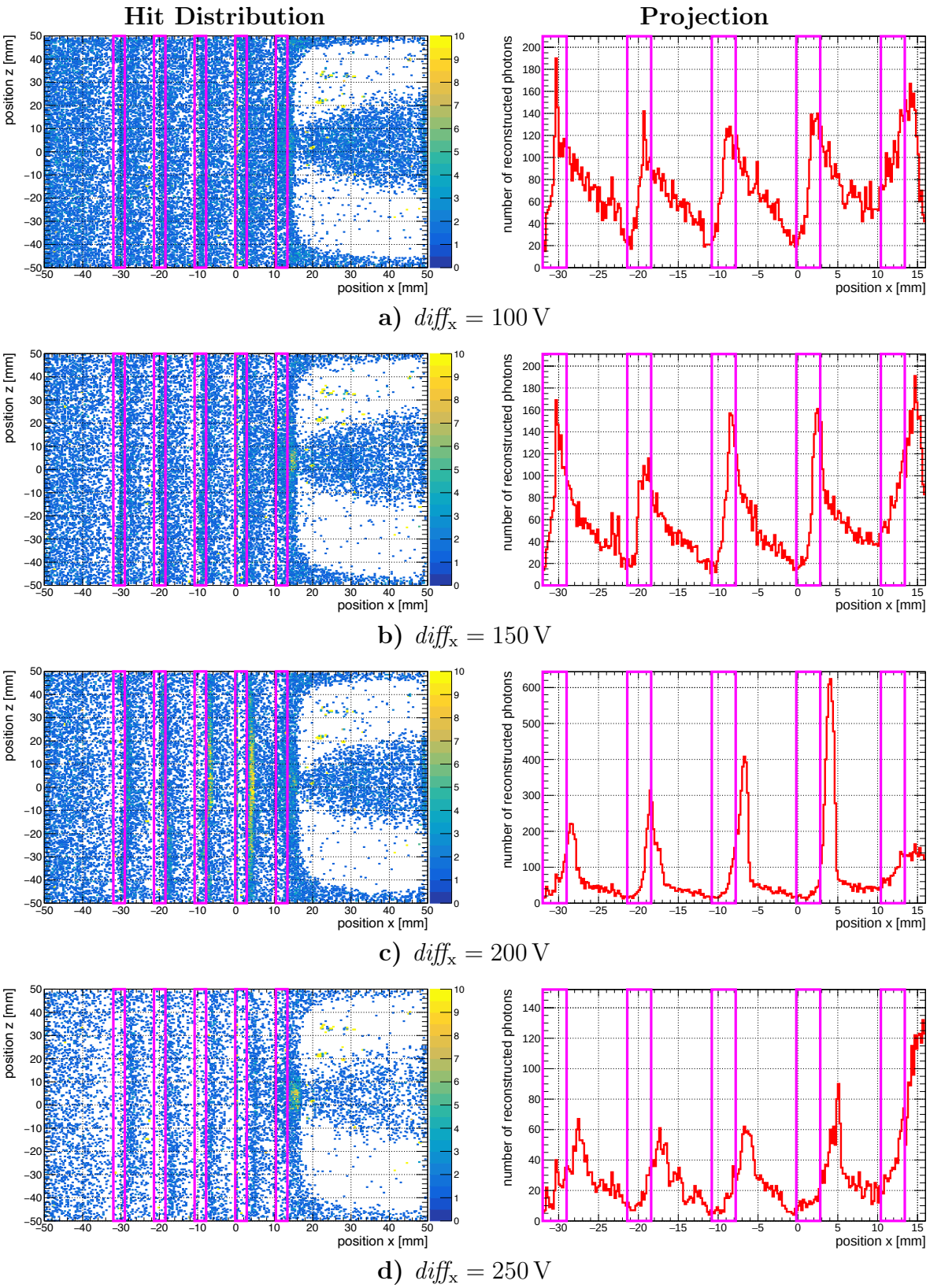

Figure 5.52: On the left side the measured hit distributions for fixed $diff_y = 400\,V$ and different $diff_x$ are presented while on the right side the corresponding projections are shown. The pink boxes mark the lamella boundaries. In the hit distribution more hits are observed close to the lamellae resulting in peaks in the profile. These peaks are located close to the left lamella and are shifted to higher x-positions for increasing $diff_x$.

For investigation of the electron guiding the ^{55}Fe source introduced in section 5.3.1.3 is used. As in all simulations performed so far, a voltage difference between the top side of the third GEM foil and the bottom side of the lamella $\Delta U_{\text{drift}} = 100\,\text{V}$ is applied. Additionally, the voltages from table 5.2 are applied. While $diff_{\text{y}} = 400\,\text{V}$ is fixed, $diff_{\text{x}}$ is varied. The resulting hit distributions are presented in figure 5.52 on the left side for $diff_{\text{x}} = 100\,\text{V}$, $diff_{\text{x}} = 150\,\text{V}$, $diff_{\text{x}} = 200\,\text{V}$ and $diff_{\text{x}} = 250\,\text{V}$. There are more hits closer to the lamellae than in the middle for all of these four $diff_{\text{x}}$ values. The corresponding x-projection of the hit distribution in the lamellar area is shown on the right of figure 5.52 for the same voltages. Although the projections show the same behavior as the hit distributions, this visualization helps by investigating and comparing the measurement results. In all cases the peaks are located closer to the left lamella. Up to $diff_{\text{x}} = 200\,\text{V}$ the peaks get sharper with increasing voltage whereas for $diff_{\text{x}} = 250\,\text{V}$ it is broader again. Also a peak shift to the right with increasing $diff_{\text{x}}$ is observed. While for most of the presented profiles the height of the single peaks is constant, for $diff_{\text{x}} = 200\,\text{V}$ it increases from left to right. The measurement results seem to be influenced by the applied voltage $diff_{\text{x}}$ as expected. Nevertheless, there are also hits outside the lamellar area due to the ^{55}Fe source halo which can be seen in the hit distribution. All these observations are further investigated and compared to the simulation results from section 5.2.4 since the simulated homogeneous electron distribution between the lamellae approximates the position of the created electrons from the interaction process of the 5.9 keV photons with the detector gas.

5.3.2.1 Electron Guiding Peak

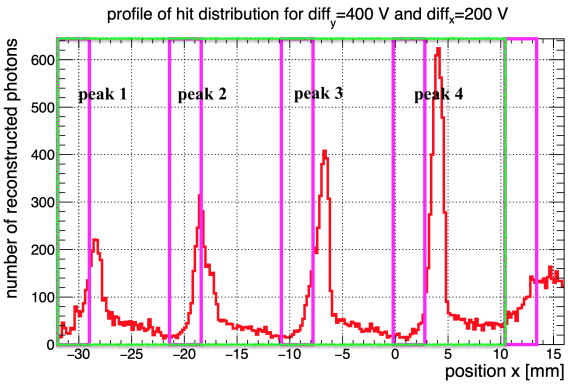

Figure 5.53: In the measurement the number of reconstructed photons in the lamellar area (green rectangle) divided by the measuring time defines the frequency which is a measure for the guiding efficiency.

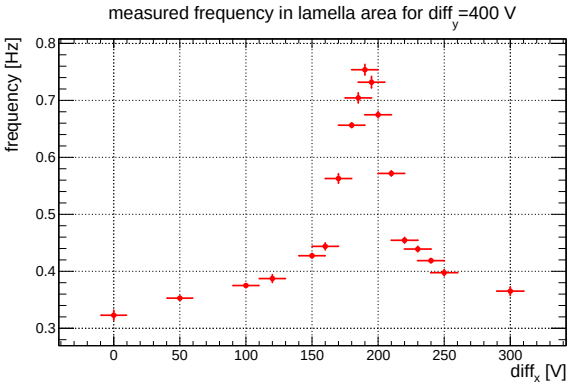

Figure 5.54: A frequency peak is measured. It includes the tolerance of the power supply. The maximum frequency is reached for $diff_{\text{x}} = (190 \pm 10)\,\text{V}$.

Figure 5.53 shows the measured profile of the hit distribution for $diff_{\text{y}} = 400\,\text{V}$ and $diff_{\text{x}} = 200\,\text{V}$. In the measurement the electron guiding efficiency can be associated to the number of reconstructed photons in the structured cathode area divided by the measuring time which defines the frequency in this area. This measured frequency is plotted in figure 5.54 for various $diff_{\text{x}}$ while $diff_{\text{y}} = 400\,\text{V}$ is constant. As expected, a frequency peak including all four peaks is measured with a maximum frequency for $diff_{\text{x}} = (190 \pm 10)\,\text{V}$. The corresponding error bars for $diff_{\text{x}}$ result from the tolerance

of the power supply (see [25]). For better visualization the $diff_x$ error bars are not included in the following histograms.

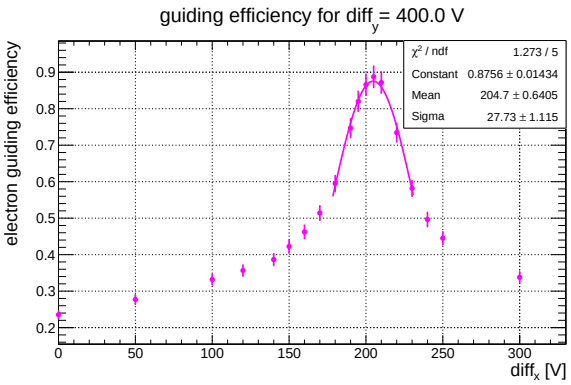

Figure 5.55: The simulated guiding efficiency peak has a peak height factor of 3.77 and width of $\sigma = (27.7 \pm 1.2)\,\mathrm{V}$.

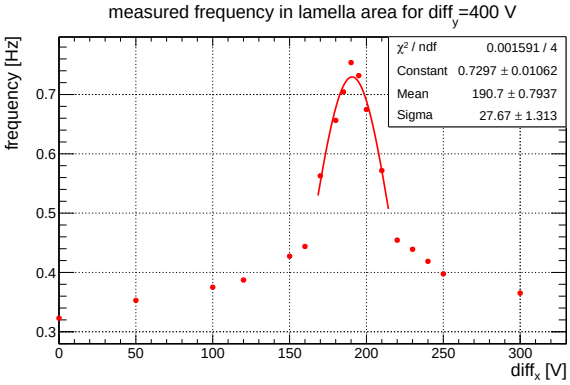

Figure 5.56: The measured frequency peak has a peak height factor of 2.33 and width of $\sigma = (27.7 \pm 1.4)\,\mathrm{V}$.

In figure 5.55 the simulation result of the electron guiding efficiency peak is shown with a peak height factor of 3.77. The fitted Gaussian function provides the width of the peak with $\sigma = (27.7 \pm 1.2)\,\mathrm{V}$. To the measured frequency peak in figure 5.56 a Gaussian function is fitted as well. The resulting width $\sigma = (27.7 \pm 1.4)\,\mathrm{V}$ is identical to the simulated one including the error interval. Additionally, the position of the peak for the simulation ($diff_x = (204.7 \pm 0.7)\,\mathrm{V}$) and the measurement ($diff_x = (190.7 \pm 0.8)\,\mathrm{V}$) lie rather close together. But the peak height factor is with 2.33 about 1.62 times smaller than expected from simulation. Nevertheless, simulation and measurement peaks show similar shapes.

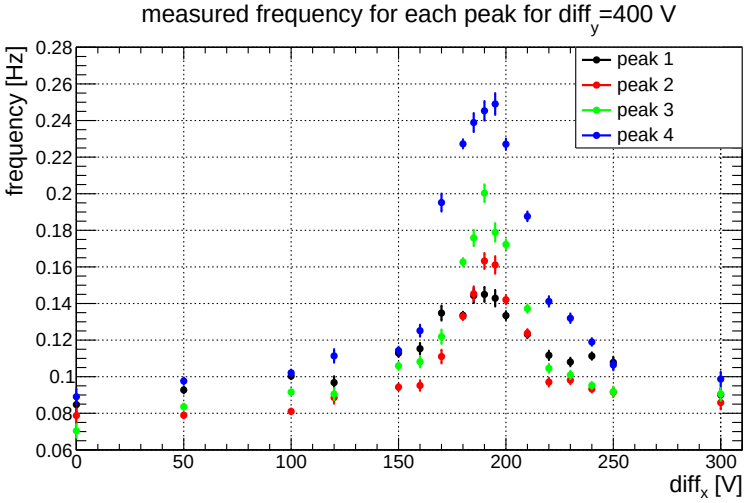

Figure 5.57: The measured frequencies for the single peaks differ. It is about 60 % higher for peak 4 (peak height factor = 2.76) compared to peak 1 (peak height factor = 1.71).

Different peak height factors are observed if the measured frequency is determined for each peak individually. This is shown in figure 5.57 and the labeling of the peaks in figure 5.53. The maximum frequency increases from left (peak 1) to right (peak 4) and the corresponding peak height factor reaches from 1.71 for the first peak to 2.76 for the last one. This determination emphasizes the different behavior of the peaks which can

already be seen in figure 5.53. The reason for this behavior might be the positioning of the source which is further examined in section 5.3.2.3.

5.3.2.2 Electron Distribution

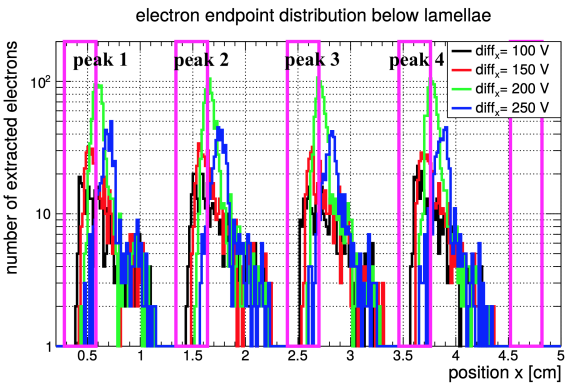

Figure 5.58: In the simulation the peaks are located closer to the left lamella and are shifted to the right with increasing $diff_x$. The peak height is also influenced by $diff_x$.

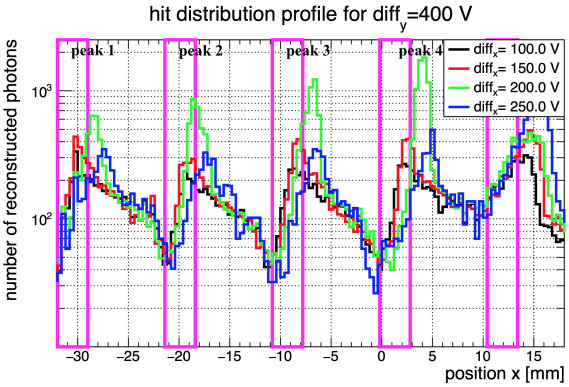

Figure 5.59: Also in the measurement the peaks are located closer to the left lamella and are shifted to the right with increasing $diff_x$. The peak height is also influenced by $diff_x$.

Since the electron distribution below the lamellae can be simulated and measured, it is another useful quantity for comparison. Figure 5.58 shows the simulated electron endpoint distribution for $diff_y = 400\,V$ and different $diff_x$ (see section 5.2.4). The measurement result for the same voltage values is presented in figure 5.59. Simulation and measurement show a similar behavior. All peaks are located closer to the left lamella and with increasing $diff_x$ they are shifted to the right. Since every measured distribution is scaled to the corresponding measuring time, the peak height represents the measured frequency while for the simulation it is an index for the electron guiding efficiency. According to section 5.3.2.1 the peak height is the highest for the four plotted $diff_x$ values for $diff_x = 200\,V$. Although simulation and measurement show a rather good agreement, for a better comparison the peak shift has to be quantified.

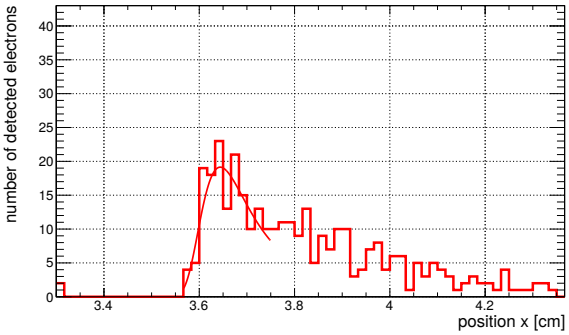

Figure 5.60: Fit of a Landau function to peak 4 of the simulated electron distribution.

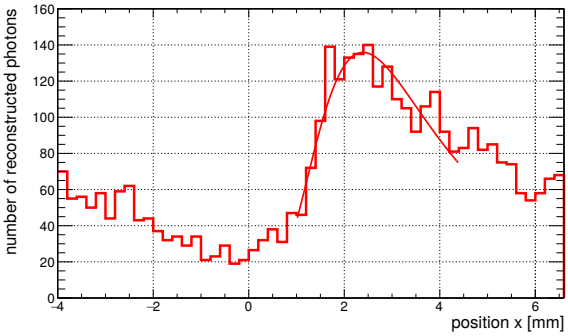

Figure 5.61: Fit of a Landau function to peak 4 of the measured electron distribution.

Therefore, to every peak of the electron distribution a Landau function is fit in order to describe the shape. This is exemplarily shown in figure 5.60 for the simulation and

in 5.61 for the measurement. In figure 5.61 for $x < 0\,\text{mm}$ an overlap of background noise and the tail from peak 3 can be observed. The fit does not aim for a perfect description of the complete peak shape but should provide the x-position of each peak as precisely as possible. It is received from the fit parameter for the most probable value. Due to a quite flat electron distribution for $diff_\text{x} = 0\,\text{V}$ and $diff_\text{x} = 50\,\text{V}$ the first considered value is $diff_\text{x} = 100\,\text{V}$ which marks the starting point. The peak shift is then defined as the x-distance between another $diff_\text{x}$ value and $diff_\text{x} = 100\,\text{V}$

$$\text{peak shift} = x(diff_\text{x}) - x(diff_\text{x} = 100\,\text{V}) \tag{5.9}$$

with $diff_\text{x} > 100\,\text{V}$.

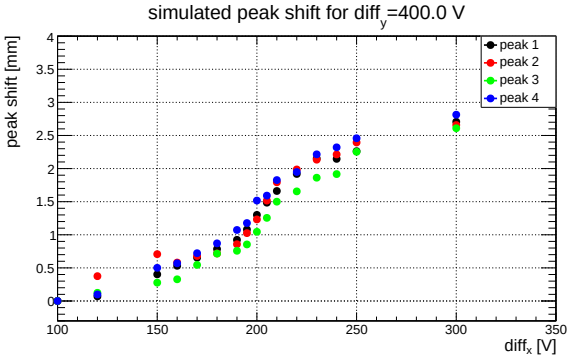

Figure 5.62: The simulated peak shift has an s-shape with the largest peak shift in the range of the highest electron guiding efficiency at the turning point. While peak 4 tends to have the largest shift, peak 3 has the smallest one. The fitting errors are included but they are too small to be noticeable.

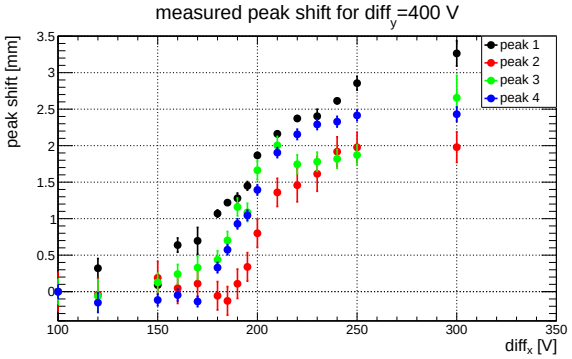

Figure 5.63: The measured peak shift shows an s-shape as expected from simulation. Here peak 1 shows the largest shift while peak 2 tends to have the smallest one.

This peak shift is calculated for all four peaks separately. The results are shown for the simulation in figure 5.62 and for the measurement in figure 5.63. In both cases the development of the peak shift is very similar. With increasing $diff_\text{x}$ first a slight peak shift occurs which becomes larger in the range of the highest guiding efficiency between $diff_\text{x} = 190\,\text{V}$ and $diff_\text{x} = 210\,\text{V}$. For even higher $diff_\text{x}$ values the shift starts to saturate. Although this behavior is valid for all peaks, each of them shows a slightly different shift. In the simulation peak 4 has the highest shift while peak 3 has the smallest whereas in the measurement peak 1 has the highest and peak 2 the smallest shift. In general, differences in the shift between the single peaks can occur due to the fitting method. The reason for discrepancies in the measurement can be the alignment of the lamellae as well as the position of the source which influence the electron distribution. Nevertheless, simulation and measurement have similar results showing that the structured cathode works as intended.

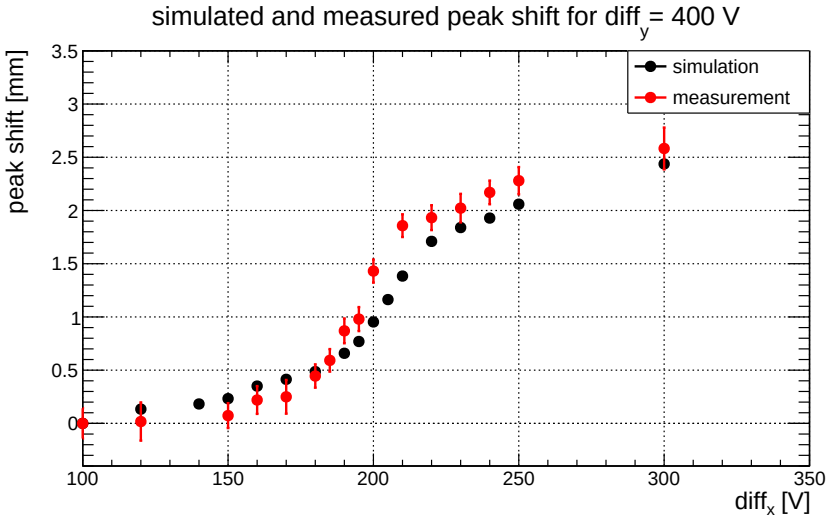

Figure 5.64: Average peak shift versus $diff_x$ at $diff_y = 400\,V$ for simulation (black) and measurement (red).

For a better comparison the average shift for each $diff_x$ is calculated and plotted in figure 5.64. Simulation and measurement show good agreement. Only in the range around the highest electron guiding efficiency (maximum at $diff_x = 205\,V$ see figure 5.55) and the highest measured frequency (maximum at $diff_x = 190\,V$ see figure 5.56) the discrepancy is slightly larger. The reason for this might be the different $diff_x$ values for the maximum guiding efficiency which lead to a general offset between simulation and measurement. Additionally, the $diff_x$ error from figure 5.54 has to be considered. The s-shape of the plotted peak shift can be explained with equation 5.4 since the guiding angle θ defines the direction of the electron drift. Consequently, also the peak position is determined by θ as well as the peak shift for different $diff_x$ values. Considering that θ is described by an inverse tangent function, the resulting peak shift also has this shape. Since the efficiency peaks are symmetric around the maximum efficiency, the peak shift shows a point reflection around the optimized $diff_x$ value. Summarizing, simulation and measurement values lie close together.

5.3.2.3 Differences between Simulation and Measurement

Although simulation and measurement exhibit a general agreement, some differences can be observed which are now further examined. For the measured electron guiding efficiency (see figure 5.57) as well as the measured peak shift (see figure 5.63) the results for the single peaks differ. Figure 5.53 shows nicely how for $diff_y = 400\,V$ and $diff_x = 200\,V$ the peak height increases from left to right. Consequently, the measured frequency increases from left (peak 1) to right (peak 4) which is shown in figure 5.57. The origin of this behavior might be the source position. For this investigation the frequency in the lamellar area is measured for varying source position.

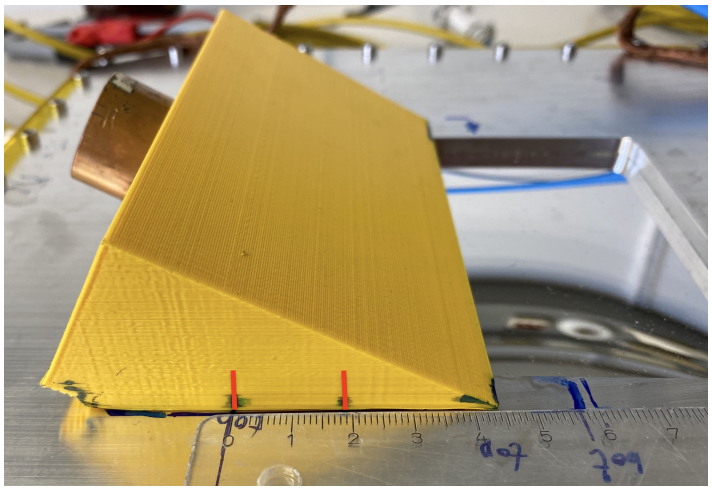

Figure 5.65: The exit area of the photons in the mount is marked with two red lines at the bottom. For a proper alignment the left line is positioned at 0 cm (see ruler) which also represents the edge of the entrance window of the detector.

The mount for the ^{55}Fe source under an angle of 60° is shown in figure 5.65. The two red lines on the bottom of the mount mark the exit area of the photons and are used for alignment. Additionally, with the help of a ruler the position is defined. In total the entrance window is $(10 \times 10)\,\mathrm{cm}^2$ large and starts at the ruler position 0 cm where the left red line from the mount is aligned. For the measurement the source position is changed in 0.5 cm steps.

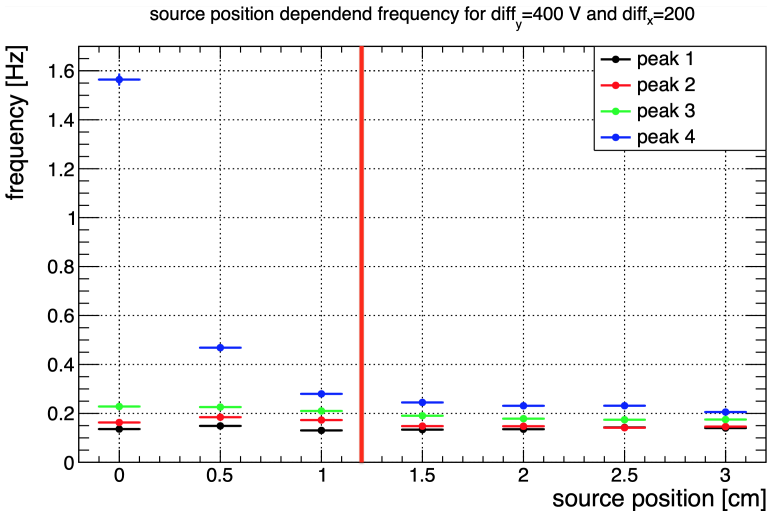

Figure 5.66: The measured frequency for peak 1 and peak 2 stay constant while for peak 3 a slight decrease is observed. Only peak 4 shows a completely different behavior: The frequency drops constantly. All previous measurements were performed at the position 1.2 cm (vertical red line).

The measured frequency is plotted against the source position in the lamellar area for each peak in figure 5.66. While the frequency stays constant for peak 1 and peak 2, it slightly decreases for peak 3. For peak 4 however, the source position has the strongest influence. The frequency drops from 1.6 Hz at 0 cm to about 0.2 Hz at 3 cm. To understand the different behavior at 0 cm the measured hit distributions are further studied.

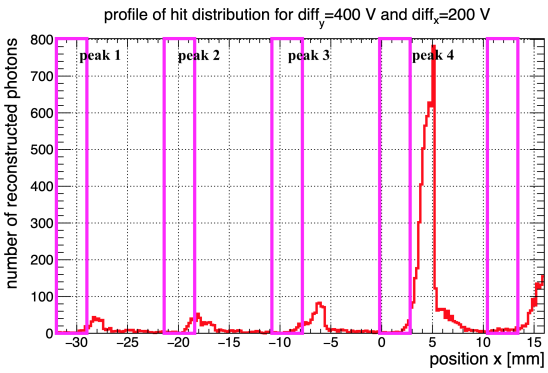

Figure 5.67: At the source position 0 cm peak 4 is up to 10 times higher than the others.

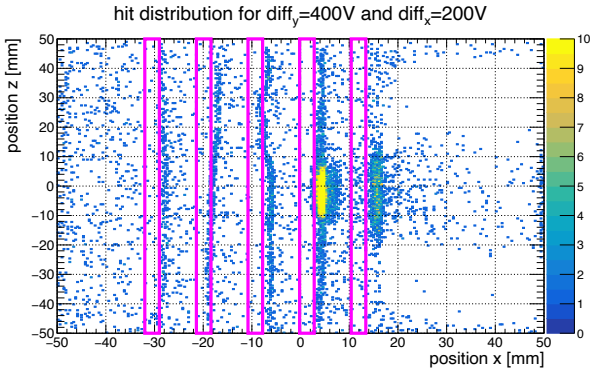

Figure 5.68: At the source position 0 cm for peak 4 an oval formed hit distribution is observed. It is the beam core of the ^{55}Fe-source.

In figure 5.67 the projection of the hit distribution for $diff_y = 400\,\mathrm{V}$ and $diff_x = 200\,\mathrm{V}$ at 0 cm is shown. Peak 4 is nearly up to 10 times higher than the others. The reason for this becomes clear in figure 5.68. Only if the source is at 0 cm, photons from the beam core can enter the gas volume between the fourth and fifth lamella leading to an extremely high peak due to the large photon density. It leads to an oval formed hit distribution. If the source is then moved to the right, also the beam core is shifted leaving the lamellar area. Consequently, the frequency from peak 4 decreases constantly up to 3 cm. The other peaks are unaffected because the beam core is already at 0 cm too far away to cause an increased frequency. Since the structured cathode is not directly positioned below the entrance window, the emitted photons first have to pass a gaseous volume before they can enter the lamellar area. Consequently, the beam core position directly above the lamellar area has a general offset compared to its position outside the detector leading to position dependent frequencies and differences in the four peaks.

Another aspect that influences the measurement result is the positioning of the lamellae. Already section 5.3.1 emphasized how the positioning influences the electric field and the resulting electron guiding efficiency. Although these difficulties were fixed, it is possible that a slight displacement of one lamella in the mount still influences the electron guiding. Since this cannot be measured, a proper simulation is performed.

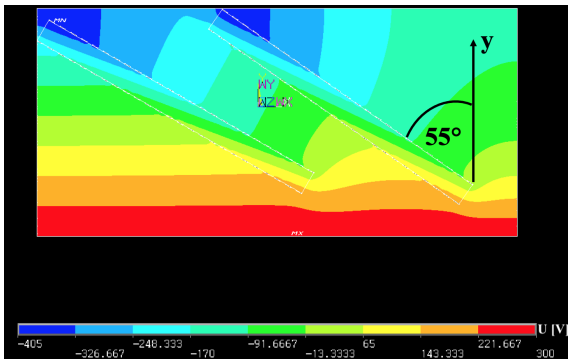

Figure 5.69: While the left lamella is tilted by 60°, the right one has a tilting angle of 55°. For this twisted geometry the resulting potential distribution is plotted.

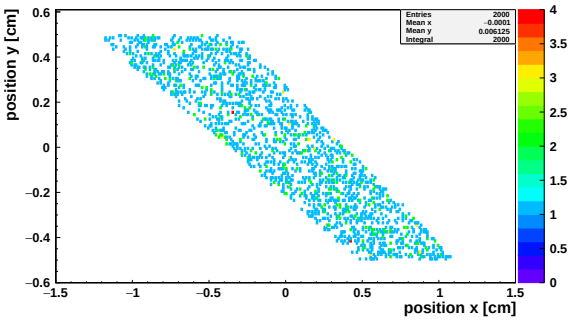

Figure 5.70: Also for the twisted setup the initial electrons are homogeneously distributed between both lamellae.

The used geometry is based on setup 5 (see table 5.1). While the tilting angle of the left lamella is fixed at $\alpha_l = 60°$, the right one is twisted by $\alpha_r = (60 \pm 5)°$ to simulate the influence of a slight twist of the lamella on the electron guiding efficiency. The corresponding potential distribution is shown in figure 5.69 for $\alpha_r = 55°$. For the complete simulation the voltages $diff_y = 400\,\mathrm{V}$, $diff_x = 205\,\mathrm{V}$ (maximum efficiency) and $\Delta U_{\mathrm{drift}} = 100\,\mathrm{V}$ are used. Also, the electron start position is adapted to the geometry as presented in the figures 5.70 for $\alpha_r = 55°$. The initial electrons are homogeneously distributed between both lamellae.

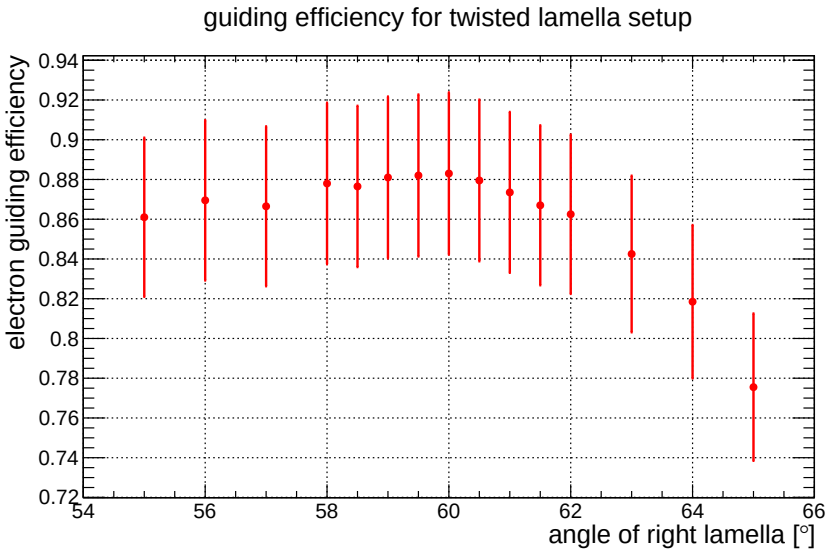

Figure 5.71: The tilting angle of the right lamella is plotted against the electron guiding efficiency.

For tilting angles of $\alpha_r = (60 \pm 2)°$ the electron guiding efficiency is almost unaffected (see figure 5.71). While a tilting angle of $\alpha_r = 55°$ only leads to a decrease of about 2 %, for $\alpha_r = 65°$ a loss of around 10 % is observed. This simulation underlines the impact of misalignments of one lamella on the electric field and the electron guiding efficiency.

5.3.3 Results for Conversion Efficiency using an Am-241 Source

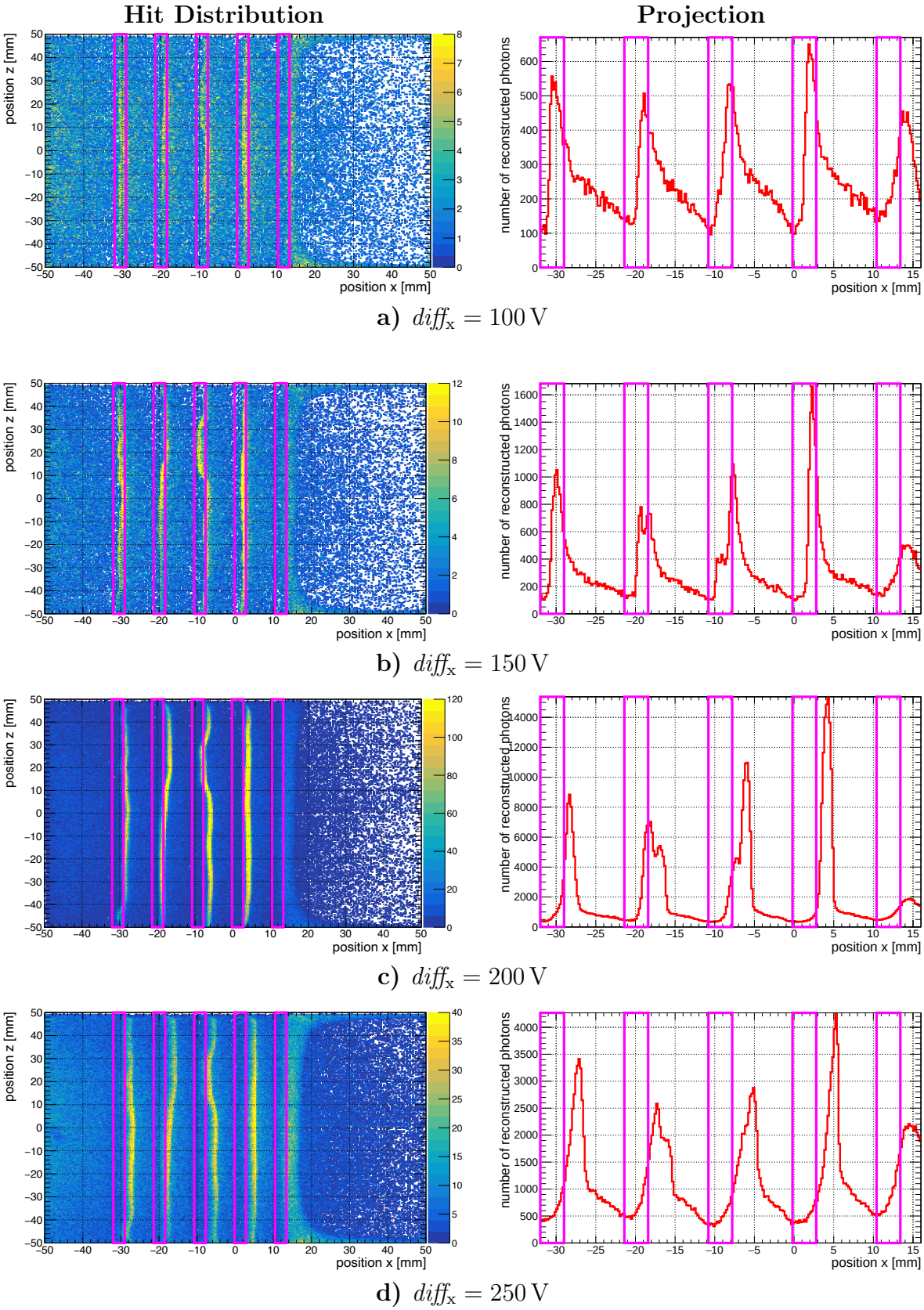

Figure 5.72: While on the left side the measured hit distribution is shown for $diff_y = 400\,V$ and four different $diff_x$ values, the right side shows the corresponding projections in x-direction. Again, the pink boxes represent the lamella boundaries.

The photon conversion in combination with the electron guiding is examined using a ^{241}Am-source introduced in section 5.3.1.4 when the voltages from table 5.2 as well as $\Delta U_{\text{drift}} = 100\,\text{V}$ are applied. For fixed $diff_{\text{y}} = 400\,\text{V}$ and different $diff_{\text{x}}$ the resulting hit distributions are shown in figure 5.72 on the left for $diff_{\text{x}} = 100\,\text{V}$, $diff_{\text{x}} = 150\,\text{V}$, $diff_{\text{x}} = 200\,\text{V}$ and $diff_{\text{x}} = 250\,\text{V}$. The corresponding x-profiles for these voltages are shown on the right of figure 5.72. As for the ^{55}Fe-measurement there are more hits close to the lamellae. The peaks are located close to the left lamella and a clear peak shift with increasing $diff_{\text{x}}$ can be observed. Nevertheless, there are still differences in the peak height for the single peaks. Additionally, the hit distribution of peak 2 ($x = -18\,\text{cm}$) and peak 3 ($x = -7\,\text{cm}$) show irregularities which can be seen in figure 5.72c) (hit distribution) due to wavy lamellae in the detector. In the profiles these irregularities lead to a double peak as shown for example in figure 5.72c) (projection) for $x = -18\,\text{cm}$.

The measurement results are analyzed in the same way presented in section 5.3.2 and compared to the simulation results from section 5.2.6.

5.3.3.1 Electron Guiding Peak

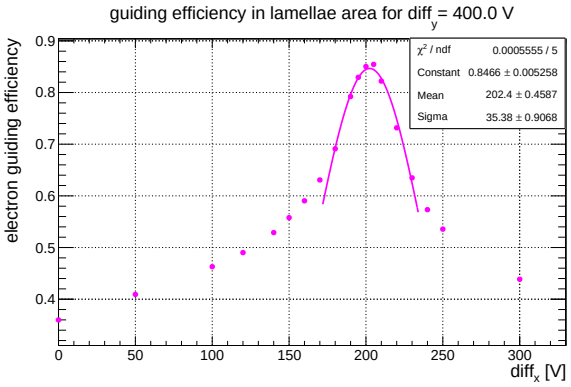

Figure 5.73: The simulated electron guiding efficiency peak has a peak height factor of 2.37 and the Gaussian fit leads to a width of $\sigma = (35.4 \pm 1.0)\,\text{V}$.

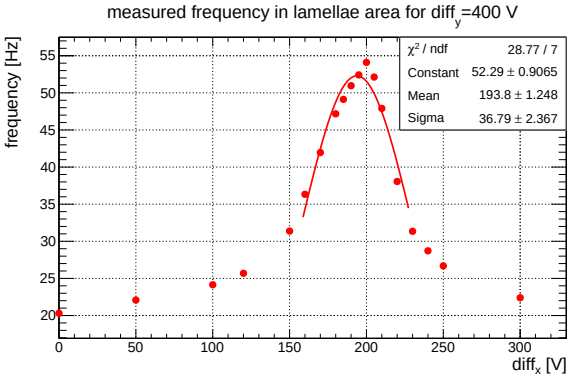

Figure 5.74: Also this measurement results in a frequency peak. It has a peak height factor of 2.64 and according to the Gaussian fit a width of $\sigma = (36.8 \pm 2.4)\,\text{V}$.

For the determination of the electron guiding efficiency and the frequency all four peaks are taken into account. In the simulation an electron guiding efficiency peak with a peak height factor of 2.37 and width of $\sigma = (35.4 \pm 1.0)\,\text{V}$ is calculated (see figure 5.73). Also in the lamellar area a frequency peak is measured as shown in figure 5.74. Its peak height factor of 2.64 is slightly larger than the simulation. The measured width of $\sigma = (36.8 \pm 2.4)\,\text{V}$ corresponds to the simulated one within the limits of accuracy. Additionally, the peak position $diff_{\text{x}}$ for the maximum efficiency shows for simulation ($diff_{\text{x}} = (202.4 \pm 0.5)\,\text{V}$) and measurement ($diff_{\text{x}} = (193.8 \pm 1.3)\,\text{V}$) a good agreement.

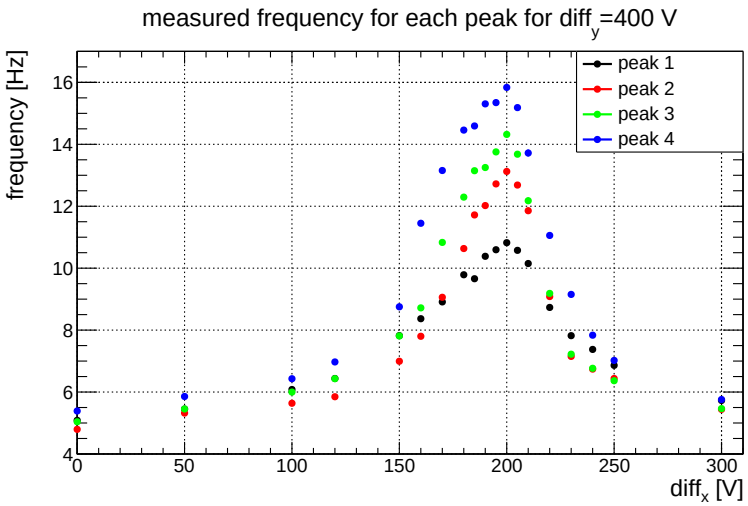

Figure 5.75: The measured frequency in the lamellar area differs for the single peaks. It is the highest for peak 4 and the lowest for peak 1.

The differences of the measured frequencies for the single peaks are shown in figure 5.75. While peak 1 has a peak height factor of 2.12, it is about 1.4 times higher for peak 4 (peak height factor = 2.94). The reason for these differences can be the positioning of the source but also the positioning of the lamellae, which influences the measurement as already presented in figure 5.72c). For the ^{241}Am-measurement not only the lamellar area is investigated but also the complete active area.

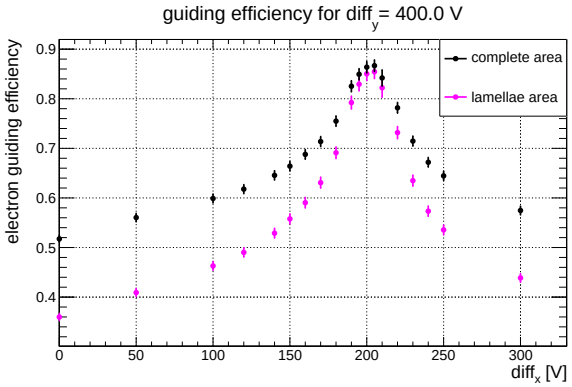

Figure 5.76: For all $diff_x$ values the electron guiding efficiency is higher for the complete area (black dots) compared to the lamellar area (pink dots). Nevertheless the peak height factor is smaller for the complete area in contrast to the lamellar area.

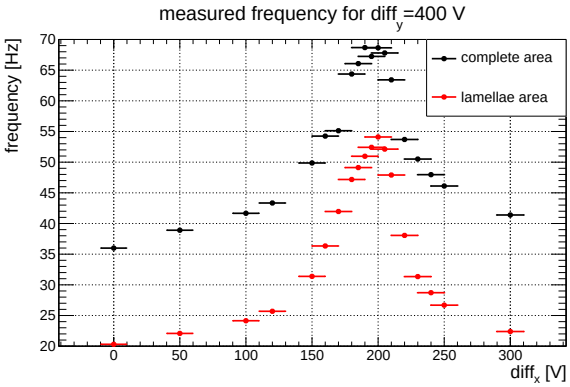

Figure 5.77: The measured frequency in the complete area (black dots) is higher than for the lamellar area (red dots). Nevertheless, the peak height factor in the lamellar area is higher.

Already in section 5.2.6 the influence of the complete gas volume on the simulation is introduced and presented in figure 5.76. The additional electrons which are now taken into account do only change the peak height but not the peak position. For the simulation the peak height factor is about 30 % smaller for the complete area (1.68) compared to the lamellar area (2.37) meaning the peak is less distinct. But due to the additional electrons the peak for the complete area is always higher. While the dimensions of the structured cathode in simulation and measurement are equal, the dimension of the complete area in x-direction differs: In the simulation it has a width of

6.2 cm whereas in the measurement it is 10 cm large. Consequently, in the measurement more electrons outside the lamellar area are detected leading to a higher frequency difference in the complete area compared to the lamellar area as shown in figure 5.77. However, also in the measurement the peak height factor for the complete area (1.91) is about 30 % smaller than for the lamellar area (2.66). But also by considering the complete detector area a frequency peak is observable.

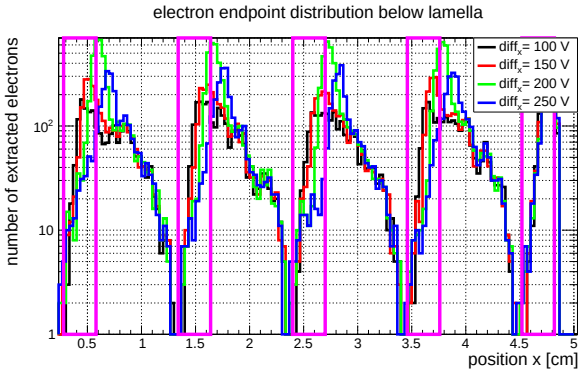

Figure 5.78: The simulated peak position and height below the lamellae for $diff_y = 400\,V$ depends on the applied $diff_x$ value.

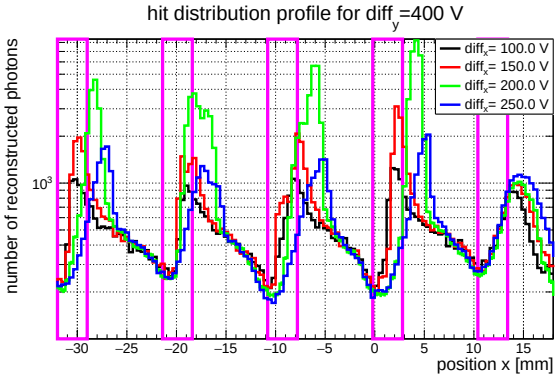

Figure 5.79: For the measurement the distributions are scaled on the measuring time for better comparison. While $diff_y = 400\,V$ is fixed, different $diff_x$ values influence the peak position and height.

The electron distribution below the lamellae is discussed for the simulation in figure 5.78 and for the measurement in figure 5.79. As expected, for these four $diff_x$ values $diff_x = 200\,V$ shows the highest peak. For simulation as well as for measurement the peaks are located close to the left lamella and are shifted to the right with increasing $diff_x$. Nevertheless, the peak shift for the measurement tends to be higher than for the simulation. In order to compare this peak shift more quantitatively, a Landau function is fitted to each peak.

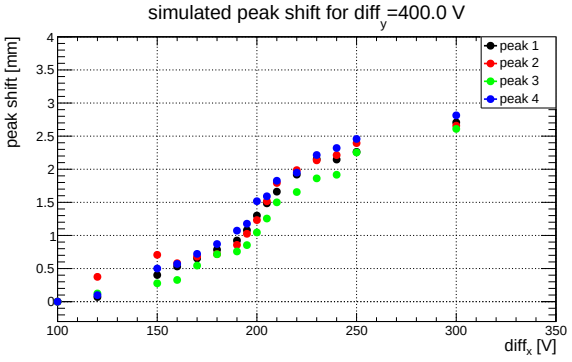

Figure 5.80: The simulated peak shifts are s-shaped and are very similar for all four peaks.

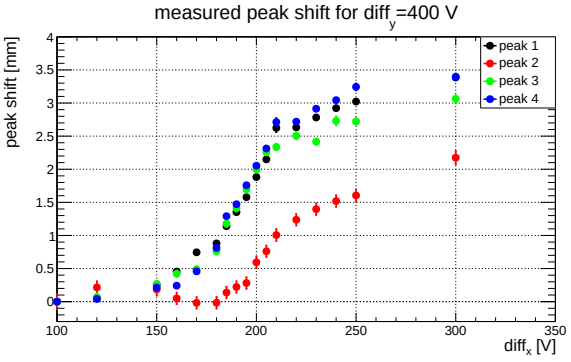

Figure 5.81: Also the measured peak shifts show an s-shape. While the peak shifts for peak 1, peak 3 and peak 4 are similar, it differs for peak 2.

For simulation (figure 5.80) and measurement (figure 5.81) $diff_x$ is plotted against the calculated peak shift. While the peak shift for each simulated peak is very similar, it differs extremely for the measured peak 2. Due to the deformed lamella a double-peak

structure occurs as shown in figure 5.72c). Fitting a proper Landau to this double-peak function is rather difficult and consequently this peak is neglected for the calculation of the average peak shift.

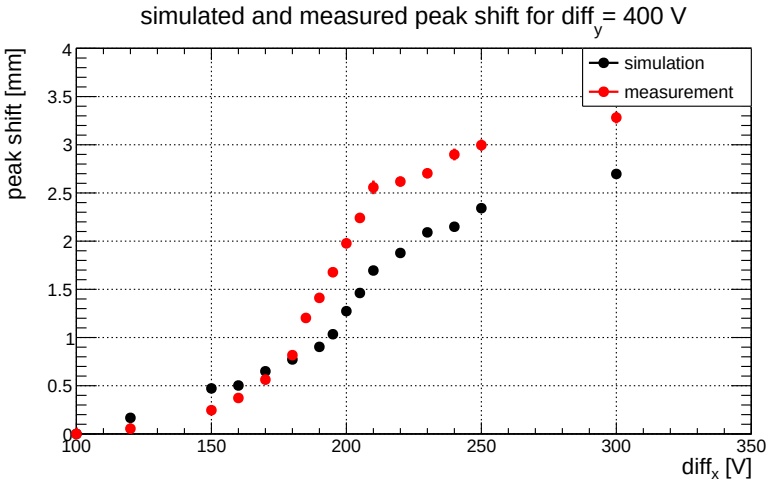

Figure 5.82: The average peak shift from simulation (figure 5.63, black dots) and measurement (figure 5.63, red dots) is plotted as a function of $diff_x$. Both have the expected shape of an inverse tangent function. Especially for high $diff_x$ values the measured peak shift is larger than the simulated one.

This average peak shift can be seen in figure 5.82. For the simulation as well as for the measurement the peak shift has the expected shape of an inverse tangent function. Both show the same tendency although the measured shift is slightly larger probably due to irregularities in the structured cathode setup. The lamellae can be positioned under a slightly different tilting angle or get a wavy structure caused by the fixation of the lamellae in the mount.

Up to now the electron guiding in combination with the photon conversion is examined. Finally, also the influence of the structured cathode on the photon conversion efficiency with a constant electron guiding efficiency is investigated.

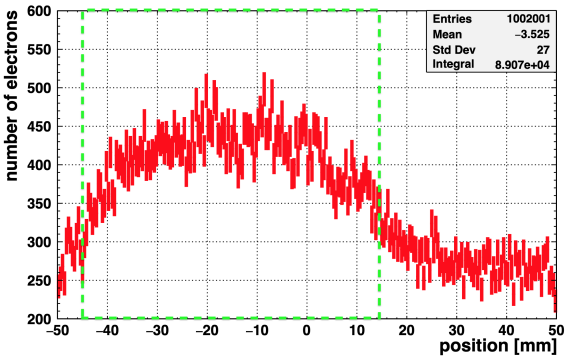

Figure 5.83: In the Geant4 simulation the photon conversion efficiency is higher in the area of the structured cathode (green rectangle) than in the empty gas volume.

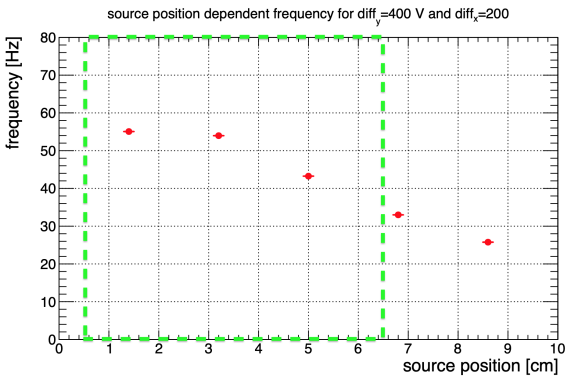

Figure 5.84: The measured frequency for a source position within the area of the structured cathode (green rectangle) is higher than outside.

According to the Geant4 simulation the photon conversion efficiency in the area of

the structured cathode should increase by a factor of 1.6 compared to an empty gas volume (see figure 5.83). Note, that this simulation result does not include the electron guiding. For a corresponding measurement the position of the ^{241}Am-source is changed as shown in figure 5.84. Then the frequency for fixed $diff_y = 400\,\mathrm{V}$ and $diff_x = 200\,\mathrm{V}$ (close to the guiding efficiency maximum) in the complete detector area is measured. While in the simulation the photons enter perpendicular to the detector area, in the measurement the photons have different entrance angles due to the point-like source emission. With the structured cathode the frequency can be increased by a factor of 2 compared to a pure gas volume. That means, the structured cathode improves the photon conversion efficiency as intended.

5.4 Conclusion

All in all, the comparison between simulation and measurement show a very good agreement regarding the electron guiding efficiency and the peak shift of the electron distribution for the ^{55}Fe as well as the ^{241}Am-measurement. Reasons for slight deviations are the source position, the tolerance of the power supply and the positioning of the lamellae inside the detector. With this structured cathode the total photon conversion can be increased by a factor of 1.4 from about 0.33 % (pure gas) to 0.45 % according to the Geant4 simulation. The conversion probability can be further increased, for example by decreasing the distance between the lamellae which leads to a larger overlap. In this thesis the optimized structured cathode works as intended and increases the measured detection efficiency of 60 keV photons by a factor of 2 compared to a pure gas volume.

Chapter 6

Neutron Detection

In this chapter the detection of neutrons is investigated by using a ^{10}B converter layer which is placed inside a GEM detector. With this setup various imaging processes are performed. Therefore, an object is placed in a particle beam in front of a detector. Since the object absorbs parts of the radiation a shadow is detected leading to an image of this object.

6.1 Theoretical Principle

Since neutrons are electrically neutral, they only show a poor detection efficiency in gaseous detectors. As motivated in section 2.1.3 it can be increased by using a Boron-10 converter cathode which can capture the neutron in the following process

$$^{10}\mathrm{B} + \mathrm{n} \longrightarrow {}^{7}\mathrm{Li} + {}^{4}\mathrm{He} \; + 2.8\,\mathrm{MeV}$$

producing an α-particle and a Lithium-particle and additional 2.8 MeV energy. These reaction products are then used for detection (see section 6.2.2).

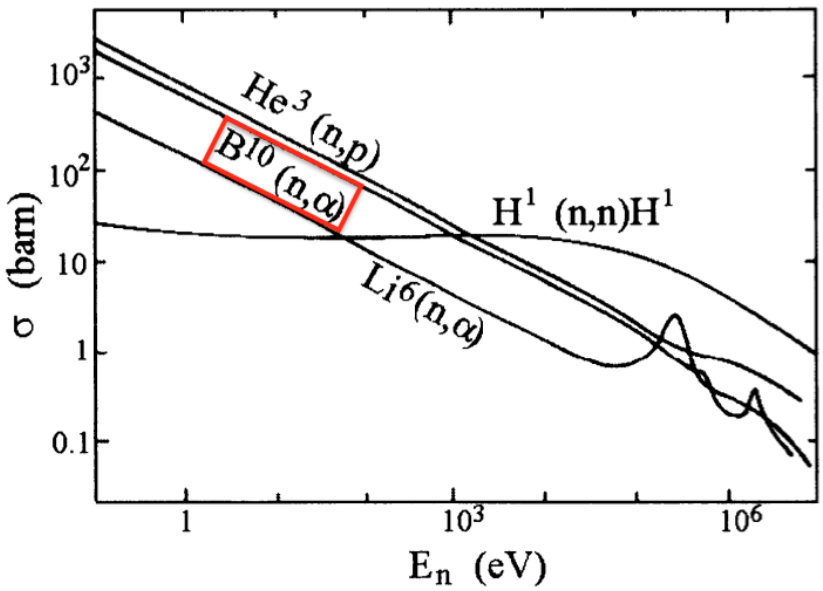

Figure 6.1: Cross Section for neutron induced reactions plotted against the neutron energy E_n with logarithmic scaling (x- and y-axis). In this thesis ^{10}B (red rectangle) is used for neutron detection (taken from [6]).

As shown in figure 6.1 the neutron cross section σ decreases linearly with increasing neutron energies E_n for the ^{10}B converter cathode in the log-log-diagram because σ is proportional to $1/\sqrt{E_n}$ (see section 2.1.3). Especially for thermal neutrons which have typically energies below 100 meV the cross section is with $\sigma > 1000$ barn high. For neutrons with energies in the MeV region the cross section is more than 10^3 times smaller. In the performed measurements such a ^{10}B converter cathode is used for particle detection.

6.2 Measurement at the Tandem van de Graaf Accelerator in Garching

The measurements are performed at the Tandem van de Graaf Accelerator in Garching [26] and the focus lies on the imaging of different objects. For better comparison corresponding Geant4 simulations are carried out.

6.2.1 Setup

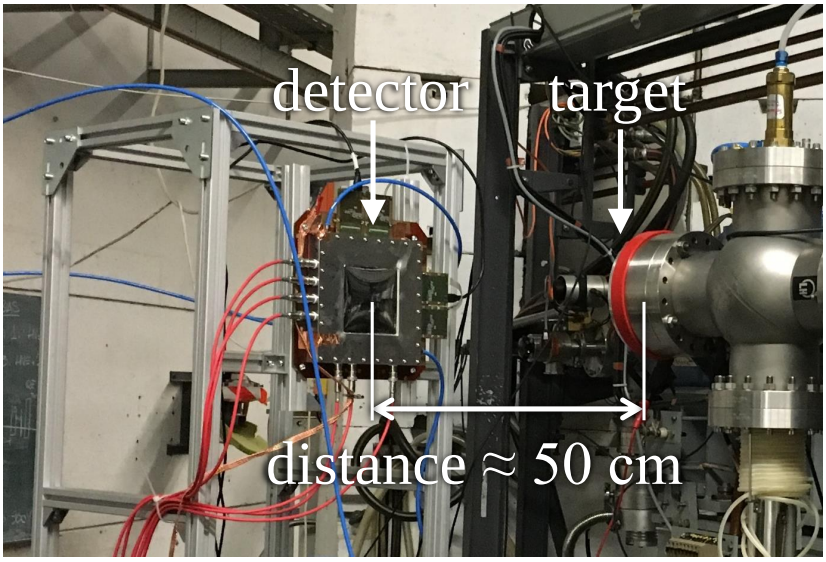

Figure 6.2: The GEM detector is positioned with a distance of about 50 cm directly in front of the target where the particles exit the beam pipe.

In figure 6.2 the general measurement setup is shown. During a measurement a 20 MeV deuteron beam hits a target made of Beryllium and Aluminum. In this interaction process mainly photons and neutrons are created which can leave the target and are detected with a GEM detector. It is positioned in a distance of about 50 cm. In order to get a better understanding of the ongoing processes a corresponding Geant4 (see section 4.1) simulation is performed to model the particle production.

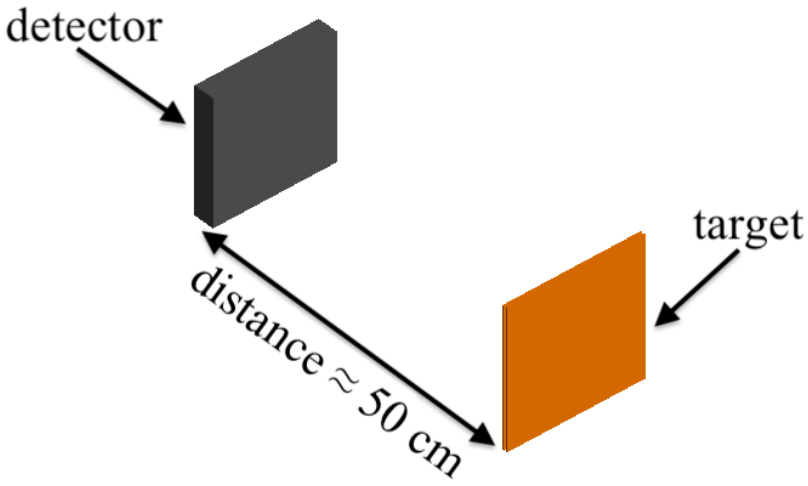

Figure 6.3: A detector is placed at a distance of 50 cm from the target in the Geant4 simulation.

First, the setup is modeled. A target made of Beryllium and Aluminum (each has a thickness of 2.5 mm) is positioned 50 cm off the detector as shown in figure 6.3. While in the measurement 20 MeV deuterons hit the target, the simulation is performed with 25 MeV deuterons. After the target is irradiated with these deuterons the number of created particles including their type and energy is counted in the detector volume in the simulation. In this process about 33 % photons and 67 % neutrons are created.

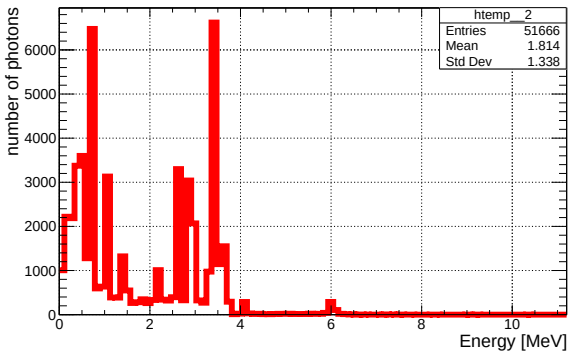

Figure 6.4: In the simulated photon energy spectrum there are single energy peaks below 6 MeV.

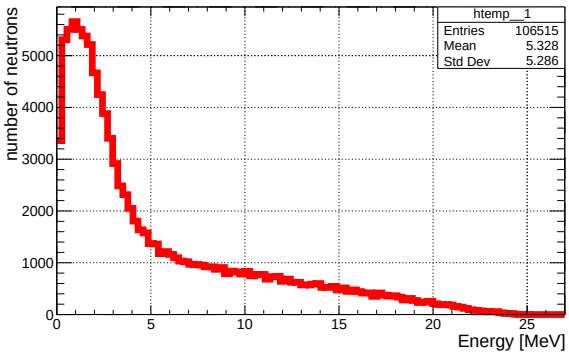

Figure 6.5: The simulated neutron spectrum created by 25 MeV deuteron breakup has a peak at 1 MeV and a tail to energies up to 25 MeV.

The resulting simulated energy spectrum for photons is shown in figure 6.4 and for neutrons in figure 6.5. While there are several photon energy peaks below 6 MeV due to the photon resonances, the neutron energy spectrum shows one peak at 1 MeV with a tail to energies up to 25 MeV. Since most of the neutrons have energies in the MeV range, the cross section is in the order of 1 barn and the detection efficiency for these neutrons is quite low (see figure 6.1). There are also a few neutrons in the beam with lower energies. For them the detection probability is higher according to figure 6.1. It can be assumed that the detected neutrons have a wide energy range meaning thermal as well as MeV neutrons are measured.

6.2.2 Detection Mechanism

As the previous simulation shows, the beam consists of a certain amount of photons and neutrons. Since both particles can interact with the used ^{10}B cathode inside the detector creating ionization charge, a method for particle distinction is necessary.

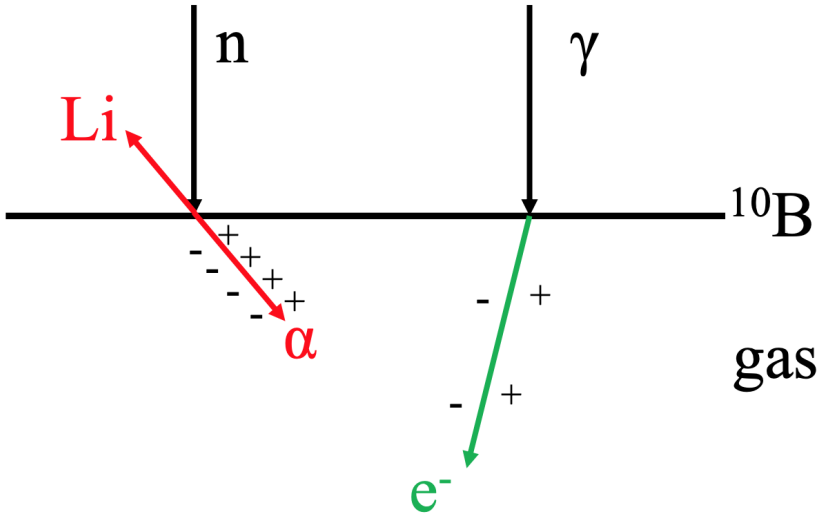

Figure 6.6: In the neutron interaction process (left) with the ^{10}B cathode a Li- and α-particle is emitted back-to-back leading to ionization in the gas volume. If a photon interacts (right) with the ^{10}B cathode, a photoelectron is created. In case the electron can leave the cathode, it ionizes the detector gas. For α particles more charge is deposited than for electrons.

Figure 6.6 shows the interaction process of neutrons and photons with a ^{10}B cathode inside a gaseous detector. In the neutron capture process a Li- and α-particle are emitted back-to-back which ionize the detector gas. Due to their high mass they gain only little kinetic energy and consequently they have a short range. According to the Bethe-Bloch formula (see section 2.1.1) they experience a high energy loss leading to dense ionization. For a photon interaction with the ^{10}B cathode a photoelectron is created. If its kinetic energy is large enough to leave the cathode it also ionizes the gas. Due to the photon energy Compton scattering occurs leading to low-energetic electrons compared to the energy of the reaction products of the neutron capture process. Consequently, the electrons deposit less charge than the neutrons inside the detector. With a proper chosen amplification voltage it is possible to distinguish both particles. With a low voltage the amplification for the created electron charge is too small to be measurable whereas the signal of the neutron reaction products is high enough due to the larger amount of charge created in the ionization process. In order to distinguish visually between photons and neutrons the ^{10}B cathode is modified.

Figure 6.7: On the bottom side of the ^{10}B cathode a copper tape is placed.

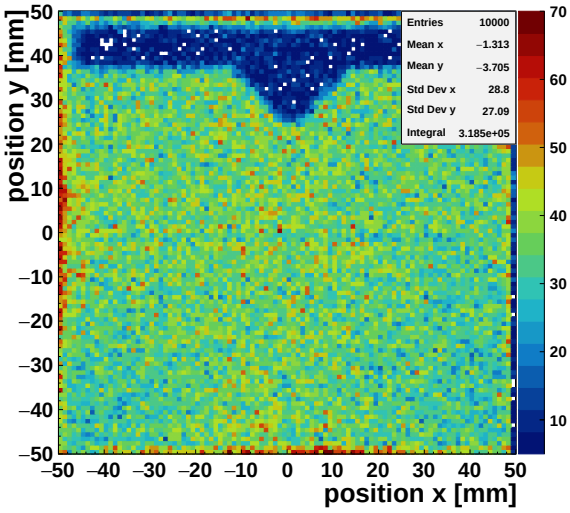

Figure 6.8: This copper tape is visible in the measured hit distribution.

The converter cathode consists of a 0.5 mm thick Aluminum layer coated with 2 µm ^{10}B. Additionally, a 0.05 mm copper tape with a triangle is placed on the bottom side of the cathode. Since the range of a Li- and α-particles in copper are only a few µm [27], they are absorbed whereas electrons can pass it easily. With this cathode structure measurements are performed according to figure 6.7. The cathode with this copper structure is placed inside a GEM detector which is flushed with a gas mixture of 93:7 vol. % Ar:CO_2 for all measurements in this chapter. Also it is connected to the readout electronics from section 3.2 and the high voltage power supply with the voltages presented in table 6.1. With these voltages mainly neutrons are detected.

GEM1B	GEM1T	GEM2B	GEM2T	GEM3B	GEM3T	cathode
−600 V	−900 V	−1400 V	−1600 V	−2100 V	−2315 V	−2700 V

Table 6.1: To provide sufficient gas amplification the listed voltages are applied at the GEM foils inside the detector to examine the detection mechanism for photons and neutrons. The naming corresponds to figure 3.3 and the ending 'B' stands for the bottom side and 'T' for the top side of one GEM foil. Additionally, the voltage applied at the ^{10}B cathode is provided.

For data recording in this chapter mmdaq (see section 3.3) is used. The resulting hit distribution is shown in figure 6.8 where the copper structure is clearly visible with less entries. That means, in the rest of the active volume neutrons are measured where they are homogeneously distributed. Furthermore, the entries in the copper tape region are created by photons since all reaction products from neutrons are absorbed. If only photons are detected, the copper tape structure is no longer visible as shown in figure 6.18. This copper tape structure is used as verification method for neutron detection.

6.2.3 Imaging Processes

This setup and detection mechanism is now used for imaging processes. In total three different objects are imaged: blocks of different materials, a steel rod and a lead bunny. In some cases the results are compared to corresponding Geant4 simulations.

6.2.3.1 Imaging of Blocks

Simulation

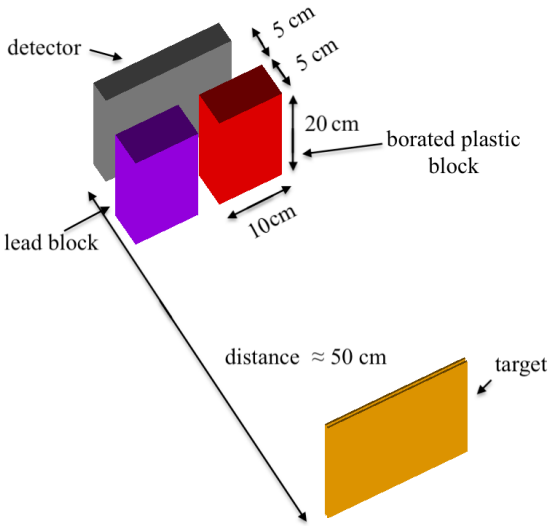

Figure 6.9: In the Geant4 simulation between target and detector a lead block (purple, left) and a borated plastic block (red, right) are positioned at a certain distance. Each block has a height of 20 cm, width of 10 cm and thickness of 5 cm.

First, the setup is modeled in Geant4. To the previous setup (figure 6.3) two blocks are added as shown in figure 6.9. One block is made of lead and the other of borated plastic. Then the blocks are irradiated with photons and neutrons with the energies as simulated in section 6.2.1. With this simplified geometry the inside of the blocks can be studied. Therefore, in the simulation the detector counts the number of passing neutrons and photons. The interaction processes and corresponding quantities like the energy loss which are used for particle detection in the measurement are not taken into account in the simulation.

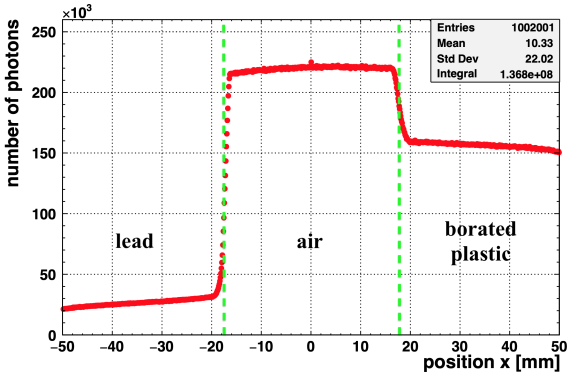

Figure 6.10: In the simulation the number of detected photons differ for the lead block, air and the borated plastic block.

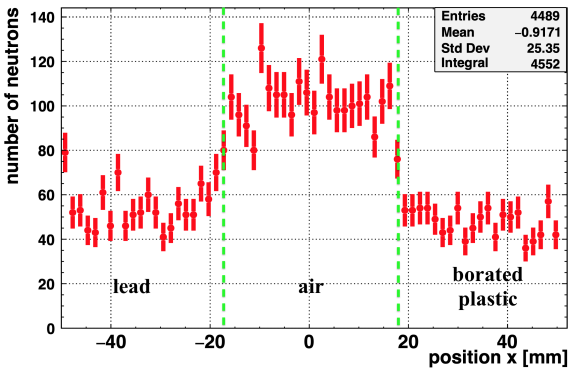

Figure 6.11: The absorbed neutrons for both blocks are nearly the same according to the simulation.

In the simulation the number of detected photons (see figure 6.10) and neutrons (see figure 6.11) are counted separately. According to the simulation the lead block absorbs about 90 % of the photons whereas for the borated plastic block it is 30 % less compared

to air. According to equation 2.2 the corresponding linear attenuation coefficient μ is calculated with these simulation results: $\mu = 0.46\,\mathrm{cm}^{-1}$ for lead and $\mu = 0.07\,\mathrm{cm}^{-1}$ for borated plastic. For photons both blocks should be visible and also distinguishable. Figure 6.11 shows that about 50 % of the simulated neutrons are absorbed by each block leading to $\mu = 0.14\,\mathrm{cm}^{-1}$ for both materials. As a consequence both blocks should be visible in an imaging process but their separation is less clear.

Measurement

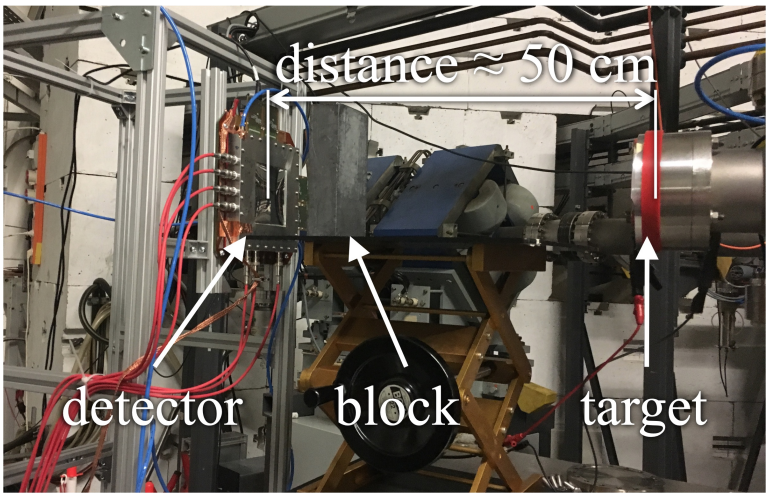

Figure 6.12: In the real setup one block is positioned between detector and target.

For the measurement a single block is placed between target and detector as shown in figure 6.12. It is either made of lead or borated plastic. Both blocks are irradiated with neutrons. The voltages from table 6.2 are applied for a measurement detecting mainly neutrons.

GEM1B	GEM1T	GEM2B	GEM2T	GEM3B	GEM3T	cathode
−600 V	−900 V	−1400 V	−1600 V	−2100 V	−2315 V	−2600 V

Table 6.2: These voltages are applied at the GEM foils inside the detector for the imaging process of both lead blocks with neutrons. The ending 'B' stands for the bottom side and 'T' for the top side of one GEM foil. Additionally, a voltage is applied to the ^{10}B cathode.

Since for measurements with photons higher voltages are needed (see section 6.2.2), the voltages from table 6.3 are applied.

GEM1B	GEM1T	GEM2B	GEM2T	GEM3B	GEM3T	cathode
−600 V	−950 V	−1400 V	−1600 V	−2100 V	−2350 V	−2635 V

Table 6.3: These voltages are applied at the GEM foils inside the detector for imaging the steel rod with photons. The ending 'B' stands for the bottom side and 'T' for the top side of one GEM foil. Additionally, a voltage is applied to the ^{10}B cathode.

The corresponding photon measurement is performed in section 6.2.3.2. In this section the imaging process of two different blocks with neutrons is examined using the voltages from table 6.2. First, the lead block is positioned in the particle beam.

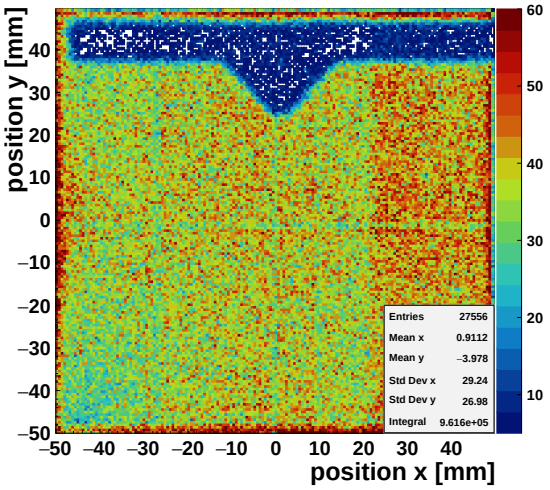

Figure 6.13: In the area between $x = -50\,\text{mm}$ and $x = 20\,\text{mm}$ less entries are observed in the measured hit distribution. This is the region were the lead block is located.

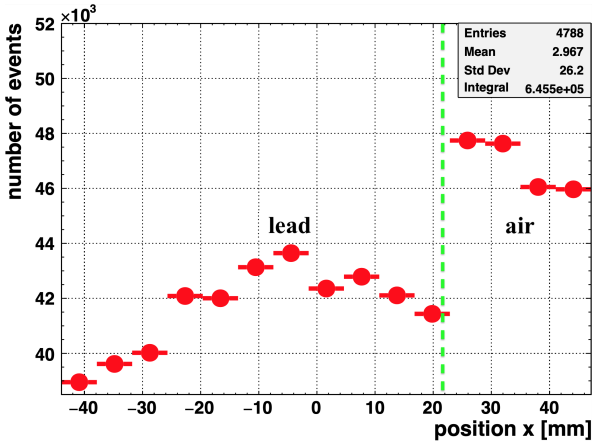

Figure 6.14: Here the corresponding x-projection of the hit distribution is shown. The lead block absorbs about 10 % while 50 % are expected from simulation.

The measured hit distribution with the lead block is shown in figure 6.13. It is located in the area between $x = -50\,\text{mm}$ and $x = 20\,\text{mm}$. Exactly in this area less entries are measured. Since the copper structure on the top of the hit distribution is visible, mostly neutrons are measured. Some of the neutrons are absorbed by the lead block. This can also be observed in figure 6.14 which shows the x-projection of the hit distribution. The lead block absorbs about 10 % of the particles whereas the simulation for neutrons predicts an absorption of 50 %.

In the next measurement the lead block is replaced by a block made of borated plastic while the rest of the setup is the same.

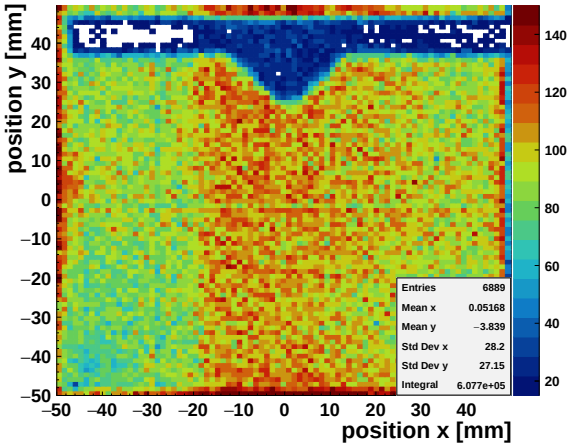

Figure 6.15: The measurement with the borated plastic block shows less entries in the area between $x = -50\,\text{mm}$ and $x = -20\,\text{mm}$ where the borated plastic block is placed.

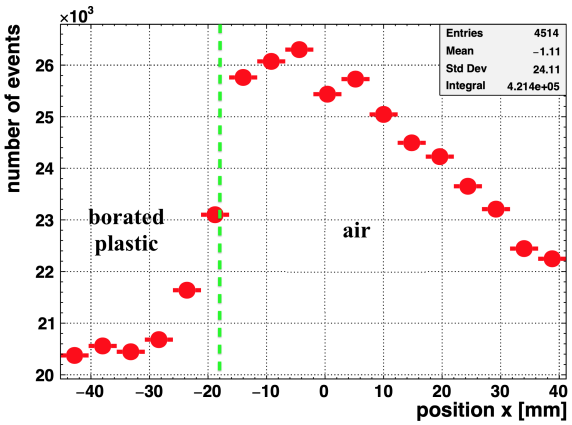

Figure 6.16: The differences between both areas with and without borated plastic block are better visible by considering the x-projection of the hit distribution.

In this measurement the borated plastic block is located in x-range between $x = -50\,\text{mm}$ and $x = -20\,\text{mm}$ where also less particles are detected (see figure 6.15).

Again, the x-projection in figure 6.16 shows a decrease of about 15 % in the area where the block is located while in the simulation 50 % are absorbed.

Differences between Simulation and Measurement
Although both blocks can be identified in the measurement, there are differences compared to the simulation. While in the simulation only neutrons are considered, in the measurement a combination of photons and neutrons is in the beam. Additionally, the measurement is influenced by the surrounding which leads to backscattering and moderation of neutrons. These effects are not included in the simulation but is further investigated in section 6.2.3.4. Also there are differences in the energy loss. The block in the beam causes neutron scattering which changes the initial neutron energy. Consequently, in the measurement one part of the neutrons is absorbed by the block and the other is scattered and detected. Due to the higher detection probability for lower neutron energies (see figure 6.1), the neutrons which are scattered in the block are more likely to be detected than the neutrons detected in the region with air. This process is not considered in the simulation since only the number of passing neutrons is counted. Consequently, the absorption curve in the measurement is less pronounced. These effects are reasons for the differences between simulation and measurement.

6.2.3.2 Imaging of a Steel Rod

Figure 6.17: This steel rod is positioned between target and detector for imaging.

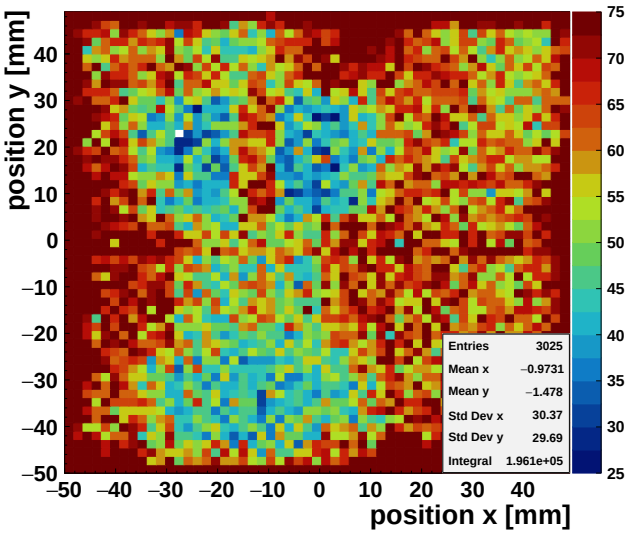

Figure 6.18: In this measured hit distribution the steel rod is visible. The copper structure on the top cannot be seen.

Since the imaging with neutrons worked in the previous section, the imaging with photons is now investigated. Therefore the steel rod from figure 6.17 is placed in the beam and the voltages from table 6.3 are applied while the rest of the setup is identical to the one before. The resulting hit distribution is shown in figure 6.18 where the copper tape structure on the top of the cathode is not visible meaning there are mostly photons detected. With these photons the steel rod is clearly imaged including its contours and also the little gap in the middle (between $x = -18\,\text{mm}$ and $x = -10\,\text{mm}$ as well as $y = 5\,\text{mm}$ and $y = 30\,\text{mm}$).

6.2.3.3 Imaging of a Lead Bunny

Since the imaging of both blocks and the steel rod works very well, now a lead bunny is imaged. As for the steel rod, this measurement aims for investigating the absorption of photons.

Simulation

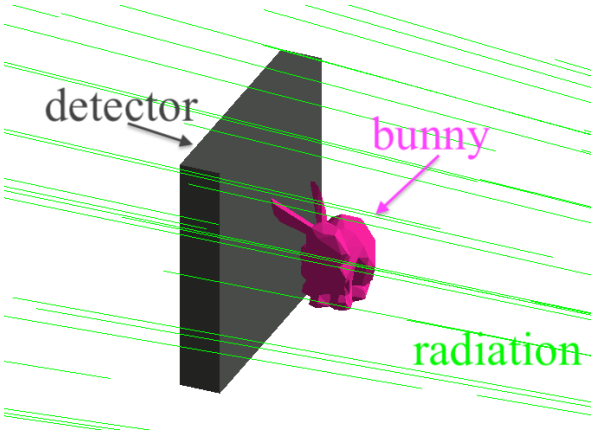

Figure 6.19: In the Geant4 simulation the lead bunny is positioned in the front of the detector and irradiated with photons.

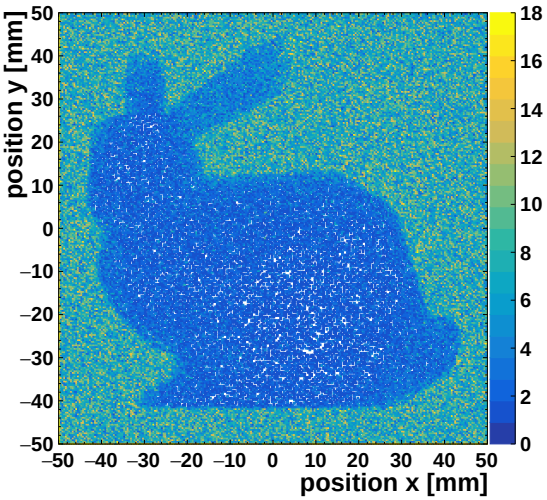

Figure 6.20: In the simulated hit distribution the lead bunny is clearly visible.

First, the imaging process of the lead bunny is simulated with Geant4. Therefore, the bunny is placed in front of the detector and is irradiated with photons as shown in figure 6.19. According to the simulation result (see figure 6.20) the bunny is clearly visible.

Measurement

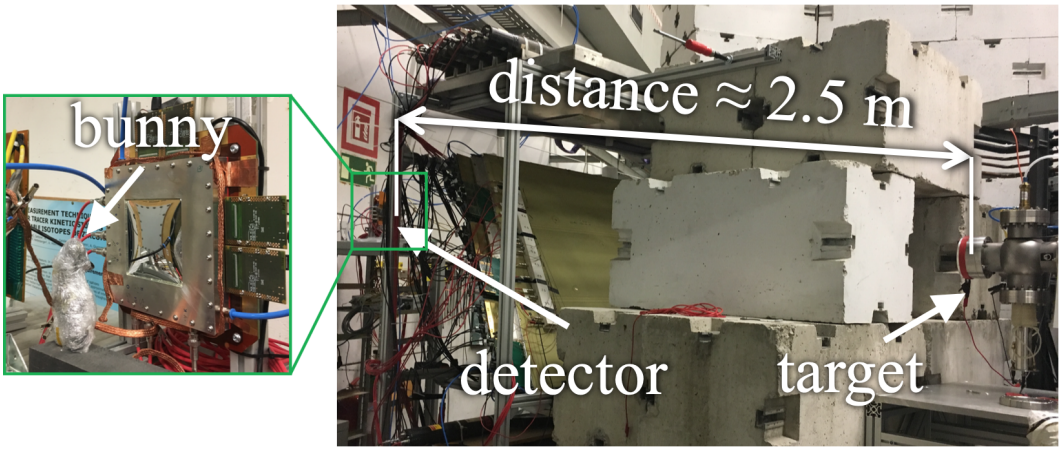

Figure 6.21: For this measurement the distance between target and detector is about 2.5 m and various other objects are between them (right figure). The lead bunny is positioned in front of the detector (left figure).

This measurement setup differs from the previous one as presented in figure 6.21. Now the distance between target and detector is about 2.5 m and several objects for other measurements which are performed in parallel are placed in between. The bunny made of lead is directly positioned in front of the detector. Although various voltages are used for the measurement, the results are always similar. For the presented one the voltages from table 6.4 are applied aiming to measure photons.

GEM1B	GEM1T	GEM2B	GEM2T	GEM3B	GEM3T	cathode
−600 V	−900 V	−1400 V	−1600 V	−2000 V	−2350 V	−2635 V

Table 6.4: These voltages are applied at the GEM foils inside the detector for imaging the lead bunny. The naming corresponds to figure 3.3 and the ending 'B' stands for the bottom side and 'T' for the top side of one GEM foil. Additionally, a voltage is applied to the ^{10}B cathode.

Figure 6.22: This lead bunny is positioned in front of the detector.

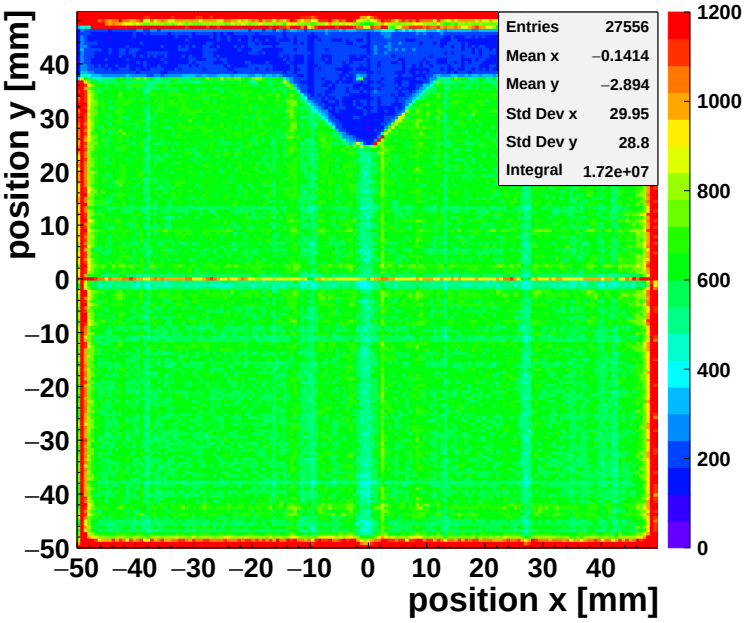

Figure 6.23: But on the resulting hit distribution the bunny is not visible. Nevertheless, the copper structure can be seen.

On the resulting hit distribution (see figure 6.23) the lead bunny from figure 6.22 is not visible but instead the copper structure. Consequently, mostly neutrons are detected leading to a homogeneous distribution in the area where the bunny is expected. Since the simulation is performed with photons and in the measurement neutrons are detected, both results cannot be compared. The imaging process does not work properly as in the previous measurements which can have different reasons. On the one hand the distance between target and detector is larger and there are other objects in the beam which can scatter and moderate the neutrons and photons. But on the other hand the detector is also placed in front of a concrete wall (see figure 6.21) which can cause backscattering. This is now investigated in section 6.2.3.4 in more detail.

6.2.3.4 Influence of a Concrete Wall

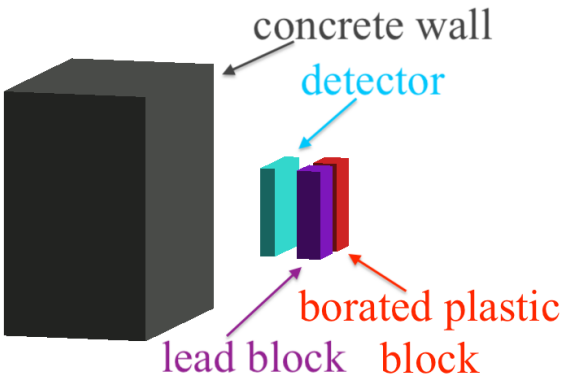

Figure 6.24: The detector as well as both blocks are placed in front of a concrete wall.

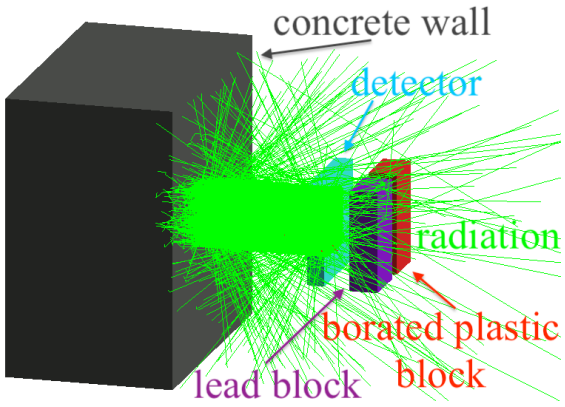

Figure 6.25: This setup is irradiated and some of the particles are backscattered.

For a better understanding of the influence of the concrete wall on the simulation results, the setup with both blocks is complemented by a concrete wall as shown in figure 6.24. Due to the concrete wall the incoming neutrons are backscattered (see figure 6.25) and influence the measurement result.

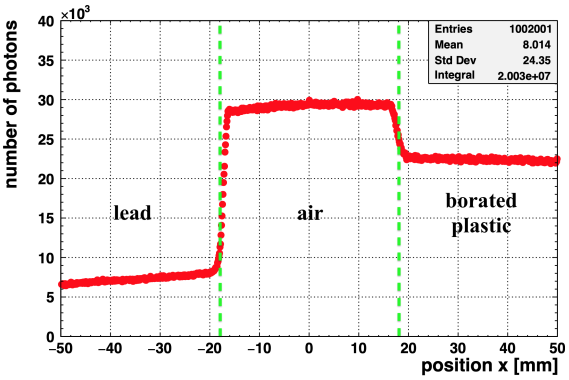

Figure 6.26: The number of detected photons still differs for lead, air and borated plastic.

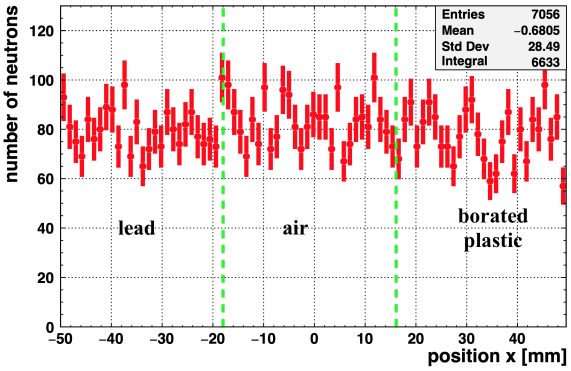

Figure 6.27: For all three materials the number of detected neutrons is equal.

The influence of the concrete wall on the simulation result is shown for photons in figure 6.26 and for neutrons in figure 6.27. Since photons are less likely to be backscattered, the concrete wall has nearly no influence on the simulation result. Still the number of detected photons differs for all three materials so that they can be distinguished. Nevertheless, the concrete wall affects the neutron detection since they are more likely to be backscattered. For all three materials the number of counted neutrons in the simulation is identical which makes imaging impossible. The consideration of the corresponding neutron energy spectrum emphasizes the difficulties.

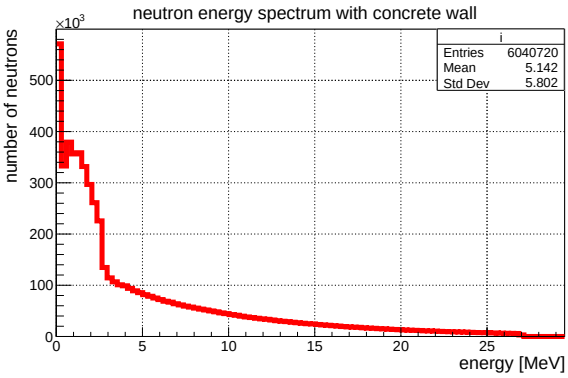

Figure 6.28: The neutron energies with the concrete wall created by 25 MeV deuteron breakup range up to 25 MeV including a peak for low energies.

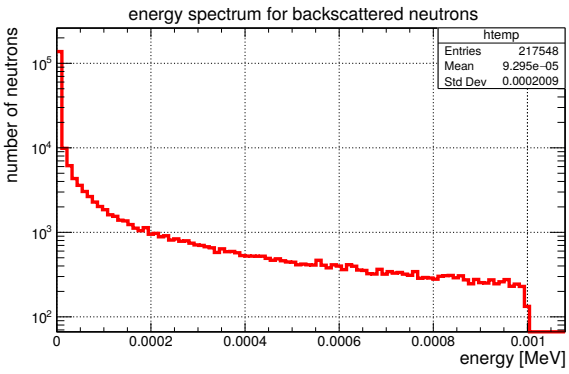

Figure 6.29: All backscattered neutrons have energies less than 0.1 keV (logarithmic scale).

As shown in figure 6.28 the concrete wall influences the neutron energy spectrum. The original spectrum from figure 6.5 has an additional peak for energies below 0.5 MeV. This peak occurs from the backscattered neutrons (see figure 6.29). Due to the backscattering the neutrons suffer an energy loss leading to energies below 0.1 keV. Since with decreasing neutron energy the detection probability increases (see figure 6.1), their interaction probability is higher than for the initial neutrons. Consequently, the backscattered neutrons dominate and no imaging for objects positioned in front of the detector is possible.

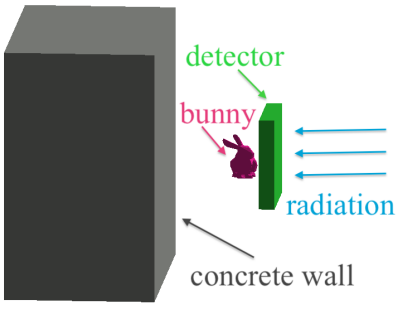

Figure 6.30: In this Geant4 simulation setup the bunny is placed between detector and concrete wall.

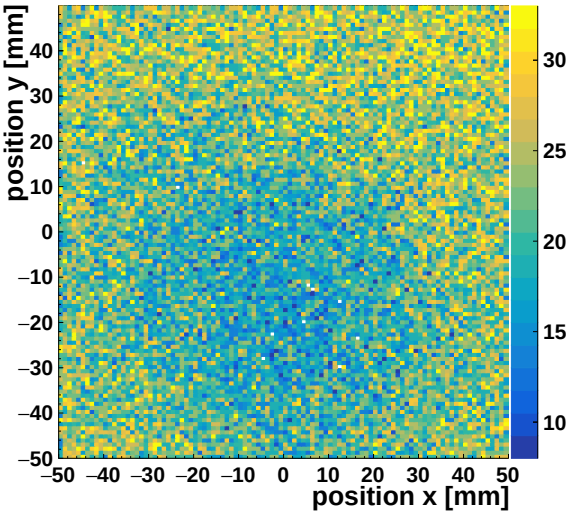

Figure 6.31: For the resulting hit distribution less entries are observed in the area where the bunny is located.

With the simulation setup from figure 6.30 it is tested if the backscattered neutrons can be used for imaging. Therefore, the lead bunny is placed between concrete wall and detector and the whole setup is irradiated. In the resulting hit distribution in figure 6.31 there are less entries in the region where the bunny is located but a precise shape is not observable. So with this configuration the imaging with backscattered particles is partially possible, but it again emphasizes the huge impact of backscattered neutrons on the simulation and consequently also on the measurement result.

6.3 Conclusion

The imaging of both blocks with neutrons and the steel rod with photons works as intended and all these objects are visible. Nevertheless, there are some differences between simulation and measurement because the simulation is performed with a simplified setup. Neither the energy loss of particles nor the surrounding are taken into account. However, as further simulation show, especially the environment influences the result like the concrete wall which causes backscattering of neutrons. Due to this backscattering the lead bunny cannot be imaged since the detector was directly placed in front of a concrete wall compared to the previous measurements. But also all other objects in the real setup scatter or moderate the neutrons and impacts the result. Nevertheless, by choosing a proper measurement setup the detection of neutrons as well as photons is possible and can be used for imaging processes.

Chapter 7

Summary and Outlook

In this thesis the detection of electrically neutral particles with a GEM detector is investigated using different detection techniques for photons and neutrons.

For an improved detection efficiency a structured cathode is optimized regarding its geometry and electric field configuration. Its main component are lamellae which are made of 35 µm thick copper strips on an 1.5 mm standard PCB which are connected with resistors. The structured cathode consists of five lamellae which are placed under a certain angle with large overlap inside a GEM detector in order to increase the photon conversion efficiency. In an interaction process electrons are created. For detection they have to be guided from their position between both lamellae to the amplification and readout area of the detector which is achieved by a proper electric field configuration. Therefore, a voltage difference between top and bottom of one lamella $diff_{\mathrm{y}}$ and between the two adjacent lamellae of $diff_{\mathrm{x}}$ is applied. An optimized voltage pair $diff_{\mathrm{y}}$ and $diff_{\mathrm{x}}$ leads to a maximized electron guiding efficiency. In the measurements the electron guiding is investigated using an ^{55}Fe source while for the conversion process and an ^{241}Am source is used. The results are compared to corresponding simulations based on Geant4, ANSYS and Garfield++. For both measurements the results show a very good agreement with the simulation regarding the electron guiding efficiency as well as the electron distribution below the structured cathode area. For $diff_{\mathrm{y}} = 400\,\mathrm{V}$ a maximum efficiency of about 88 % is achieved in the region of $diff_{\mathrm{x}} = (200 \pm 10)\,\mathrm{V}$. The resulting peak for simulation has also the same width and approximately the same height. For the electron distribution below the structured cathode a peak shift of some mm is observed. Especially, the positioning of the lamellae influence the measurement results due to a wavy structure leading to slight discrepancies between simulation and measurement. Nevertheless, the structured cathode increases the conversion efficiency of 59.5 keV photons by a factor of two compared to pure gas which shows that it works as intended.
Up to now, there are no information regarding the position of the photon conversion. In a next step a method for position reconstruction can be investigated for example by considering different parameters like deposited charge or timing or a further adaption of the structured cathode design to get more necessary information.

For the detection of neutrons a ^{10}B cathode is used and measurements at the Tandem van de Graaf Accelerator in Garching are performed. Different objects are placed in the beam to study their absorption behavior and reconstruct their image. The par-

ticle beam consists of photons and neutrons between 1 MeV and 25 MeV. In order to distinguish visually between them a copper tape structure is added to the ^{10}B cathode. Also both particles can be differentiated by the used amplification voltage. With this cathode the imaging processes are carried out and are compared to a Geant4 simulation. The imaging of both blocks with neutrons as well as the imaging of a steel rod with photons works properly. Due to the backscattering of neutrons from a concrete wall a lead bunny cannot be imaged with photons because the less energetic backscattered neutrons dominate the measured distribution. In general, the neutrons are scattered or moderated by objects around the measurement setup leading to differences between simulation and measurement.
In order to reconstruct the bunny image, the data analysis can be adapted by excluding backscattered neutrons for example by their energy and other parameter. For future measurements the neutron backscattering can be prevented by adding an absorber (for example paraffine or water) between the detector and the concrete wall.

The final idea is to combine both methods to improve the neutron detection efficiency by adapting and optimizing the structured cathode design.

Appendix A

Printed Resistors

The single copper strips on the lamella are connected with a printed resistor.

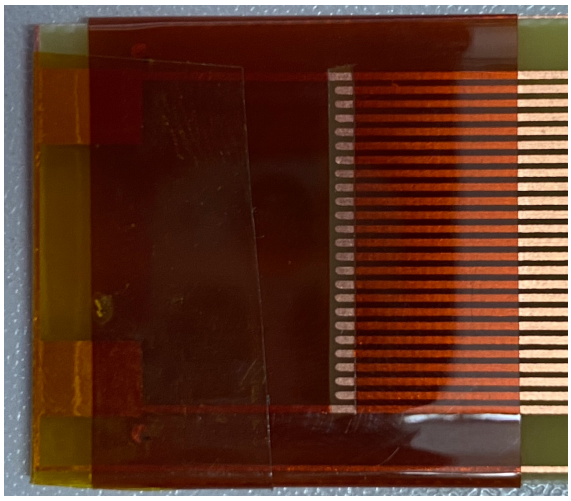

Figure A.1: The size of the printed resistor is defined with a Kapton tape.

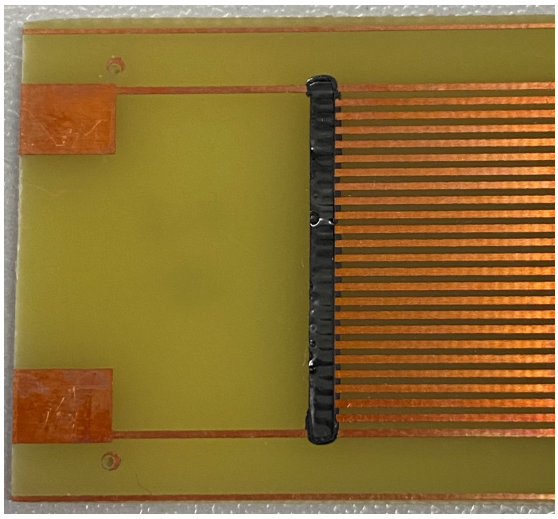

Figure A.2: The printed resistor (black) connects all copper strips.

Therefore, the size of the resistor is defined by a 60 µm thick Kapton tape as shown in figure A.1. The free area with a height of 20.5 mm and width of 1 mm is covered evenly with a resistive paste (here $R = 100\,\mathrm{k\Omega/sq}$, best before 2016). Then the lamella is backed at 150° for 100 minutes. As shown in figure A.2 the resulting printed resistor connects all copper strips. In order to achieve resistances between 100 MΩ and 800 MΩ step by step more printed resistors are added with the same procedure. Due to this production process the printed resistors show irregularities. That is also the reason why on each lamella another number of resistors are added. The final resistances for several lamellae sides are presented in figure A.3 for different measurement voltages.

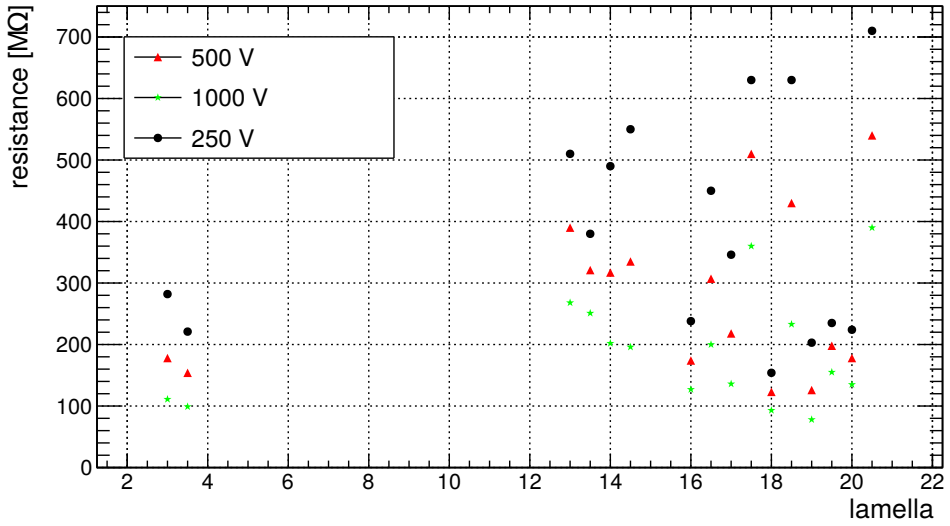

Figure A.3: The produced resistances for each lamellae side are measured with different voltages.

If the resistance lies in the desired region, it is covered with glue (UHU Plus Endfest) for better fixation. The finished lamellae are placed in the detector. Nevertheless, there is a strong variation between the produced resistance values for each lamella (see figure A.3).

Appendix B

Calculation of the Electron Guiding Angle

In order to optimize the electron guiding efficiency an optimal voltage combination between $diff_x$ and $diff_y$ has to be achieved. The direction of the electron movement is defined by the resulting electric field E_{res} which is always orientated perpendicular to the equipotential lines. First, the orientation of these equipotential lines between both lamellae is calculated by a geometrical consideration. From the resulting correlation the orientation of the electric field is defined by introducing the electron guiding angle θ. Finally, a correlation between $diff_x$ and $diff_y$ is derived for the maximum guiding efficiency.

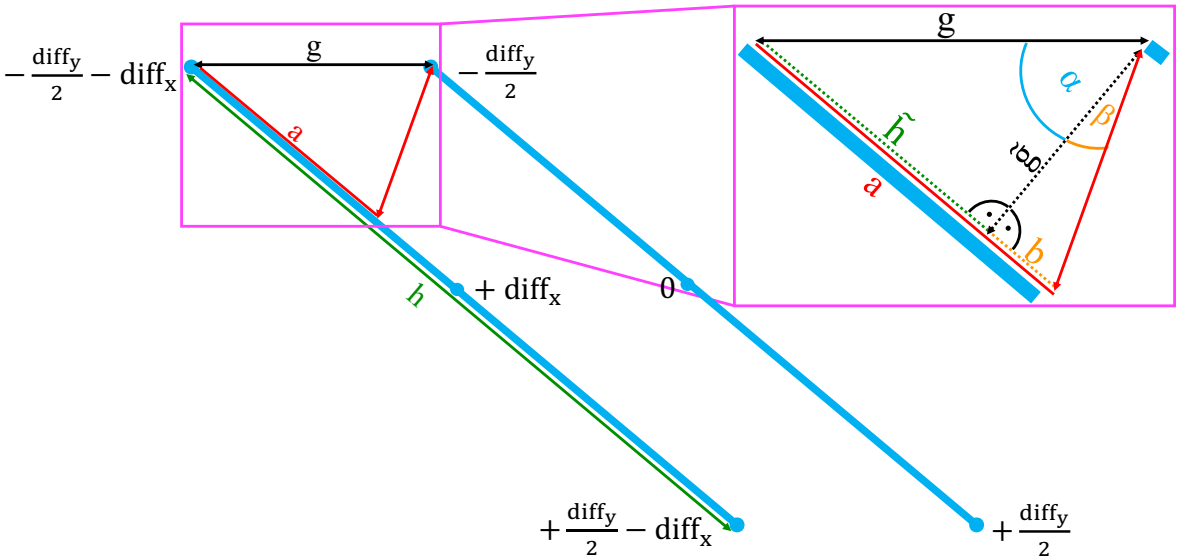

Figure B.1: To both lamellae the voltage differences $diff_x$ and $diff_y$ are applied leading to equipotential lines (red arrow) between the left and right lamella. The orientation of this equipotential line can be calculated by using the shown geometrical quantities.

In all performed simulations the voltage differences $diff_x$ and $diff_y$ are applied to the lamellae as shown in figure B.1. Each lamella has a height h and they are placed in a distance g. To each voltage combination belongs resulting equipotential lines which have a certain orientation between both lamellae. Here only one equipotential line (red arrow in figure B.1) is considered but due to a linear voltage decrease on both sides all other equipotential between both lamellae are parallel. Since for proper electron

guiding $diff_x > 0$ volt is required, the voltage $-\frac{diff_y}{2}$ (top voltage of the right lamella) is reached after a distance a at the left lamella (see figure B.1 on the left side). Due to the linear voltage decrease between top and bottom of one lamella follows

$$-\frac{diff_y}{2} - diff_x + \frac{diff_y}{h} \cdot a = -\frac{diff_y}{2} \tag{B.1}$$

leading to

$$a = \frac{h \cdot diff_x}{diff_y} \tag{B.2}$$

For certain voltage combinations the equipotential line is orientated perpendicular to the lamellae. This equipotential line has a distance $\tilde{g}$ between both lamella and is achieved after a distance $\tilde{h}$ from the top of the left lamella (see figure B.1 on the right). For both quantities a correlation between the tilting angle α of the lamellae and the distance g is found:

$$\tilde{h} = g \cdot \sin(\alpha) \tag{B.3}$$

$$\tilde{g} = g \cdot \cos(\alpha) \tag{B.4}$$

Nevertheless, in a more generalized consideration where the equipotential line has no perpendicular orientation, it is tilted against $\tilde{g}$ by β (here drawn for $b > 0$) with

$$\tan(\beta) = \frac{b}{\tilde{g}} \tag{B.5}$$

and

$$b = a - \tilde{h} \tag{B.6}$$

By inserting the previous equations into B.5 the following relation is gained:

$$\beta = \arctan\left(\frac{b}{\tilde{g}}\right) \tag{B.7}$$

$$\overset{B.6}{=} \arctan\left(\frac{a - \tilde{h}}{\tilde{g}}\right) \tag{B.8}$$

$$\overset{B.3}{=} \arctan\left(\frac{a - g \cdot \sin(\alpha)}{\tilde{g}}\right) \tag{B.9}$$

$$\overset{B.4}{=} \arctan\left(\frac{a - g \cdot \sin(\alpha)}{g \cdot \cos(\alpha)}\right) \tag{B.10}$$

$$\overset{B.2}{=} \arctan\left(\frac{\frac{h \cdot diff_x}{diff_y} - g \cdot \sin(\alpha)}{g \cdot \cos(\alpha)}\right) \tag{B.11}$$

Finally, an expression for β is found which only consists of the geometrical arrangement of the lamella (g, h and α) as well as the applied voltages $diff_x$ and $diff_y$. This can be used for defining the guiding angle θ which defines the orientation of the electric field E_{res}.

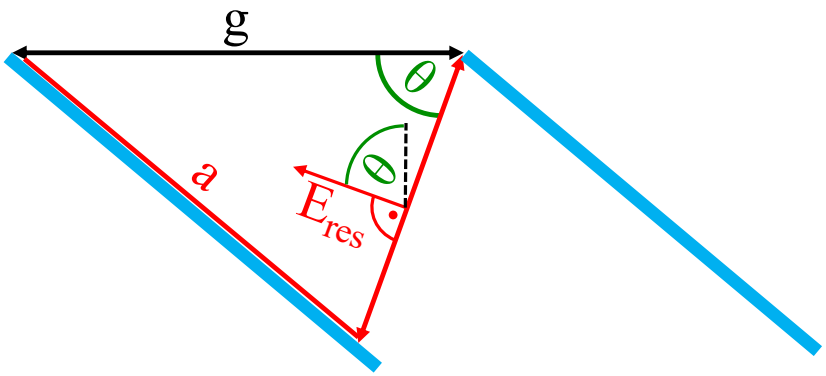

Figure B.2: The electric field E_{res} is perpendicular to the equipotential line (red arrow connection both lamellae) and its orientation can be described with the guiding angle θ. It determined the direction of the electrons between the lamellae since they drift parallel to the electric field in opposite direction.

The guiding angle θ is defined as

$$\theta = \alpha + \beta \tag{B.12}$$

which can be seen by comparing figure B.1 and B.2. As shown in figure B.2 it does not only set the orientation of the equipotential line but also of the resulting electric field E_{res} which is always perpendicular to the equipotential line. The electrons between both lamellae drift parallel to the electric field E_{res} but in opposite direction. Consequently, the electron guiding efficiency is determined by the guiding angle θ with

$$\theta = \alpha + \arctan\left(\frac{\frac{h \cdot diff_{\text{x}}}{diff_{\text{y}}} - g \cdot \sin(\alpha)}{g \cdot \cos(\alpha)}\right) \tag{B.13}$$

It is expected that most of the electrons can be extracted, if E_{res} is parallel to the lamellae meaning $\theta \stackrel{!}{=} \alpha$. In this case the equipotential lines are perpendicular to the lamellae. For this situation the arctan-function or rather its argument has to be 0:

$$\frac{\frac{h \cdot diff_{\text{x}}}{diff_{\text{y}}} - g \cdot \sin(\alpha)}{g \cdot \cos(\alpha)} \stackrel{!}{=} 0 \tag{B.14}$$

Consequently, in the case of maximum guiding efficiency a correlation for the proper voltage pair $diff_{\text{x}}$ and $diff_{\text{y}}$ is found:

$$diff_{\text{x}} = \frac{g \cdot \sin(\alpha)}{h} \cdot diff_{\text{y}} \tag{B.15}$$

Appendix C

Simulation of the GEM Foil

In order to verify the modeled GEM geometry, simulations regarding the GEM foil are performed.

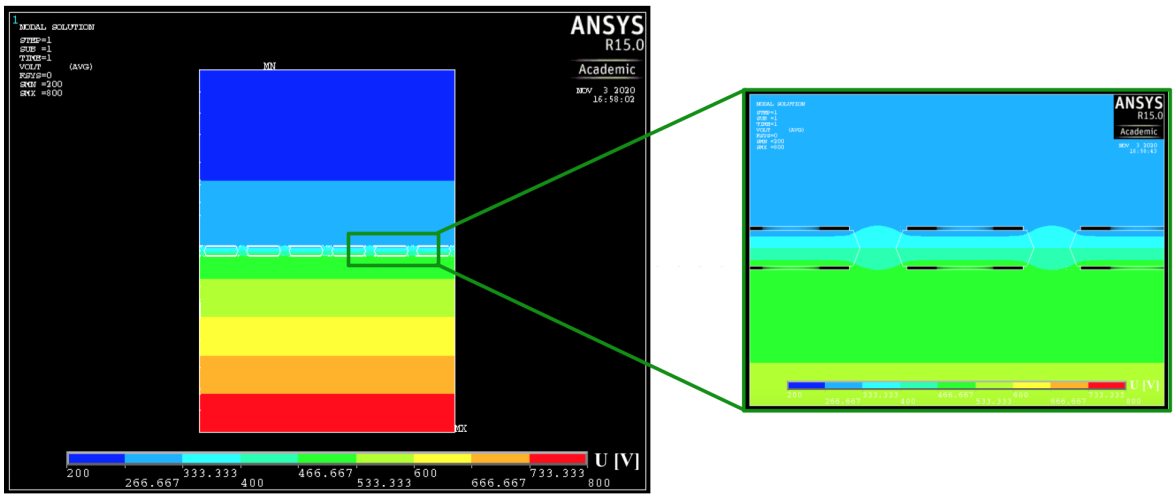

Figure C.1: Potential distribution of the GEM foil for exemplary for $\Delta U_{\text{drift}} = 100\,\text{V}$, $\Delta U_{\text{GEM}} = 200\,\text{V}$ and $\Delta U_{\text{ind}} = 300\,\text{V}$.

Therefore, a GEM foil made of 6 GEM unit cells is created in ANSYS with a 1 mm high drift region on the top and a 1 mm high induction area at the bottom. The calculated electric field configurations are imported to Garfield++. Furthermore, a certain number of electrons are positioned above the GEM foil with zero kinetic energy. With this setup the influence of the electric fields E_{D} for the drift and E_{I} for the induction region is investigated. For verification the simulation results are compared to [28]. While the $E_{\text{D}} = 1\,\text{kV}\,\text{cm}^{-1}$ is constant, E_{I} is varied for different ΔU_{GEM} voltages. As in [28] the parameters G_{tot} for the total number of electrons produced in the simulation and G_{eff} for the number of electrons which can leave the GEM foil are defined.

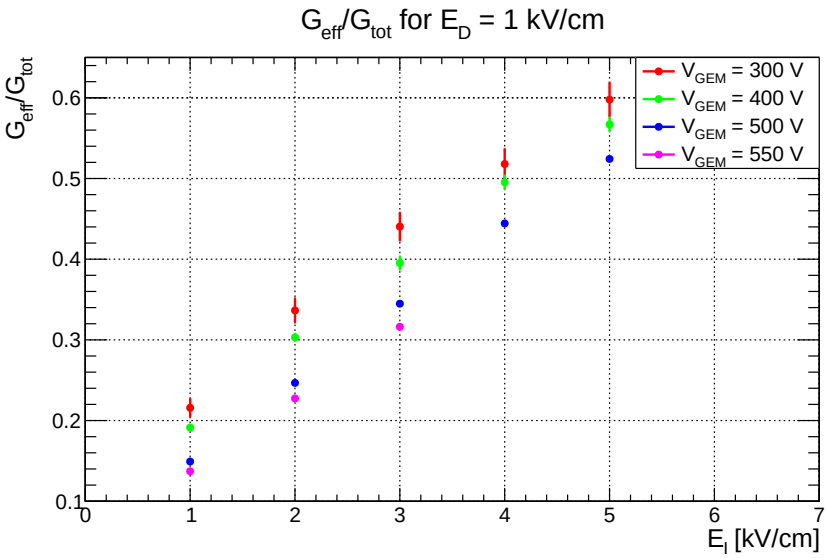

Figure C.2: $G_{\text{eff}}/G_{\text{tot}}$ is plotted for different E_{I} and constant $E_{\text{D}} = 1\,\text{kV}\,\text{cm}^{-1}$ for different ΔU_{GEM} (V_{GEM}) voltages.

The simulation results are shown in figure C.2. For constant $E_{\text{D}} = 1\,\text{kV}\,\text{cm}^{-1}$ the ratio $G_{\text{eff}}/G_{\text{tot}}$ increases with higher E_{I} field meaning more electrons can leave the GEM foil. In general, there are various possibilities where electrons are lost in the amplification process. Already primary electrons can be absorbed by the top metal layer of the GEM foil. In the GEM hole electrons diffuse in the gas they also can be absorbed by the Kapton layer. Due to attraction of the created charge by a metal, also the bottom GEM layer leads to losses. But the simulation shows that these effects can be compensated by finding the proper electric field configuration. The simulation result shows a very good agreement with [28] and small differences can occur due to slight differences in the geometry or parameter values. This results emphasize, that the GEM foil simulation works as intended.

Appendix D

Construction of the Detector Housing

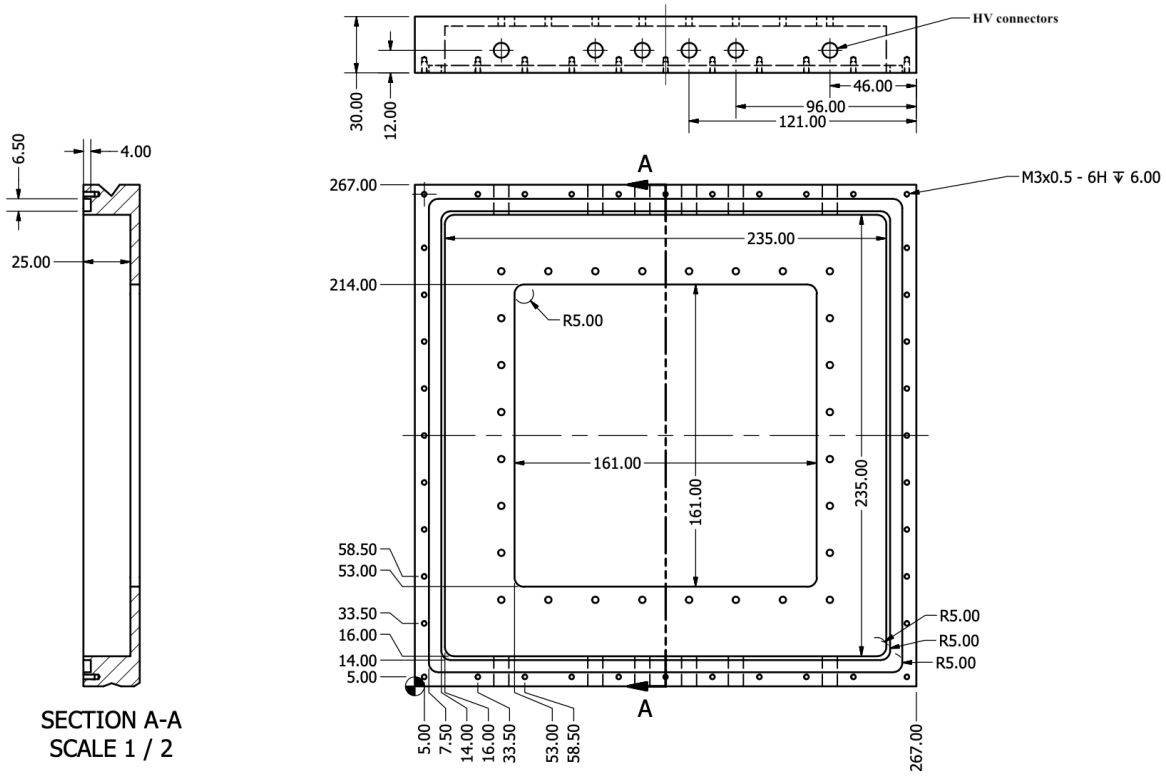

Figure D.1: Plan for a larger detector housing for the structured cathode.

Appendix E

Construction of the Lamellae Mount

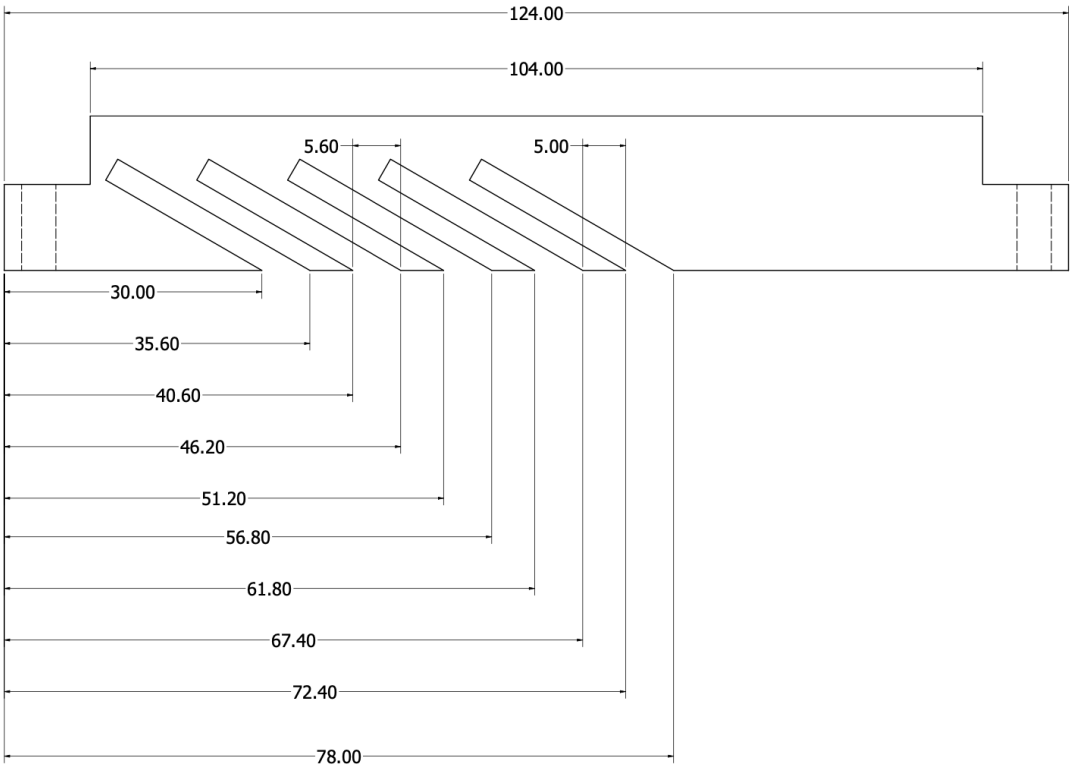

Figure E.1: Plan for the lamellae mount which is placed inside the detector.

Bibliography

[1] Fabio Sauli. The gas electron multiplier (gem): Operating principles and applications. *Nuclear Instruments and Methods in Physics Research Section A: Accelerators, Spectrometers, Detectors and Associated Equipment*, 805:2–24, 2016. https://doi.org/10.1016/j.nima.2015.07.060, Accessed: 02.09.2020.

[2] Heinz Maier-Leibniz Zentrum. Bildgebende verfahren. https://mlz-garching.de/instrumente-und-labore/bildgebende-verfahren.html, Accessed: 05.11.2020.

[3] H. A. Bethe J. Ashkin et al. E. Segr'e, H. Staub. *Experimental nuclear physics, volume I.* John Wiley & Sons, 1953.

[4] Enrico Fermi. The ionization loss of energy in gases and in condensed materials. *Phys. Rev.*, 57:485–493, Mar 1940.

[5] J.H. Hubbell M.J. Berger. Xcom: Photon cross sections database. https://www.nist.gov/pml/xcom-photon-cross-sections-database, Accessed: 17.09.2020.

[6] Konrad Kleinknecht. *Detektoren für Teilchenstrahlung.* Teubner Studienbücher Physik, 4. edition, 2005.

[7] Wolfgang Demtröder. *Experimentalphysik 4: Kern-, Teilchen- und Astrophysik.* Springer Spektrum, 5. edition, 2017.

[8] William R. Leo. *Techniques for Nuclear and Particle Physics Experiments: A How-to Approach.* Springer, 2. edition, 1995.

[9] Francisco García-Moreno and Nikolay Kardjilov. Cellular architecture overview of x ray and neutron radioscopy and tomography. 2014. https://www.researchgate.net/publication/40829132_Cellular_architecture_overview_of_X_ray_and_neutron_radioscopy_and_tomography, Accessed: 30.09.2020.

[10] A. C. Melissinos. *Experiments in Modern Physics.* Academic Press, 1966.

[11] John Townsend. *The theory of ionization of gases by collision.* Constable & Company, ltd., London, 1910.

[12] Eugenio Nappi and Vladimir Peskov. *Imaging Gaseous Detectors and Their Applications.* John Wiley & Sons, Incorporated, 2013. http://ebookcentral.proquest.com/lib/ub-lmu/detail.action?docID=1132804, Accessed: 20.9.2020.

[13] H. Raether. *Electron Avalanches and Breakdown in Gases*. Butterworths advanced physics series. Butterworths, 1964.

[14] M. J. French, L. L. Jones, Q. R. Morrissey, A. Neviani, R. Turchetta, J. R. Fulcher, G. Hall, E. Noah, M. Raymond, G. Cervelli, P. Moreira, and G. Marseguerra. Design and results from the APV25, a deep sub-micron CMOS front-end chip for the CMS tracker. *Nucl. Instrum. Methods Phys. Res., A*, 466(2):359–65, 2001. http://cds.cern.ch/record/516812, Accessed: 04.11.2020.

[15] RD51. What is SRS - RD 51 Scalable Readout System, 2010. https://indico.cern.ch/event/77597/contributions/2088463/attachments/1056845/1506857/RD51-SRS-Description.pdf, Accessed: 04.11.2020.

[16] Marcin Byszewski. Micromegas daq system mmdaq. 2011. https://indico.cern.ch/event/132080/contributions/1356987/attachments/98068/139968/byszewski_rd51mtng_mamma_daq.pdf, Accessed: 04.11.2020.

[17] Bernhard Flierl. Particle tracking with micro-pattern gaseous detectors, PhD thesis, Ludwig-Maximilians-Universität München, 2018.

[18] S. Agostinelli et al. GEANT4: A simulation toolkit. *Nucl. Instrum. Meth.*, A506:250–303, 2003.

[19] Inc. (2013) ANSYS. Ansys mechanical apdl element reference. https://www.pdfdrive.com/ansys-mechanical-apdl-structural-analysis-guidepdf-e12262220.html, Accessed 24.09.2020.

[20] Rob Veenhof. Garfield, recent developments. *Nuclear Instruments and Methods in Physics Research Section A: Accelerators, Spectrometers, Detectors and Associated Equipment*, 419(2):726–730, 1998.

[21] I. Smirnov. Heed - modeling of ionization produced by fast charged particles in gases. 2005. http://ismirnov.web.cern.ch/ismirnov/heed, Accessed: 24.09.2020.

[22] S. Biagi. Magboltz - transport of electrons in gas mixtures. August 2019. http://magboltz.web.cern.ch/magboltz/, Accessed: 24.09.2020.

[23] Katrin Penski. Development of a structured cathode to increase the efficiency of a gas detector, Bachelor's Thesis, 2018.

[24] Katrin Penski. Development of a finite elelement simulation for a structured cathode, Report, 2018.

[25] CAEN Electronic Instrumentation Tools for Discovery. Mod. a1821 / a1821h high voltage board, User's Manual, 2004.

[26] Maier-Leibnitz-Laboratorium. Broschüre für besucher, 2014. https://www.mll-muenchen.de/tandem/besucherinfo/besucherinfo.pdf, Accessed: 04.11.2020.

[27] National Institut of Standards and Technology (NIST). ASTAR - stopping power and range tables for helium ions. https://www.nist.gov/pml/stopping-power-range-tables-electrons-protons-and-helium-ions, Accessed: 04.11.2020.

[28] Sven Dildick. Gas gain in a single gem: parameter space, RD51 mini-week presentation, Department of Physics and Astronomy - Ghent University, 2011.

Acknowledgments

At this point, I would like to thank everyone who supported me during the last year. And I am really sorry if I missed anyone! I would like to tank:

- Prof. Dr. Otmar Biebel for giving me the opportunity to write this master thesis in the detector physics group and for the proofreading of my thesis.
- Dr. Ralf Hertenberger for his support and great advices.
- my supervisor Dr. Bernhard Flierl who had always time for my questions and gave me helpful feedback as well as Christoph Jagfeld who undertook this task in the last weeks of my thesis.
- the whole hardware group, Dr. Bernhard Flierl, Christoph Jagfeld, Dr. Maximilian Herrmann, Dr. Felix Klitzner, Maximilian Rinnagel, Sebastian Trost, Dr. Chrysostomos Valderanis and Fabian Vogel for the valuable discussions and inspiriting atmosphere
- the complete LS Schaile chair for the interesting and fun working environment.

Above all, a special thanks to my boyfriend Julius Kühne for his support, encouragement and understanding. And of course I thank my family and friends for their constant support in the last years.

Declaration of academic integrity

I hereby declare, that this thesis is my own work and that I have not used any sources and aids other than those stated in the thesis.

Katrin Penski

Munich, November 13, 2020